

9950-1207

RECEIVED

FEB 11 1986

SECTION 026

CAT. 43

IN -

43746

P-67

TIME DEPENDENT WIND FIELDS

FINAL REPORT

Dudley B. Chelton

College of Oceanography
Oregon State University
Corvallis, Oregon 97331

(NASA-CR-179959) TIME DEPENDENT WIND FIELDS
Final Report (Oregon State Univ.) 67 p
CSCL 08C

N87-13839

Unclas
G3/43 43639

January 27, 1986

JPL Contract No. 956567

This work was performed for the Jet Propulsion Laboratory, California Institute of Technology, sponsored by the National Aeronautics and Space Administration under Contract NAS7-100.

This document contains information prepared by Oregon State University under JPL sub-contract. Its content is not necessarily endorsed by the Jet Propulsion Laboratory, California Institute of Technology, or its sponsors.

ABSTRACT

The work performed under this contract consisted of two basic tasks: 1) determination of the accuracy of Seasat scatterometer, altimeter, and scanning multichannel microwave radiometer measurements of wind speed; and 2) application of Seasat altimeter measurements of sea level to study the spatial and temporal variability of geostrophic flow in the Antarctic Circumpolar Current.

The results of the first task have identified systematic errors in wind speeds estimated by all three satellite sensors. However, in all cases the errors are correctable and corrected wind speeds agree between the three sensors to better than 1 ms^{-1} in 96-day 2° latitude by 6° longitude averages.

The second task has resulted in development of a new technique for using altimeter sea level measurements to study the temporal variability of large-scale sea level variations. Application of the technique to the Antarctic Circumpolar Current yielded new information about the ocean circulation in this region of the ocean that is poorly sampled by conventional ship-based measurements.

TABLE OF CONTENTS

	Page
1. Introduction	1
2. SASS wind speed accuracy	3
3. ALT wind speed accuracy	5
4. SMMR wind speed accuracy	9
5. ALT sea level variability in the Antarctic	11
Circumpolar Current	
6. Conclusions and Recommendations	14
7. List of publications supported by this Research Contract	16
References	17
Appendix 1: A review of satellite altimeter measurement of	19
sea surface wind speed with a proposed new algorithm.	
Appendix 2: Comments on: Seasonal variation in wind speed	33
and sea state from global satellite measurements.	
Appendix 3: Temporal variability of the Antarctic Circum-	41
polar Current observed from satellite altimetry.	
Appendix 4: Observing large-scale temporal variability of	45
ocean currents by satellite altimetry: with application to the Antarctic Circumpolar Current.	

1. Introduction

Analysis of Seasat data has demonstrated that there are three microwave sensors capable of measuring sea surface wind speed from satellites. These are the scatterometer (SASS), altimeter (ALT) and scanning multichannel microwave radiometer (SMMR). All three sensors measure the wind speed indirectly by measuring different physical aspects of the sea surface roughness. The algorithms for converting the sensor-measured sea surface parameters to wind speed have been derived from very limited data sets and then applied to the full 96-day Seasat data set. One of the purposes of the research funded under this contract was to evaluate the accuracy of wind speeds measured by all three satellite sensors.

ALT and SASS are both active radars which beam a pulse of microwave radiation at the sea surface and measure the power of the returned signal. The ALT radar points at satellite nadir while the SASS radar is a fan beam which measures from nadir to approximately 60° incidence angle on both sides of the satellite (with a gap between 10° and 25° incidence angles). The power of the backscattered signal is sensitive to the roughness of the sea surface. As the sea surface roughness increases with increasing wind speed, the power of the backscattered signal decreases at satellite nadir through specular reflection away from the receiving antenna and increases at incidence angles greater than 10° due to Bragg scattering.

SMMR is a passive radiometer which measures the natural microwave radiation emitted from the sea surface. The "brightness temperature" of the sea surface from horizontal polarization is correlated with sea surface roughness and foam coverage. As the roughness and foam cover increase with increasing wind speed, the sea surface becomes a more efficient radiator and the brightness temperature increases.

Among the three satellite microwave wind speed estimates, off-nadir SASS measurements have received by far the greatest attention. Summaries of the evolution of the algorithm and the calibration data used to derive sea surface wind speed from SASS backscatter measurements can be found in the works by Boggs [1981] and

Schroeder et al. [1982]. The off-nadir SASS wind speed algorithm is based on extensive aircraft scatterometer measurements prior to the launch of Seasat and aircraft underflights during the Seasat mission. In addition, the off-nadir SASS wind speed algorithm incorporated orders of magnitude more direct comparisons between satellite and in situ measurements than either the ALT or SMMR algorithms. It is therefore reasonable to assume that SASS wind speed estimates are the most accurate satellite measurement of wind speed.

In Sec. 2, the results of an evaluation of the overall accuracy of SASS wind speeds by comparison with NDBO buoy winds is summarized. It was found that SASS wind speeds are in error by approximately a 1 ms^{-1} bias. The probable cause of this simple error is discussed in detail.

In the research performed under this contract, off-nadir SASS wind speeds were used to evaluate the accuracy of both ALT and SMMR wind speeds. It was found that winds speeds from both ALT and SMMR differed significantly from SASS wind speeds. Investigations into the cause for these differences identified errors in both the ALT and SMMR wind speed algorithms. These errors are described in Secs. 3 and 4. When the algorithms are corrected, wind speed estimates from ALT and SMMR agree quite well with SASS estimates.

The ultimate goal of these thorough investigations of the accuracy of satellite wind speeds is to use the data to study wind forced ocean circulation. However, application of the wind data was not included in the research supported under this contract.

An additional research project funded under this contract was analysis of Seasat ALT measurements of sea level to study the spatial and temporal variability of geostrophic flow in the Southern Ocean. This work resulted in the development of a new technique for extracting sea level variability time series from ALT data and revealed new information on the structure of variations in the flow of the Antarctic Circumpolar Current. The results of this study are summarized in Sec. 5.

2. SASS wind speed accuracy

For reasons discussed in the Introduction, vertically polarized, off-nadir SASS measurements are presently the most reliable remotely sensed estimate of sea surface wind speed. It is therefore reasonable to use these data as a basis for comparison with ALT data. In any event, there is no alternative high-quality wind data base which could be used to derive wind speed model functions for ALT and SMMR. In order to evaluate the accuracy of the SASS winds, we compared them with in situ measurements from 19 National Data Buoy Office (NDBO) buoys scattered around the coast of North America. During 1978, the winds were measured by NDBO buoys at 1-s intervals for 8.5 min. The average over the 8.5-min. interval was then reported every 3 hours (with approximately 25% of the buoys reporting hourly).

For purposes of comparison with vertically polarized, off-nadir SASS wind speed estimates, the NDBO buoy and SASS data sets were searched for matches within 100 km and 1 hour. A scatter plot comparison of the two measures of the wind speed is shown in Fig. 1. This figure suggests that there is a 1 ms^{-1} bias in the SASS wind speed estimates. This bias has been independently discovered by Wentz et al. [1984]. It can probably be attributed to the fact that the final SASS wind speed algorithm was heavily tuned to a particular buoy wind recorder in the JASIN experiment. Postexperiment calibration of this recorder showed that it was overestimating the wind speed by about 10% [Weller et al., 1983], corresponding to a 1 ms^{-1} error for the 10 ms^{-1} winds typically observed in JASIN. This error was not confirmed until after the GDR processing of SASS data. Aside from the simple 1 ms^{-1} bias in Fig. 1, the agreement between SASS and NDBO buoy winds is quite good. The rms difference between the two estimates of wind speed (after removing the 1 ms^{-1} bias) is 2.03 ms^{-1} . Much of the scatter is undoubtedly due to the general difficulty in making accurate wind measurements from a buoy [see Weller et al, 1983] and to the differences between an instantaneous satellite measurement over a finite footprint and a temporally averaged buoy measurement at a point.

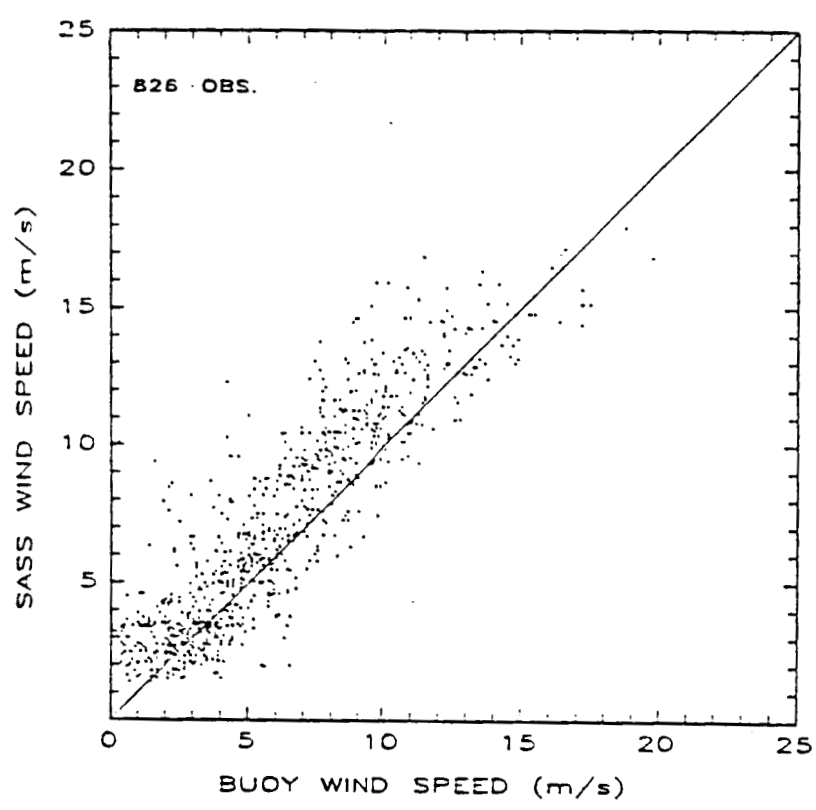


Fig. 1. Scatter plot comparison of coincident 19.5 m vertically polarized, off-nadir SASS estimated and NDBO buoy measured wind speeds. For a given orbit, all vertically polarized, off-nadir SASS observations within 100 km and 1 hour of a buoy measurement have been averaged. Data from orbits where the range of SASS wind speeds within the 100 km window exceeded 3 ms^{-1} have been excluded. SASS wind speeds are biased 1.06 ms^{-1} high over these 826 observations and the rms error about the bias is 2.03 ms^{-1} .

Although it is admittedly an ad hoc "correction", we feel there is strong justification for removal of a 1 ms^{-1} bias from the SASS GDR wind speeds. The range of uncertainty about this 1 ms^{-1} bias is difficult to assess given such a limited surface "truth" comparison data set, but a 1 ms^{-1} bias removal is certainly an improvement over using the raw GDR SASS wind speeds with no bias adjustment. Therefore, a 1 ms^{-1} bias has been removed from all of the SASS wind speeds used in the analysis that follows.

3. ALT wind speed accuracy

A complete summary of investigation of the accuracy of ALT wind speeds is given in Chelton and McCabe (1985) and Chelton (1985), included here as Appendices 1 and 2. Ideally, we would like to examine the accuracy of the ALT wind speed algorithm as with SASS by a direct comparison with high-quality in situ wind speed measurements such as the NDBO buoy winds. However, a search for NDBO buoy observations within 100 km and 1 hour of ALT measurements resulted in only 14 independent buoy observations. This small number of matches is due to the small ALT footprint size and the fact that ALT measures only at satellite nadir (as opposed to SASS which measures over two 500 km swaths in the off-nadir regime). Clearly, 14 independent measurements is too few for any meaningful comparison.

This lack of coincident satellite and buoy measurements is a long-standing problem in satellite wind speed algorithm development. To circumvent this problem, a new method of calibrating ALT wind measurements was proposed. Rather than comparing with in situ measurements, ALT measurements can be compared with vertically polarized, off-nadir SASS measurements (corrected for the 1 ms^{-1} bias discussed above). Since the ALT nadir samples are 200 km from the nearest off-nadir SASS samples, it is clearly not possible to compare instantaneous measurements by the two sensors. In this research, spatial and temporal averages of ALT and SASS wind speeds were compared. Because of their different sampling characteristics, a

given geographical region is sampled at different times by ALT and off-nadir SASS. If the winds are steady and constant over the geographical region, this time separation causes no problems. However, for variable winds, the samples by each sensor must be temporally averaged. The temporal average must be long enough so that the variable winds are sampled frequently enough to obtain a reliable estimate of the mean wind speed over the averaging period. For the Seasat mission, the maximum possible averaging period is 96 days. After experimenting with different spatial averages, 2° of latitude by 6° of longitude was subjectively chosen as a trade-off between reliable spatial averages (limited by the small footprint size of individual ALT measurements) and number of ALT and SASS intercomparisons.

Use of this proposed method of calibration is obviously dependent on the accuracy of SASS wind speed estimates. This is clearly a rather serious limitation since the accuracy of SASS winds has not yet been demonstrated over a broad range of conditions. In addition, the 1 ms^{-1} ad hoc correction is a little disturbing (although justifiable in view of known problems with JASIN data used to calibrate the SASS wind speed algorithm). However, it is almost certainly true that the errors in SASS wind speed estimates are no worse than errors in wind speed estimates by conventional measurement techniques. Since the wind speed comparison is based on spatial and temporal averages of a large number of individual observations, random errors in individual SASS wind speed estimates will be either eliminated or greatly reduced. Systematic errors, such as cross-track biases in SASS wind speed estimates, will also be greatly reduced since the spatial and temporal averages include individual wind speed estimates over the full SASS incidence angle range.

ALT wind speed retrieval is a two-step procedure. In the first step, the normalized radar cross-section σ° is computed from receiver gain (AGC), satellite attitude angle and satellite height. In the second step, the wind speed is computed from σ° . In this study of ALT wind speed estimation from Seasat, problems were identified in both steps of the procedure.

The most fundamental problem is an error in the σ° algorithm implemented in Seasat ALT GDR processing which resulted in a discontinuous dependence of σ° on AGC. When this algorithm is corrected to remove all discontinuities, the resulting values of σ° are much more reasonable than those produced in the Seasat GDR's. The corrected algorithm (suggested by D. Hancock (personal communication, 1983)) is much simpler than the Seasat GDR σ° algorithm.

The wind speeds computed from corrected σ° still exhibit rather peculiar behavior. The Seasat GDR wind speed model function was adopted from the GEOS 3 algorithm derived by Brown et al. [1981]. In this algorithm, the wind speed is first estimated from a three-branch model function and then corrected with a fifth-order polynomial adjustment. The peculiar behavior of computed wind speeds was traced to discontinuous derivatives at the two branch points of the three-branch model function.

The end result of the ALT wind speed research funded through this contract has been development of a new model function for wind speed estimation from corrected values of σ° . The proposed model function has the same functional form as that used on Seasat SASS data (both nadir and off-nadir). If σ° is expressed in decibels, the new model function estimates the wind speed at 19.5 m by

$$\hat{u}_{19.5} = 10^{[(\sigma^\circ(\text{dB})/10 - G)/H]}$$

where

$$G = 1.502$$

$$H = -0.468$$

The parameters G and H were estimated by least squares from a comparison of global 96-day, 2° by 6° averages of ALT σ° with vertically polarized, off-nadir SASS wind speed. The SASS wind speeds were corrected for a 1 ms^{-1} bias which was evidently introduced into the Seasat SASS GDR processing due to calibration against an erroneous wind recorder in JASIN as discussed in Section 2.

The proposed model function of course produces ALT wind speeds which are consistent with SASS wind speeds. For the global 96-day, 2° by 6° averages, the correlation between ALT and SASS wind speed is 0.94, and the rms difference is 0.82 ms^{-1} . A distinct advantage of this technique for ALT and SASS wind speed comparison is that the averaging removes any random component of error in individual estimates of wind speed. It should be born in mind that the validity of the proposed algorithm has only been demonstrated on spatially and temporally averaged data.

A natural question that arises is whether the proposed algorithm adequately describes instantaneous ALT estimates of wind speed. A rigorous test of performance on individual measurements of σ° requires an extensive high-quality in situ data base for comparison. As discussed previously, a search of the NDBO buoy data base identified only 14 independent buoy observations of wind speed within 100 km and 1 hour of Seasat ALT σ° measurements. This is clearly too few for a meaningful intercomparison. The extensive in situ measurement program planned for Geosat will correct this situation and allow an independent assessment of the proposed wind speed model function.

An alternative approach which yields some information on model function performance on instantaneous measurements is to determine the rms error of ALT σ° measurements. It was found that the point-to-point rms error was 0.3 dB. This noise can lead to very large errors in estimated wind speed. For example, the error in an estimate of 20 ms^{-1} wind speed is about 4 ms^{-1} .

It was concluded that Seasat ALT σ° measurement error is too large to provide reliable instantaneous estimates of wind speed. ALT wind speed estimates will only be useful when the data are temporally and spatially averaged. In this study, 96-day, 2° by 6° averages were used. The lower limits of averaging are the subject of further investigation. This problem is unfortunately addressable to only a limited degree from Seasat data because of intermittent sampling by ALT during the 96-day mission.

One final caveat in the proposed model function is that it is based on very few comparisons at wind speeds higher than 12 ms^{-1} .

Thus the validity of the model function is suspect at these high wind speeds. This can only be resolved from a carefully coordinated in situ measurement program such as that planned for Geosat.

4. SMMR wind speed accuracy

The accuracy of SMMR wind speeds was evaluated using the same technique used for ALT wind speeds. Temporally and spatially averaged SMMR wind speeds were compared with similarly averaged SASS wind speeds.

A careful investigation of the Seasat SMMR wind speed algorithms developed by T. Chester determined that they cannot be used in their present form because they contain errors. In all of the algorithms for the various geophysical parameters measured by SMMR, Chester applied an incorrect incidence angle correction to brightness temperatures. The Seasat SMMR was intended to measure microwave radiation at an incidence angle of 48.8° . However, because of spacecraft roll, pitch and yaw, the actual incidence angle varied about the average of 48.8° with an rms value of about 0.25° . The brightness temperature should decrease with increasing incidence angle but the Chester algorithm imposes the opposite effect.

There are also problems with some of the individual algorithms for the various geophysical parameters. For example, there are two problems with the wind speed algorithm. The first of these is a fundamental weakness in the form of the model function. The Chester wind speed model function is a two-branch model function with a branch point at about 7 ms^{-1} (see Fig. 2). The previously discussed analysis of ALT data showed that multiple-branch model functions can produce very bad results. The problem is that discontinuities in the slope of the model function at the branch point result in different probabilities of obtaining wind speeds above or below the branch point. Thus, the Chester wind speed model function for SMMR must be modified to be smoothly varying.

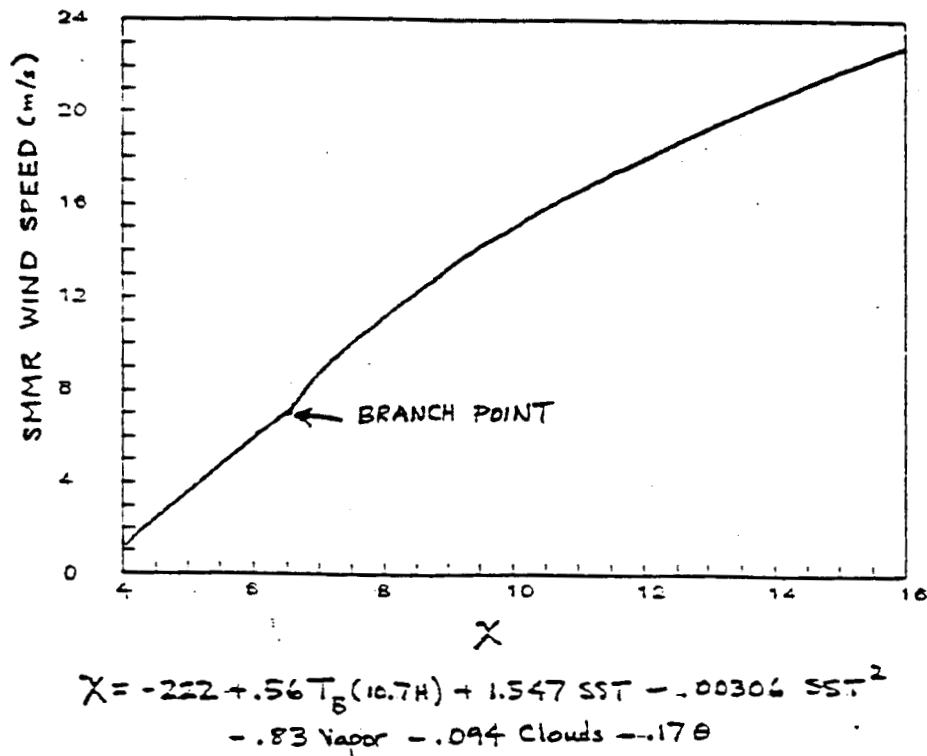


Fig. 2. The Chester 2-branch algorithm for wind speed from the Seasat SMMR. The quantity x is a function of horizontally polarized 10.7 GHz radiation, SST, water vapor, atmospheric liquid water and incidence angle.

The second problem with the Chester wind speed algorithm is an erroneous correction for SST effects. In the derivation of the Seasat algorithms, Chester compared SMMR estimated wind speed with SASS wind speeds along one orbit in the Pacific Ocean. Based on the results of the limited comparison, Chester applied an ad hoc SST dependent adjustment in the final Seasat geophysical processing. A global comparison of SMMR and SASS winds found that these "corrected" SMMR wind speeds differed from the SASS wind speeds by exactly the amount of the ad hoc SST dependent adjustment (Fig. 3). In other words, the Chester SST adjustment to wind speed should not have been applied. After removing the Chester SST adjustment (and accounting for a simple constant relative bias), the Seasat SMMR and SASS wind speeds compare very well over 2° latitude and 10° longitude 96-day averages (Fig. 4). The rms difference is 0.72 ms^{-1} with a correlation of 0.93.

5. ALT sea level variability in the Antarctic Circumpolar Current

A thorough discussion of this component of the research supported under this contract is given in Fu and Chelton (1984; 1985), included here as Appendices 3 and 4. Briefly, a new method was developed for constructing sea level time series from crossover differences of satellite altimetric measurements at geographical locations with high density of ascending and descending orbit ground track intersections (cluster areas). In this method, an orbit bias adjustment is first employed to reduce the dominant, long-wavelength orbit error by removing from altimetric measurements a constant bias over a distance of a few thousand kilometers. Residual crossover differences are then computed for each cluster location. To further reduce high-frequency residual errors, the sequence of crossover differences at each particular cluster location is smoothed using a two-dimensional running average window in the two-time domain spanned by the ascending and descending orbit times of the crossovers. The resulting crossover differences are then treated as measurements of time-lagged sea level differences, from which an irregularly spaced time series of sea level

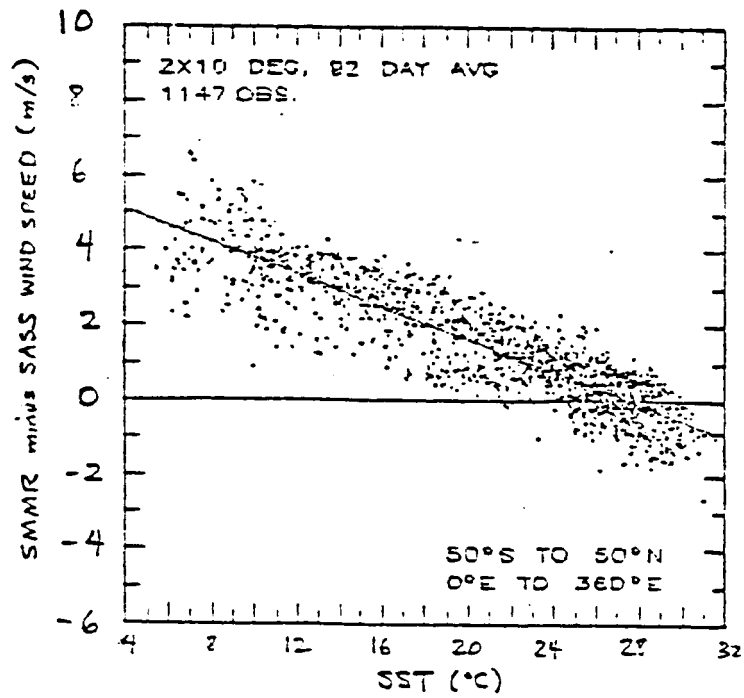


Fig. 3. Difference between globally distributed 2° latitude by 10° longitude 96-day average Seasat SMMR and SASS wind speeds as a function of SST.

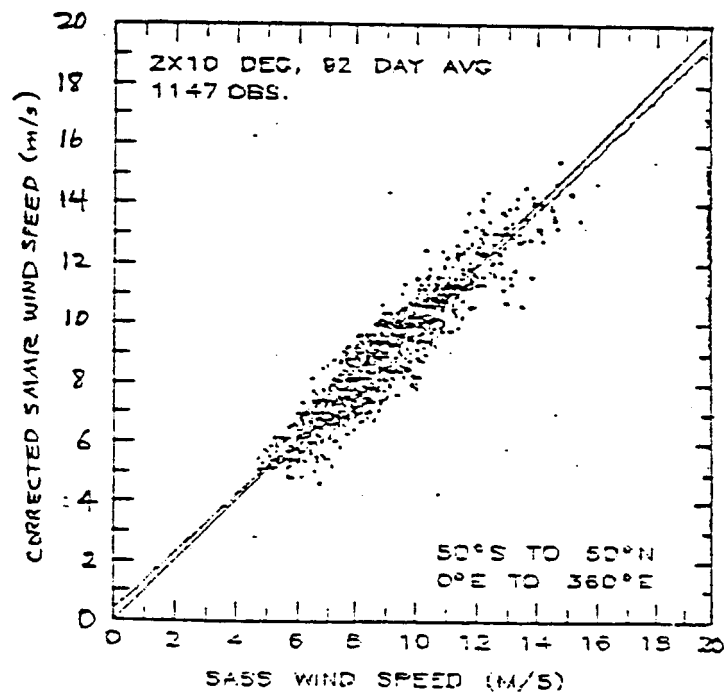


Fig. 4. Comparison between Seasat SMMR and SASS 2° latitude by 10° longitude 96-day average wind speeds with the Chester *ad hoc* SST adjustment removed.

variation is estimated by a least squares technique. Finally, an evenly spaced sea level time series is constructed at each cluster location from the irregularly spaced samples using optimal interpolation.

The method was applied to Seasat data over the Southern Ocean to study large-scale temporal variability of the ACC during the Seasat mission (July 7, 1978, to October 10, 1978). Due to the fact that the Seasat orbits were nonrepeating (except for the last 30 days of the mission), clusters of crossover differences were sampled in a finite area of 200 x 200 km to assure adequate temporal coverage. In a given cluster area, the crossover differences are smoothed over a 20 x 20 day running window to reduce the magnitude of measurement errors to a marginally useful value of 5 cm (rms). Hence the resulting altimetrically measured sea level time series for each cluster location represents a spatial and temporal average of the true sea level variations.

The altimetric results were compared with in situ bottom pressure measurements made by pressure gauges deployed at a depth of 500 m on the continental slope on either side of Drake Passage. The comparison shows fair agreement between the two measurements at the southern side of Drake Passage, but substantial disagreement is found at the northern side. It is speculated that this is due to a greater presence on the northern side of the ACC of baroclinic variability which causes the differences between sea level and bottom pressure measurements.

A total of 229 time series were computed from the Seasat altimeter data, covering the entire ACC region from 40°S to 65°S. An empirical orthogonal function (EOF) analysis of the time series indicates that 73.5% of the total variability during the 96-day Seasat mission can be accounted for by the first EOF, which is characterized by a general decrease in sea level around the southern side of the ACC and a general increase in sea level to the north. The corresponding change in surface geostrophic velocity indicates a generally eastward acceleration of the ACC. Substantial meridional components of the acceleration are observed over major topographic features. The small

magnitude of the large-scale meridional velocity change (about 2 cm/s over the 3-month mission) indicates that the extent of meridional migrations of the ACC axis during the Seasat mission are, at most, a few hundred kilometers.

The results of this analysis constitute the first direct observational evidence for large-scale coherence in the temporal variability of the ACC. Although the accuracy and statistical significance of the results are questionable due to the short duration and substantial measurement errors of the Seasat altimeter, the results have demonstrated the great potential of the methodology in application to more accurate and longer duration altimetric missions expected in the near future. For example, the projected rms accuracy for the altimeter proposed for the TOPEX mission [see TOPEX Science Working Group, 1981] is 14 cm, an order of magnitude improvement over Seasat. The TOPEX mission design calls for global altimeter measurements over a 3-year period. Using the method introduced here, it will be possible to obtain from TOPEX altimetry a global network of sea level series with much improved accuracy for studying temporal variability of the world ocean circulation.

6. Conclusions and Recommendations

The conclusions from the investigation of satellite-measured wind speed accuracy supported under this contract are that the algorithms for all three satellite sensors contain systematic errors. For SASS, the error in vertically polarized estimates of wind speed appears to be a simple bias of about 1 ms^{-1} . For ALT and SMMR the errors are more complex and due to a combination of several errors in the respective algorithms. These errors are discussed in detail in Secs. 3 and 4. When the errors are corrected, ALT and SMMR wind speeds agree with SASS wind speeds to better than 1 ms^{-1} in 96-day, 2° latitude by 6° longitude averages.

The recommendations from this analysis of wind speeds are:

- 1) The SASS V-pol wind speed model function should be modified to remove the 1 ms^{-1} bias in wind speed.
- 2) The full 96-day Seasat SASS data set should be reprocessed using the modified model function.
- 3) A thorough investigation of SASS H-pol wind speeds should be carried out to determine whether any systematic errors exist. (This work is being done by P. Woiceshyn and colleagues at JPL and F. Wentz).
- 4) The ALT σ° algorithm should be corrected and the wind speed model function used to process the Seasat data should be modified to be continuously differentiable as discussed in Sec. 3.
- 5) Seasat ALT wind speeds should be reprocessed using the corrected σ° algorithm and modified wind speed model function.
- 6) Errors in the T. Chester SMMR wind speed algorithm should be corrected and the model function modified to be continuously differentiable.
- 7) The Seasat SMMR wind speeds should be reprocessed using the corrected algorithm and modified wind speed model function.

The conclusions from the ALT sea level analysis supported under this contract are that altimeter data are indeed useful for studies of large-scale, low frequency variability of geostrophic currents. The results of this research represent the first application of altimeter data for studies of this nature. These conclusions have important implications for use of ALT data from the proposed TOPEX mission.

7. List of publications supported by this Research Contract

The following publications were supported by this Research Contract. These publications are included here as Appendices.

Fu, L.-L., and D. B. Chelton , 1984: Temporal variability of the Antarctic Circumpolar Current observed from satellite altimetry. Science, 226, 343-346.

Fu, L.-L., and D. B. Chelton, 1985: Observing large-scale temporal variability of ocean currents by satellite altimetry; with application to the Antarctic Circumpolar Current. Journal of Geophysical Research, 90, 4721-4739.

Chelton, D. B., and P. J. McCabe, 1985: A review of satellite altimeter measurement of sea surface wind speed; with a proposed new algorithm. Journal of Geophysical Research, 90, 4707-4720.

Chelton, D. B., 1985: Comments on: Seasonal variation in wind speed and sea state from global satellite measurements. Journal of Geophysical Research, 90, 5001-5008.

References

- Boggs, D. H., 1981: The Seasat scatterometer model function: the genesis of SASS-1. Rep. 622-230, 30 pp., Jet Propul. Lab., Pasadena, California.
- Brown, G. S., H. R. Stanley, and N. A. Roy, 1981: The wind speed measurement capability of spaceborne radar altimetry. IEEE J. Oceanic Eng., OE6, 59-63.
- Chelton, D. B., 1985: Comments on: Seasonal variation in wind speed and sea state from global satellite measurements. J. Geophys. Res., 90, 5001-5008.
- Chelton, D. B., and P. J. McCabe, 1985: A review of satellite altimeter measurement of sea surface wind speed; with a proposed new algorithm. J. Geophys. Res., 90, 4707-4720.
- Fu, L.-L., and D. B. Chelton, 1984: Temporal variability of the Antarctic Circumpolar Current observed from satellite altimetry. Science, 226, 343-346.
- Fu, L.-L., and D. B. Chelton, 1985: Observing large-scale temporal variability of ocean currents by satellite altimetry; with application to the Antarctic Circumpolar Current. J. Geophys. Res., 90, 4721-4739.
- Schroeder, L. C., D. H. Boggs, G. Dome, I. M. Halberstam, W. L. Jones, W. J. Pierson, and F. J. Wentz, 1982: The relationship between wind vector and normalized radar cross section used to derive Seasat-A Satellite Scatterometer winds, J. Geophys. Res., 87, 3318-3336.
- TOPEX Science Working Group, 1981: Satellite altimetric measurements of the ocean. Doc. 400-111, Jet Propul. Lab., Pasadena, Calif.

Weller, R. A., R. E. Payne, W. G. Large, and W. Zenk, 1983: Wind measurements from an array of oceanographic moorings and from F/S Meteor during JASIN 1978. J. Geophys. Res., 88, 9689-9705.

Wentz, F. J., S. Peteherych, and L. A. Thomas, 1984: A model function for ocean radar cross sections at 14.6 GHz, J. Geophys. Res., 89(C3), 3689-3704.

A Review of Satellite Altimeter Measurement of Sea Surface Wind Speed: With a Proposed New Algorithm

DUDLEY B. CHELTON

College of Oceanography, Oregon State University, Corvallis

PATRICK J. McCABE

Jet Propulsion Laboratory, Pasadena, California

The scheduled February 1985 launch of a radar altimeter aboard the U.S. Navy satellite Geosat has motivated an in-depth investigation of wind speed retrieval from satellite altimeters. The accuracy of sea surface wind speed estimated by the Seasat altimeter is examined by comparison with wind speed estimated by the Seasat scatterometer. The intercomparison is based on globally distributed spatial and temporal averages of the estimated wind speed. It is shown that there are systematic differences between altimeter and scatterometer wind speed estimates. These differences are traced to errors in the Seasat altimeter geophysical data record wind speed algorithm. A new algorithm is proposed which yields consistent estimates from the two satellite sensors. Using this new algorithm, the rms difference between spatial and temporal averages of the two wind speed estimates is less than 1 m/s, and their correlation is greater than 0.9.

1. INTRODUCTION

Satellite radar altimeters were developed principally for measurement of the sea surface elevation from which the general ocean circulation and temporally varying ocean currents can be studied (see *Fu* [1983] for a recent review). Altimeter data can also be used to infer the ocean surface significant wave height and wind speed from an examination of the shape and amplitude of the return radar signal [see *Fedor and Brown*, 1982]. For wind measurements, a satellite scatterometer is generally more useful since it measures the wind speed more accurately and also provides information about the wind direction. However, it will be at least 5 years before the next satellite scatterometer is launched. Since an altimeter is scheduled for February 1985 launch on board the U.S. Navy satellite Geosat, it is useful to examine the accuracy of wind speeds estimated from radar altimetry.

To date, three satellite altimeters have orbited the earth. The first was carried on board Skylab in 1973. The noise level of this first altimeter was too high for the data to be of any value for wind speed estimation. GEOS 3, launched in April 1975, carried the first altimeter capable of estimating sea surface wind speeds. The GEOS 3 altimeter observed the ocean surface for 3 1/2 years until December 1978. An improved altimeter was launched on Seasat in July 1978. The Seasat altimeter operated until October 1978 when a power failure brought the mission to an unfortunate premature end. In this paper, we review wind speed retrieval from the Seasat altimeter and evaluate the algorithms for possible implementation on Geosat.

Seasat carried three microwave sensors capable of remotely measuring winds at the sea surface. Two of these, the scatterometer (SASS) and altimeter (ALT), were active radars which beamed a pulse of microwave radiation at the sea surface and measured the power of the backscattered radiation. Wind speed estimation from SASS and ALT is based on the prin-

ciple that backscattered power depends almost exclusively on short-wavelength roughness of the sea surface, which itself is dependent on wind speed. The third sensor, the scanning multichannel microwave radiometer (SMMR), was a passive radiometer which measured the power of the natural radiation emitted from the sea surface and intervening atmosphere. By correcting for atmospheric effects, the power of the residual radiation can be converted to the "brightness temperature" of the sea surface which is, in part, a function of wind speed (see *Swift* [1980] for a summary). The data from these three sensors have been processed to geophysical data records (GDR's) by the Jet Propulsion Laboratory. The wind speed algorithms are purely empirical and were developed using entirely different "calibration" data for each sensor. If the various algorithms have been derived appropriately, there should be no systematic differences in the wind speed estimates from all three sensors. In this paper, we compare ALT and SASS wind speed estimates in order to assess the accuracy of the corresponding algorithms.

Most oceanographic and atmospheric applications of sea surface winds require knowledge of the vector wind field (both speed and direction). For these applications, wind speed estimates from altimeters may not be useful. However, for studies of latent heat flux, knowledge of only the wind speed is sufficient [*Liu and Niiler*, 1984], and ALT estimates of wind speed could be very useful. Recent evidence [*Halpern and Knox*, 1983] that cloud motions can be used to infer the wind direction at the sea surface (at least in tropical regions) suggests another potential application of ALT data. Vector surface winds could be determined by combining altimeter estimates of surface wind speed with surface wind direction inferred from cloud motions. It is therefore useful to examine ALT wind speed estimates in some detail in order to evaluate the accuracy of present algorithms. This is particularly important in view of the fact that, at least for the next several years, the Geosat altimeter is the only hope for obtaining global sea surface wind data.

There are a number of methods of determining the accuracy of satellite estimates of wind speed. The approach generally

Copyright 1985 by the American Geophysical Union.

Paper number 4C1478.
0148-0227/85/004C-1478\$05.00

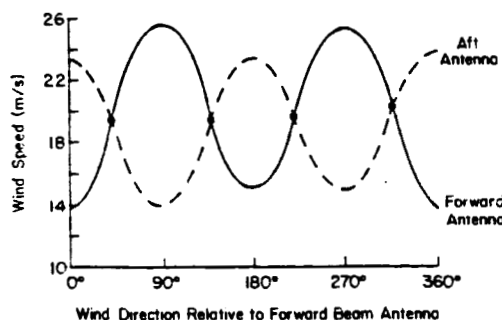


Fig. 1. Schematic diagram showing the possible vector wind solutions from a forward and aft antenna pair with pointing angles separated by 90°. For noise-free measurements, the true wind vector is one of the four intersections of the two curves.

taken in the past has been to compare satellite backscatter measurements with high-quality surface "truth" measurements. Since exactly coincident observations (in both space and time) seldom occur, measurements within 100 km and 1 hour are usually considered "coincident." A fundamental difficulty is that satellites and in situ instruments sample very different characteristics of the same wind field. Satellites measure wind speed averaged over a finite spatial footprint at an instant in time. The size of the footprint varies, ranging from less than 10 km for ALT to 50 km for SASS. In comparison, conventional anemometers measure the turbulent wind field at a single point in space. Much of the inherent turbulent variability (which is generally not of interest to large-scale studies) can be removed by averaging over time. For example, to compare a satellite wind speed measurement of 8 m s⁻¹ over a 50-km footprint with an anemometer measurement of the same wind field, the anemometer record must be averaged over something like 100 min (the time required for a Lagrangian particle in a typical 8 m s⁻¹ synoptic wind field to travel 50 km). Except in carefully conducted experiments, this filtering of anemometer data is rarely done.

Wentz *et al.* [1982] proposed another method of determining the accuracy of satellite estimates of wind speed. They compared instantaneous estimates of wind speed from different satellite sensors. To obtain coincident measurements, the analysis was restricted to satellite nadir (the point directly beneath the orbiting satellite). The results suggested that ALT wind speeds were biased low relative to nadir SASS wind speeds. However, nadir SASS winds are not nearly as reliable as off-nadir SASS winds. In part, this is because the algorithm for nadir SASS wind speeds was developed by a circuitous method that did not involve any direct comparisons with in situ data (see Wentz *et al.* [1982] for a summary). Since off-nadir SASS wind speeds are 200 km or more from satellite nadir, coincident observations with ALT measurements do not exist.

An alternative method of determining the accuracy (or at least the consistency) of wind speeds measured from satellites is to compare spatial and temporal averages (maps) of wind speed from the different sensors. This is the method used in this paper. The advantage of this approach is that it does not require coincident observations and therefore yields a far greater number of comparisons. The obvious limitation is that if the winds are highly variable, this method requires a uniform sampling of the spatial area over the averaging time interval to be meaningful.

Among the various satellite microwave wind speed estimates, off-nadir SASS measurements have received by far the

greatest attention. Summaries of the evolution of the algorithm and the calibration data used to derive sea surface wind speed from SASS backscatter measurements can be found in the works by Boggs [1981] and Schroeder *et al.* [1982]. The off-nadir SASS wind speed algorithm is based on extensive aircraft scatterometer measurements prior to the launch of Seasat and aircraft underflights during the Seasat mission. In addition, the off-nadir SASS wind speed algorithm incorporated orders of magnitude more direct comparisons between satellite and in situ measurements than either the ALT or SMMR algorithms. It is therefore reasonable to assume that SASS wind speed estimates are the most accurate satellite measurement of wind speed. In this study, we use off-nadir SASS wind speeds as calibration data to examine the accuracy of ALT wind speed estimates (section 3). The two estimates of wind speed are found to differ significantly. To determine whether the differences can be attributed to errors in ALT estimates, the Seasat ALT GDR wind speed algorithm is examined in detail in section 4. It is found that errors and weaknesses exist in the present algorithms. The errors are corrected and an improved algorithm is proposed in section 5. Wind speed estimates using the new algorithm agree quite well with SASS wind speeds.

2. RADAR MEASUREMENTS OF SEA SURFACE WIND SPEED

In order to understand the similarities and differences between ALT and SASS wind speed measurements, we include here a brief summary of wind speed estimation from satellite-borne radars. More detailed discussions can be found in the works by Moore and Fung [1979] and Barrick and Swift [1980]. Both ALT and SASS operated in approximately the same microwave frequency range (13.5 GHz for ALT and 14.6 GHz for SASS). The nature of returned radar power depends strongly on the incidence angle of the radiation, defined to be the angle measured in a vertical plane between satellite nadir and the pointing angle of the radar. At small incidence angles (less than 10°) the backscattered radiation results primarily from specular reflection from ocean waves having wavelengths longer than the incident radiation (about 2 cm for ALT and SASS). As the wind speed increases, the sea surface roughness increases and a greater fraction of the incident radiation is reflected away from the satellite. Thus, at incidence angles near nadir, the power of the backscattered radiation is inversely related to wind speed but independent of wind direction.

Both ALT and SASS provided measurements of wind speed in this small incidence angle regime. Wind speed measurements in this near-nadir regime are attractive from the point of view that a long, continuous 3 1/2 year record of global

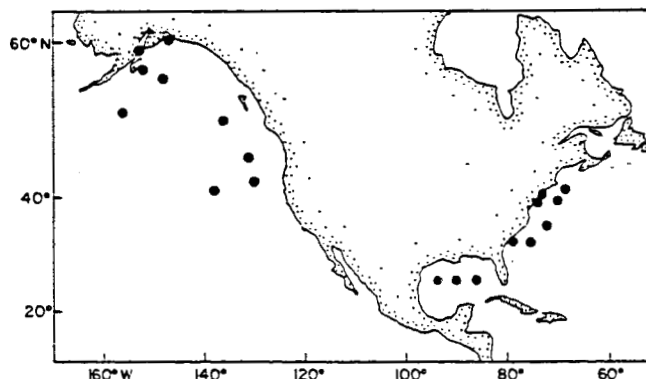


Fig. 2. Map of NDBO buoy locations during summer 1978.

nadir wind speed is available from the GEOS 3 altimeter (April 1975 to December 1978). In addition, altimeter wind speeds will soon be available from Geosat. The limitations are that (1) the sensitivity of near-nadir radar backscatter to wind speed is relatively weak so that small errors in backscatter measurement can lead to sizable errors in wind speed, (2) no information on wind direction can be obtained from near-nadir backscatter measurements, and (3) the spatial coverage of near-nadir measurements is small. For Seasat orbiting at an altitude of 800 km, $\pm 8^\circ$ of incidence angle covers an area 140 km wide centered on the satellite ground track. For the scatterometer this area is broken up into approximately 50 km cells by using doppler filtering of the backscattered radiation. For the altimeter, which measures backscatter from only a single cell centered at satellite nadir, the cross-track footprint size ranges from 2 to 10 km, depending on sea state.

At incidence angles ranging from 10° to 15° , there is no strong dependence of backscattered power on either wind speed or wind direction. Thus no wind speeds can be retrieved from satellite radar measurements in this range of incidence angles.

At incidence angles greater than 15° , few of the longer wave faces are favorably oriented for specular reflection, and the shorter ocean wave crests act analogous to a diffraction grating. The radar selectively samples resonant backscatter from ocean waves with wavelength governed by the Bragg scattering equation. At 30° incidence angle, the Bragg resonant ocean wavelengths are approximately 2 cm for the 14.6-GHz SASS radar. The amplitudes of these short capillary-gravity waves are found to increase with increasing wind speed, and the sea surface becomes more effective at scattering incident radiation. Thus the power of the backscattered radiation in this off-nadir regime increases with increasing wind speed. The sensitivity of backscattered power to wind speed improves with increasing incidence angle so that wind speed estimation is less sensitive

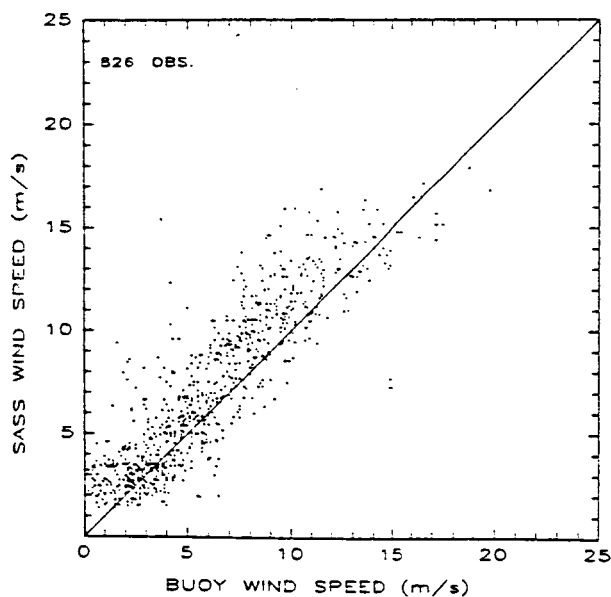


Fig. 3. Scatter plot comparison of coincident 19.5 m vertically polarized, off-nadir SASS estimated and NDBO buoy measured wind speeds. For a given orbit, all vertically polarized, off-nadir SASS observations within 100 km and 1 hour of a buoy measurement have been averaged. Data from orbits where the range of SASS wind speeds within the 100 km window exceeded 3 m s^{-1} have been excluded. SASS wind speeds are biased 1.06 m s^{-1} high over these 826 observations and the rms error about the bias is 2.03 m s^{-1} .

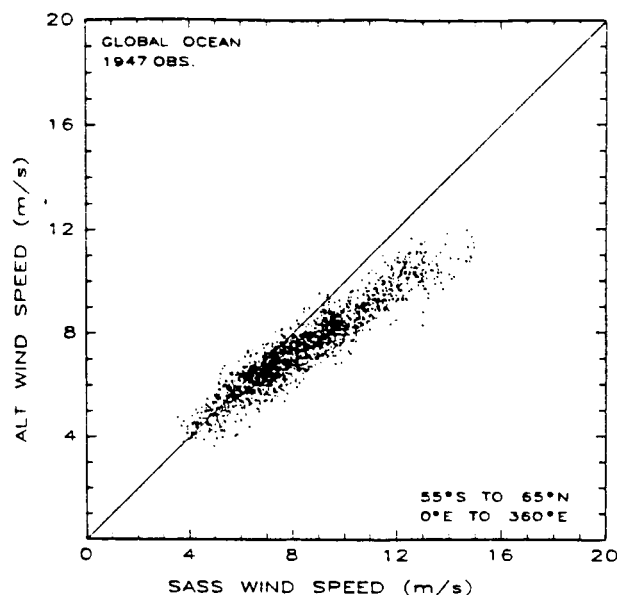


Fig. 4. Scatter plot comparison of 96-day, nonoverlapping 2° by 6° average wind speeds estimated by the Seasat ALT and SASS. Straight line represents perfect fit.

to errors in backscatter measurement than at satellite nadir. However, the total returned power decreases with increasing incidence angle. As a consequence, wind speeds in excess of 10 m s^{-1} are required at large incidence angles (greater than 55°) in order to achieve adequate signal to noise ratio with the Seasat SASS.

In the off-nadir regime, the backscattered power is dependent also on wind direction. The returned power is maximum when the antenna is pointed upwind or downwind and minimum when the antenna is pointed crosswind. This anisotropic behavior varies approximately as the cosine of twice the angle measured in a horizontal plane between the wind direction and the antenna pointing angle (see, for example, Moore and Fung [1979]). There is also a small contribution which varies as the cosine of the angle between wind direction and antenna pointing angle (which leads to a slight asymmetry between upwind and downwind backscatter for a given wind speed). For a single backscatter measurement, the possible vector wind solutions thus lie along a quasi-harmonic curve in wind speed-wind direction space. This is shown schematically in Figure 1. A second antenna measurement from a different viewing angle (optimally 90° separation from the first antenna) defines a second quasi-harmonic curve of possible vector wind solutions. For noise-free measurements, the true wind vector must lie at one of the intersections of the two curves.

The Seasat SASS carried forward and aft antennas oriented 45° and 135° , respectively, relative to the satellite ground track. A pair of such antennas was mounted on each side of the spacecraft. A fan beam antenna design was used to obtain off-nadir backscatter measurements over an incidence angle range from 25° to 55° (corresponding to a 500-km-wide swath on each side of the spacecraft, centered 450 km from satellite nadir). In each of these off-nadir regimes (port and starboard side of the spacecraft), 12 Doppler filters and range gates were used to subdivide electronically the illuminated SASS footprint into separate resolution cells and to exclude interfering signals from side lobes of the antenna. The doppler filter bandwidths were designed to give approximately 50-km cross-track cell spacing, and the measurement timing was set to give

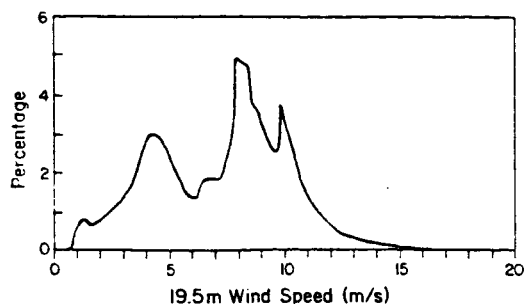


Fig. 5. Histogram of 19.5 m wind speeds computed from approximately 3 million observations during the full 96-day Seasat mission using the Seasat GDR algorithms. Bin size is 0.25 m s^{-1} .

approximately 50 km along-track cell spacing. A forward antenna measurement was combined with an aft antenna measurement at the same location to form a paired antenna multiple wind vector solution like that shown in Figure 1. The time separation between forward and aft antenna measurements at the same location varied from about a minute at 25° incidence angle to about 4 min at 55° incidence angle.

The schematic in Figure 1 shows the possible wind direction solutions relative to one of the antenna pointing angles (in this case, the forward antenna). Note that the vector wind solution from the two antennas is not unique; there are four possible solutions (the four intersections of the two quasi-harmonic curves). For more general orientation of wind direction relative to antenna pointing angle, the number of possible vector wind solutions varies from two to four.

The ambiguity in vector wind solution is a serious impediment to most applications of SASS winds. A methodology has been proposed for subjective selection of the true solution [Wurtele *et al.*, 1982]. The technique is very labor intensive and nonautomated. To date it has been applied only to 2 weeks of global SASS data in September 1978 (P. M. Woiceshyn, personal communication, 1984). However, for purposes of comparison with ALT wind speed estimates, the ambiguity in SASS solution is not a problem. Although the multiple solutions differ widely in direction, they differ very little in speed (see Figure 1). Thus the speeds corresponding to the multiple solutions can be averaged to obtain an estimate of the true wind speed. This procedure has been applied to the SASS winds used in this paper.

One final characteristic of SASS data should be noted. The microwave radiation transmitted and received by the SASS antenna can have either vertical or horizontal polarization. However, in the off-nadir regime, the power of the measured backscatter for a fixed wind speed is greater for vertical than for horizontal polarization. The difference increases with increasing incidence angle [see Jones *et al.*, 1977]. Thus vertical polarization gives a somewhat greater signal to noise ratio and consequently a generally more reliable estimate of wind speed. (This is not always true since given an adequate signal to noise ratio, horizontally polarized backscatter is more sensitive to changes in wind speed than vertically polarized backscatter.) In addition, 75% of all Seasat SASS off-nadir winds were constructed by pairing vertically polarized forward and aft antenna measurements. Since the SASS wind speed algorithm was based predominantly on comparisons between vertically polarized SASS measurements of backscatter and in situ measurements of wind speed, vertically polarized SASS winds are more reliable than other polarization combinations. We therefore restrict the SASS winds used in this study to vertically polarized, off-nadir data.

3. SEASAT ALT AND SASS WIND SPEED COMPARISON

For reasons discussed previously, vertically polarized, off-nadir SASS measurements are presently the most reliable remotely sensed estimate of sea surface wind speed. It is therefore reasonable to use these data as a basis for comparison with ALT data. In any event, there is no alternative high-quality wind data base which could be used to derive a wind speed model function for ALT. In order to evaluate the accuracy of the SASS winds, we compared them with in situ measurements from 19 National Data Buoy Office (NDBO) buoys scattered around the coast of North America (Figure 2). During 1978, the winds were measured by NDBO buoys at 1-s intervals for 8.5 min. The average over the 8.5-min interval was then reported every 3 hours (with approximately 25% of the buoys reporting hourly).

For purposes of comparison with vertically polarized, off-nadir SASS wind speed estimates, the NDBO buoy and SASS data sets were searched for matches within 100 km and 1 hour. A scatter plot comparison of the two measures of the wind speed is shown in Figure 3. Figure 3 suggests that there is a 1 m s^{-1} bias in the SASS wind speed estimates. This bias has been independently discovered by Wentz *et al.* [1984]. It can probably be attributed to the fact that the final SASS wind speed algorithm was heavily tuned to a particular buoy wind recorder in the JASIN experiment. Postexperiment calibration of this recorder showed that it was overestimating the wind speed by about 10% [Weller *et al.*, 1983], corresponding to a 1 m s^{-1} error for the 10 m s^{-1} winds typically observed in JASIN. This error was not confirmed until after the GDR processing of SASS data. Aside from the simple 1 m s^{-1} bias in Figure 3, the agreement between SASS and NDBO buoy winds is quite good. Much of the scatter is undoubtedly due to the general difficulty in making accurate wind measurements from a buoy [see Weller *et al.*, 1983] and to the differences between an instantaneous measurement over a finite footprint and a temporally averaged measurement at a point.

Although it is admittedly an ad hoc "correction," we feel there is strong justification for removal of a 1 m s^{-1} bias from the SASS GDR wind speeds. The range of uncertainty about this 1 m s^{-1} bias is difficult to assess given such a limited surface "truth" comparison data set, but a 1 m s^{-1} bias removal is certainly an improvement over using the raw GDR SASS wind speeds with no bias removed. Therefore, a 1 m s^{-1} bias has been removed from all of the SASS wind speeds used in the analysis that follows.

Ideally, we would like to examine the accuracy of the ALT wind speed algorithm by a similar direct comparison with high-quality in situ wind speed measurements such as the NDBO buoy winds. However, a search for NDBO buoy observations within 100 km and 1 hour of ALT measurements resulted in only 14 independent buoy observations. This small number of matches is due to the small ALT footprint size and

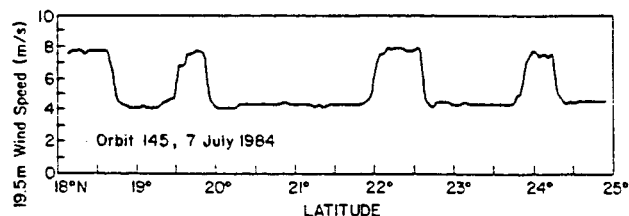


Fig. 6. Wind speeds measured over a 2-min period during descending orbit 145 over the central Pacific (approximately 160°W) on July 7, 1978.

the fact that ALT measures only at satellite nadir (as opposed to SASS which measures over two 500 km swaths in the off-nadir regime). Clearly, 14 independent measurements is too few for any meaningful comparison.

This lack of coincident satellite and buoy measurements is a long-standing problem in satellite wind speed algorithm development. To circumvent this problem, we propose a new method of calibrating ALT wind measurements. Rather than comparing with in situ measurements, we suggest comparing ALT measurements with vertically polarized, off-nadir SASS measurements (corrected for the 1 m s^{-1} bias discussed above). Since the ALT nadir samples are 200 km from the nearest off-nadir SASS samples, we clearly cannot compare instantaneous measurements by the two sensors. We propose comparing spatial and temporal averages of ALT and SASS wind speeds. Because of their different sampling characteristics, a given geographical region is sampled at different times by ALT and off-nadir SASS. If the winds are steady and constant over the geographical region, this time separation causes no problems. However, for variable winds, the samples by each sensor must be temporally averaged. The temporal average must be long enough so that the variable winds are sampled frequently enough to obtain a reliable estimate of the mean wind speed over the averaging period. For the Seasat mission, the maximum possible averaging period is 96 days. After experimenting with different spatial averages, we subjectively chose 2° of latitude by 6° of longitude as a trade-off between reliable spatial averages (limited by the small footprint size of individual ALT measurements) and number of ALT and SASS intercomparisons.

Use of this proposed method of calibration is obviously dependent on the accuracy of SASS wind speed estimates. This is clearly a rather serious limitation since the accuracy of SASS winds has not yet been demonstrated over a broad range of conditions. In addition, our 1 m s^{-1} ad hoc correction is a little disturbing (although justifiable in view of known problems with JASIN data used to calibrate the SASS wind speed algorithm). However, it is almost certainly true that the errors in SASS wind speed estimates are no worse than errors in wind speed estimates by conventional measurement techniques. Since the wind speed comparison is based on spatial and temporal averages of a large number of individual observations, random errors in individual SASS wind speed estimates will be either eliminated or greatly reduced. Systematic

TABLE 1. Loss in Backscattered Power Due to Nonzero Attitude Angle of Spacecraft

Attitude, deg	L_{att} , dB
0.00	0.0161
0.05	0.0391
0.10	0.1081
0.15	0.2231
0.20	0.3842
0.25	0.5914
0.30	0.8449
0.35	1.1445
0.40	1.4904
0.45	1.8826
0.50	2.3213
0.55	2.8066
0.60	3.3386
0.65	3.9178
0.70	4.5430
0.75	5.2158

TABLE 2. Calibrated AGC as a Function of Attenuator Step for Calculation of σ^0

Attenuator Step k	A_k , dB
8	16.58
9	24.15
10	30.30
11	35.67
12	42.27
13	48.07
14	54.52
15	60.58

errors, such as cross-track biases in SASS wind speed estimates, will also be greatly reduced since the spatial and temporal averages include individual wind speed estimates over the full SASS incidence angle range.

In any event, the proposed calibration method will produce wind speed estimates which are at least consistent between sensors. It will be seen later that the new ALT wind speed algorithm proposed in this paper is an improvement on the existing Seasat GDR algorithm. It should be born in mind, however, that any changes in the SASS wind speed algorithm at a later time may require adjustments to the new ALT wind speed algorithm. A rigorous test of the proposed algorithm will require an independent comparison with a large number of high-quality in situ measurements. This will be possible with the Geosat altimeter, as a carefully coordinated surface measurement program is being planned to provide coincident satellite and in situ measurements.

A scatter plot of 96-day averages of ALT versus SASS wind speeds over nonoverlapping 2° by 6° areas is shown in Figure 4. These 2° by 6° areas are globally distributed from latitude 65°N to 55°S . The southern boundary of the averaging region was chosen to eliminate any measurements over ice. For wind speeds greater than 5 m s^{-1} , Figure 4 suggests a systematic underestimate of wind speed by ALT. On the surface, this underestimate appears to be a very simple error, and one might be inclined to apply an ad hoc correction to the ALT wind speeds to make them agree with SASS wind speeds. However, a more detailed investigation reveals that this apparently simple discrepancy between ALT and SASS wind speeds is actually symptomatic of rather serious problems with the Seasat ALT GDR wind speed algorithm.

A histogram of globally distributed individual ALT wind speed estimates is shown in Figure 5. The histogram shows a peculiar bimodal distribution of wind speeds. This bimodal structure has previously been noted by *Chelton et al.* [1981], who speculated that it could be a true geophysical phenomenon attributed either to geographical inhomogeneities in the wind field or to temporal evolution of the wind field over the 96-day Seasat mission. However, subsequent analysis showed that the bimodal structure was present in all geographical regions and during all periods of the Seasat mission. In fact, examination of raw data along satellite ground tracks revealed abrupt toggling between about 4.5 and 8 m s^{-1} (Figure 6). These abrupt changes cannot be geophysical and provide rather clear evidence for problems somewhere in the algorithms used to retrieve wind speed from ALT. In the next section, the ALT wind speed algorithm is examined in detail to identify the source of this behavior.

4. SEASAT ALT GDR WIND SPEED ALGORITHMS

As discussed previously, ALT is an active radar which transmits 13.5-GHz microwave radiation and measures the

TABLE 3. Calibration Attenuator Value for Calculation of σ° Using Either the Seasat GDR or Fedor Algorithms

k	Seasat GDR C_k , dB	Fedor C_k , dB
8	43.7	43.9
9	36.1	36.3
10	30.3	30.15
11	24.2	24.78
12	18.2	18.18
13	12.2	12.38
14	6.2	5.93
15	0	-0.13

power of the radiation backscattered from the sea surface. In order to account for variations in the power of the transmitted signal, the power of the return signal is normalized by the transmitted power. This normalized return power is called the normalized radar cross section which is usually denoted by σ° . For ALT measurements at satellite nadir, σ° is inversely related to wind speed (see section 2). Estimation of wind speed from ALT is thus a two-step procedure. First, σ° is computed from parameters measured by the ALT receiver and from the measured height and attitude angle of the satellite. Then the wind speed is computed from σ° using an empirically derived model function. Errors in ALT wind speed estimates could therefore be due to problems in either the σ° algorithm or the wind speed model function (or both). These two steps in the retrieval of wind speed are examined separately in this section to identify the causes for errors in ALT wind speed estimates.

4.1. The σ° Algorithm

In order to maintain a constant output level from the Seasat ALT receiver and to operate the electronics within the linear response region of all receiver stages, an automatic gain control (AGC) loop was implemented in the electronics package. The power of the return radar signal was thus directly related to the AGC setting required to maintain the receiver output at the desired level. The algorithm used to convert Seasat ALT AGC to σ° is briefly summarized in this section. A more detailed technical discussion can be found in the work by Townsend [1980].

The AGC was controlled by a digital step attenuator which provided gain variation over a 0-63 dB range in 1-dB steps. For σ° values ranging from 10 to 15 dB (a range which includes 80% of all σ° values measured globally during the 96-day Seasat mission), the AGC setting ranged from 28 to 33 dB. AGC measurements were recorded at 0.1-s intervals. Each AGC value was scaled and added to the previous AGC value to obtain an average AGC which was stored on the telemetry data tape for later transmission to a ground-based receiving station. Thus, while the AGC gates were separated by 1-dB steps, the smoothed values received at the ground station had finer resolution. This final AGC was stored on tape with a least count of 1/16 dB. The integer and fractional parts of AGC were stored as separate data words in the telemetry string. These AGC values were further smoothed when 10 consecutive measurements were block averaged before converting to σ° (see discussion below).

The normalized radar cross section σ° was computed by a rather complex algorithm. The primary contribution to σ° was, of course, determined by the value of AGC. However, the AGC contribution must be corrected for loss from variations in the pointing angle of the antenna due to pitch, roll, and yaw of the satellite. The reduction of σ° is given as a function of

satellite attitude angle in Table 1. A change in attitude of only 0.5° translates to a σ° loss of 2.3 dB, which is quite substantial. A search of the data determined that the average attitude angle during the 96-day Seasat mission was 0.28° . In addition to the correction for antenna pointing angle, σ° must also be corrected for variations in the height of the satellite above the sea surface. These height variations are due to a small eccentricity about a circular orbit.

The Seasat ALT periodically executed an internal calibration during which a calibrated portion of the transmitted pulse was diverted into the antenna receiver for the purpose of AGC calibration and stability monitoring. It was found that incorporating internal calibration mode AGC values into computation of σ° eliminated any residual effects of transmission power changes and variations in receiver gain from changes in ambient temperature in the electronics package. Briefly, the internal calibration data were incorporated in the σ° algorithm as follows. First, the 0.1-s AGC values were block averaged over 1 s. This smoothed AGC value (call it A_j) was compared with the values A_k in Table 2 which correspond to eight of the stepped calibration values fed to the receiver during internal calibration mode. The operating region corresponding to the ocean AGC measurement was determined by identifying the value A_k for which the absolute value ($A_k - A_j$) was minimum. Define this value of k to be \hat{k} . Then σ° was computed by

$$\sigma^\circ = B - C_{\hat{k}} - \Delta_{\hat{k}} + L_{\text{ant}} + 30 \log_{10} (h/h_0)$$

where

- B bias, determined from prelaunch calibration measurements to be 39.93 dB for the GEOS 3 ALT; for the Seasat ALT, this bias was estimated to be 38.33 dB (see section 4.2);
- C_k attenuator value for calibration step k , obtained from the second column of Table 3;
- $\Delta_k = A_k - A_j$, where A_k is obtained from Table 2;
- L_{ant} correction for loss in σ° due to nonnadir antenna pointing angle; value was linearly interpolated from Table 1 based on known satellite attitude angle;
- h height of satellite above sea surface, km;
- h_0 reference height of satellite above sea surface (= 796.44 km).

The authors were unable to determine from the published or "gray" literature the motivation for or history of this complicated σ° algorithm. This is particularly puzzling in view of the fact that fixing $\hat{k} = 10$ in Tables 2 and 3 yields an improved algorithm (see discussion below).

To determine whether the σ° algorithm above could be responsible for the bimodal wind speed distribution in Figure 5, we constructed a histogram of Seasat σ° values computed

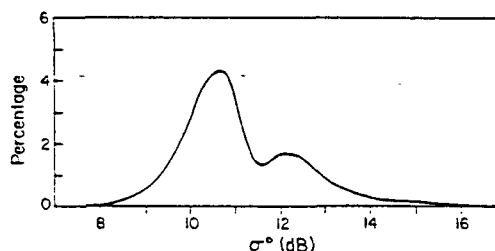


Fig. 7. Histogram of σ° computed from approximately 3 million observations during the full 96-day Seasat mission using the Seasat GDR algorithm. Bin size is 0.1 dB.

using the algorithm described above. Figure 7 shows a pronounced bimodal structure, suggesting that the σ° algorithm is a likely candidate for the bimodal behavior of the wind speeds. A more detailed investigation found that the bimodal σ° distribution was evident in all geographical regions and at all times during the Seasat mission.

The cause for the bimodal σ° distribution becomes immediately apparent when the AGC contribution to σ° is converted from tabular to graphical form (Figure 8). To isolate the AGC contribution, the attitude angle and satellite height were fixed at 0.28° and 800 km. The functional relationship between σ° and AGC is discontinuous at 27.2, 33.0, and 39.0 dB values of AGC. Note that the AGC contribution cannot produce any σ° values between 11.2 and 12.0 dB because of the discontinuity at 33.0 dB AGC. This coincides with the valley in the σ° distribution in Figure 7. The sharp cutoffs in σ° values as implied from the AGC contribution get smoothed by the satellite height and attitude angle corrections discussed above.

Clearly, these discontinuities are undesirable attributes of the σ° algorithm used in Seasat GDR processing. These discontinuities have previously been discovered independently by D. Hancock (personal communication, 1983) and L. Fedor (personal communication, 1983). However, the effects of these discontinuities on wind speed retrievals have not heretofore been fully appreciated. Both Hancock and Fedor modified the σ° algorithm to be a continuous function of AGC. The Fedor algorithm is exactly the same as the Seasat GDR algorithm except that the attenuator values C_k in column 2 of Table 3 are replaced with the values given in column 3. The Hancock σ° algorithm fixes $k = 10$ and uses the Seasat values of A_k and C_k in Tables 2 and 3. These two modified σ° algorithms are shown together in Figure 9; they differ only by a relative bias of 0.15 dB. Because of their similarity, there is no strong preference for using one of the algorithms over the other. We prefer the Hancock algorithm because it is simpler. The algorithm for σ° then becomes

$$\sigma^\circ = B - 60.6 + A_s + L_{ant} + 30 \log_{10} (h/h_0)$$

The Seasat σ° values were recomputed from AGC, satellite height, and attitude angle using the Hancock algorithm. A histogram of the resulting corrected σ° values is shown in Figure 10. The bimodal distribution is no longer present and the σ° values are approximately Gaussian. We have no way of proving that this distribution is "correct," but it certainly

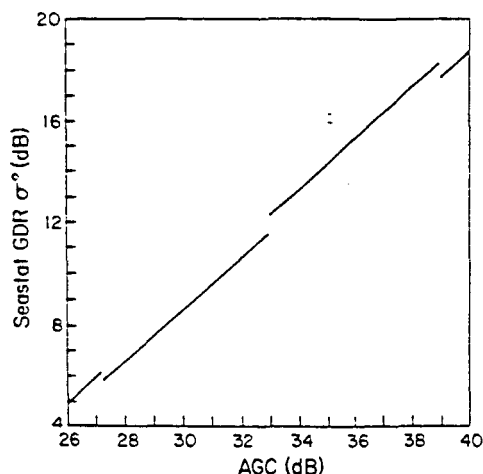


Fig. 8. Automatic gain control (AGC) contribution to σ° in the Seasat GDR algorithm.

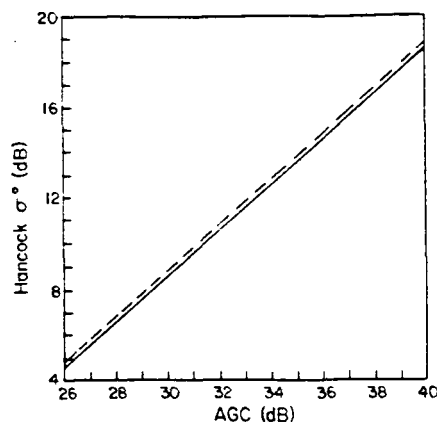


Fig. 9. Hancock (solid line) and Fedor (dashed line) algorithm for AGC contribution to σ° .

seems more reasonable than the bimodal distribution in Figure 7.

Using corrected σ° values, we recomputed wind speeds using the Seasat ALT GDR wind speed model function (see section 4.2). A histogram of the resultant wind speeds is shown in Figure 11. It is evident from Figure 11 that the distribution of ALT wind speeds still exhibits rather peculiar behavior. There are abrupt increases in the wind speed distribution at about 7.8 and 10.0 m s^{-1} . These features cannot be due to problems with the corrected σ° algorithm since the σ° distribution is so smoothly varying (Figure 10). The problems must therefore lie in the wind speed model function.

4.2. Wind Speed Model Function

The roots of the ALT wind speed model function used in the Seasat GDR processing can be traced back to early studies of the relation between the mean square sea surface slope $\langle s^2 \rangle$ and the wind speed. Cox and Munk [1954] suggested a simple linear relationship based on 23 observations. Wu [1972] re-analyzed the Cox and Munk data and suggested a two-branch logarithmic relation between $\langle s^2 \rangle$ and wind speed. One logarithmic relation was proposed for wind speeds less than 7 m s^{-1} , and a second logarithmic relation was proposed for wind speeds greater than 7 m s^{-1} . This two-branch fit was motivated by the dimensionally derived wave number spectrum proposed by Phillips [1966] for a fully developed sea state. From this assumed equilibrium spectrum, Wu derived an expression for $\langle s^2 \rangle$ in terms of a contribution from capillary waves and a contribution from longer gravity waves. He conjectured that at low wind speeds, only the gravity waves contribute to $\langle s^2 \rangle$, while at higher wind speeds, both gravity and capillary waves contribute. Wave components in the capillary

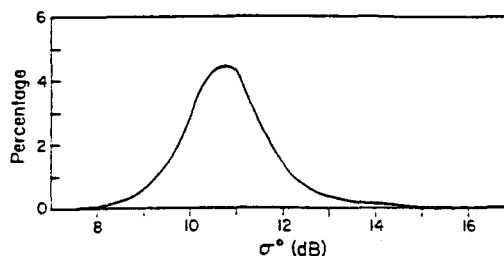


Fig. 10. Histogram of σ° computed from approximately 3 million observations during the full 96-day Seasat mission using the Hancock modified algorithm. Bin size is 0.1 dB.

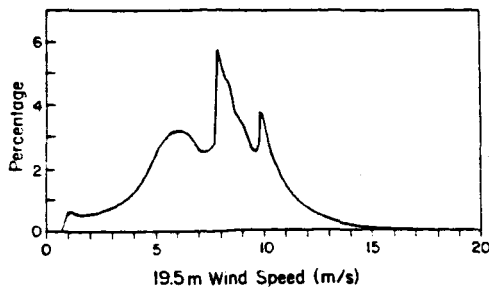


Fig. 11. Histogram of 19.5 m wind speeds computed from approximately 3 million observations during the full 96-day Seasat mission using the Hancock modified σ° algorithm and the Seasat GDR Brown *et al.* [1981] wind speed model function. Bin size is 0.25 m s^{-1} .

range have a larger mean square slope than gravity waves, and $\langle s^2 \rangle$ of capillary waves is much more sensitive to changes in wind speed than $\langle s^2 \rangle$ of longer gravity waves. Justification for the sudden change in regimes at 7 m s^{-1} is not apparent from Wu [1972]. It is also noteworthy that the two-branch logarithmic fit to the 23 Cox and Munk observations of $\langle s^2 \rangle$ does not appear to be a statistically significant improvement over the simpler single branch linear fit.

Brown [1978] showed that the normalized radar cross-section σ° (see section 4.1) for 0° incidence angle microwave backscattering is inversely related to the mean square sea surface slope $\langle s^2 \rangle$. He proposed a two-branch algorithm of the form

$$\sigma^\circ = \frac{0.617}{a \ln u_{10} + b}$$

where u_{10} is the neutral stability wind speed at 10 m above the sea surface. Expressed in terms of decibels,

$$\sigma^\circ(\text{dB}) = -2.1 - 10 \log_{10} (a \ln u_{10} + b)$$

Brown [1979] applied this algorithm to ALT measurements of σ° from GEOS 3 which collected data from April 1975 to December 1978. The GEOS 3 ALT operated at 13.9 GHz but was otherwise very similar to the Seasat ALT in terms of σ° measurements. The constants a and b (see Table 4) in the expression above were evaluated by least squares analysis of 39 ship observations and 19 buoy observations of wind speed. The 9.2 m s^{-1} branch point was selected after conducting numerous numerical experiments. The resulting correlation between measured and estimated wind speed was 0.84 and the rms difference was 2.6 m s^{-1} .

Although we have not conducted such an analysis (since we do not have the in situ data base used by Brown [1979]), we are confident that it would be difficult to justify the two-branch fit using the usual analysis of variance arguments [e.g., Draper and Smith, 1981]. A single-branch algorithm could certainly fit the observations equally well within the bounds of statistical uncertainty from the scatter in the data. Brown's motive for a two-branch algorithm was evidently the theoretic

TABLE 4. Constants in Brown's [1979] Two-Branch Logarithmic Wind Speed Model Function

Wind. Speed, m s^{-1}	a	b
<9.2	0.02098	0.01075
>9.2	0.08289	-0.12664

cal work of Wu [1972]. Note, however, the differences in branch points between the Brown and Wu models.

The reliability of the Brown [1979] two-branch algorithm was clearly very suspect because of the questionable quality and limited quantity of observations used to estimate the parameters a and b . To test further this early model, Brown *et al.* [1981] compared GEOS 3 measurements of σ° with additional high-quality buoy observations of wind speed. A total of 184 matches were identified within 110 km and 1.5 hours. They found that the parameters in the original two-branch model did not adequately fit the expanded in situ data set. In particular, in the vicinity of the branch point (9.2 m s^{-1}), wind speeds estimated from the two-branch algorithm were somewhat low. Brown *et al.* therefore conducted another series of numerical experiments to obtain a model which yielded lower mean square error. They ultimately settled on a three-branch algorithm of the same form as the earlier two-branch algorithm. The coefficients a and b evaluated by least squares analysis of the 184 buoy observations are given in Table 5.

As with the earlier two-branch algorithm, it is our opinion that the three-branch algorithm is difficult to justify in view of the large scatter in the observations. For example, the range of σ° values for wind speeds around 8 m s^{-1} was 3 dB. Again, we do not have the in situ data base used by Brown *et al.* [1981] to conduct such an analysis, but we are confident that an analysis of variance would conclude that the error variance for the three-branch algorithm is, at best, only marginally improved over a simple single branch algorithm.

In order to estimate wind speed from a given measurement of σ° , the three-branch algorithm must be inverted. Using the values of a and b in Table 5, the estimated 10 m wind speed is

$$\hat{u}_{10} = \exp [(S - b)/a]$$

where

$$S = 10^{-[\sigma^\circ(\text{dB}) + 2.1]/10}$$

Over the 184 data points, the correlation between \hat{u}_{10} and the observed u_{10} was 0.89 with an rms error of 1.86 m s^{-1} .

Brown *et al.* [1981] constructed a histogram of the errors and found them to be somewhat skewed from a Gaussian distribution. They therefore introduced a second stage to the wind speed model function which applied a fifth-order polynomial correction to the wind speed estimated from the three-branch model function,

$$\hat{u}_{10}^c = \sum_{n=1}^5 c_n \hat{u}_{10}^n$$

This polynomial correction was applied only for wind speeds less than 16 m s^{-1} . The coefficients c_n , determined by minimizing the mean square error are given in Table 6. This polynomial correction succeeded in achieving errors distributed more symmetrically about zero but did not improve the correlation between estimated and observed wind speeds.

The wind speed model function proposed for GEOS 3 ALT

TABLE 5. Constants in Brown *et al.*'s [1981] Three-Branch Logarithmic Wind Speed Model Function

Wind Speed, m s^{-1}	σ° , dB	a	b
<7.87	>10.9	0.01595	0.017215
7.87-10.03	10.12-10.9	0.039893	-0.031996
>10.03	<10.12	0.080074	-0.124651

was thus a two-stage procedure. The wind speed was first estimated using a three-branch logarithmic model function. A fifth-order polynomial correction was then applied to obtain an improved estimate of wind speed.

Since the basic functions of the Seasat and GEOS 3 altimeters were the same, *Fedor and Brown* [1982] proposed applying the *Brown et al.* [1981] GEOS 3 wind speed algorithm to the Seasat σ° measurements. This required a calibration of σ° measurements by the two instruments in order to eliminate any relative bias. The GEOS 3 mission (April 1975 to December 1978) entirely overlapped the 96-day Seasat mission (July 7, 1978, to October 10, 1978). The two data sets were searched to identify points where Seasat and GEOS 3 ground tracks intersected within 1 hour. Owing to data storage limitations, GEOS 3 essentially sampled only the northeast Pacific, the western Atlantic, and the Gulf of Mexico during the time period of the Seasat mission [see *Chelton*, this issue] so the range of environmental conditions available for comparison with Seasat data was quite limited. A total of 20 ground track intersections was found. One of these was eliminated because of an anomalously large discrepancy between Seasat and GEOS 3 measurements of σ° . The remaining 19 observations covered only a range from 10 to 13 dB (with one observation at 15 dB). Over these 19 pairs of σ° measurements, Seasat was found to be biased high by 1.6 dB with a standard deviation of 0.37 dB.

In spite of the questionable reliability of this bias estimate because it was based on so few observations and over such a limited range of σ° , the 1.6-dB bias was incorporated in the Seasat ALT wind speed algorithm. The *Brown et al.* [1981] GEOS 3 three-branch logarithmic algorithm with fifth-order polynomial correction was then applied directly to the corrected Seasat data using the parameters defined in Tables 5 and 6. To be consistent with the other wind sensors on Seasat (SASS and SMMR), the 10-m wind speeds estimated by the GEOS 3 algorithm were converted to a height of 19.5 m. Using a neutral stability wind profile, this results in

$$\hat{u}_{19.5} = 1.06 \hat{u}_{10}$$

Thus the ALT wind speed algorithm used in the Seasat GDR processing was not based on any direct comparison between Seasat ALT σ° and in situ measurements of wind speed. Surprisingly, a comparison of ALT estimated wind speed with buoy measurements yielded good results [*Fedor and Brown*, 1982]. This is rather puzzling in view of the fact that the σ° values used in the GDR processing are now known to have been in error (see section 4.1).

Having established the historical development of the Seasat ALT wind speed algorithm, we now wish to determine whether the algorithm can account for the peculiar behavior of the wind speed histogram in Figure 11. The noteworthy features of Figure 11 are sharp peaks at about 8 and 10 m s⁻¹ and valleys at about 7.5 and 9.5 m s⁻¹. The slopes of the two

TABLE 6. Coefficients in Fifth-Order Polynomial Correction to *Brown et al.*'s [1981] Three-Branch Logarithmic Model Function

n	c_n
1	2.087799
2	-0.3649928
3	4.062421×10^{-2}
4	-1.904952×10^{-3}
5	3.288189×10^{-5}

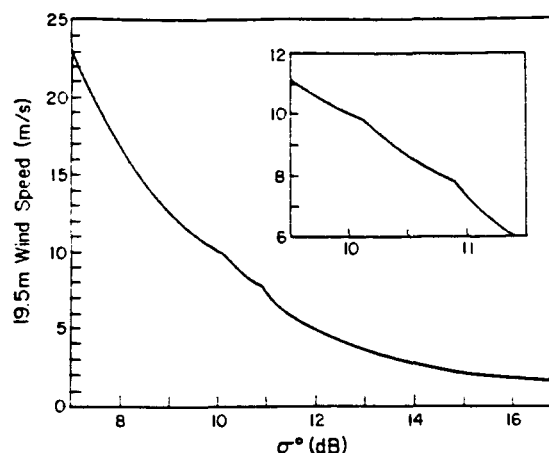


Fig. 12. The *Brown et al.* [1981] three-branch wind speed model function with fifth-order polynomial correction. This model function was implemented in the Seasat GDR processing. Insert shows enlargement of region in vicinity of branch points.

peaks are much steeper on the left side than on the right side. That is, the transitions from valley to peak as wind speed increases are very abrupt.

These abrupt jumps in the wind speed distribution coincide exactly with the two branch points in the three-branch logarithmic wind speed algorithm. This algorithm (with fifth-order polynomial correction), inverted to give the 19.5 m wind speed in terms of σ° , is shown graphically in Figure 12. Note the discontinuous derivatives at the two branch points. The probability density function for $u_{19.5}$ can be expressed in terms of the probability density function for σ° by

$$p(u_{19.5}) = \frac{p(\sigma^\circ)}{|du_{19.5}/d\sigma^\circ|}$$

[see *Bendat and Piersol*, 1971]. Thus, as long $p(\sigma^\circ)$ is smoothly varying (which it is, see Figure 10), then the probability den-

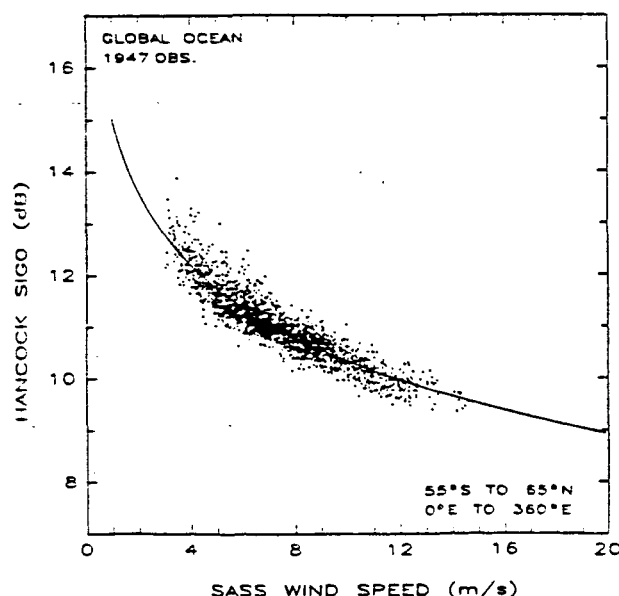


Fig. 13. Scatter plot of global 96-day, nonoverlapping 2° by 6° average σ° (computed using the Hancock modified algorithm) as a function of SASS wind speed (corrected for a 1 m s⁻¹ bias). Continuous curve shows least squares fit to the data (see Table 7).

TABLE 7. Least Squares Fit Parameters (With 95% Confidence Limits) to z Model Function of the Form σ° (dB) = 10[G + H log₁₀ $u_{19.5}$]

Region	Number of 2° by 6° Averages	G	H
Global Ocean	1947	1.502 ± 0.020	-0.468 ± 0.023
Pacific Ocean	1062	1.503 ± 0.026	-0.473 ± 0.032
Atlantic/Indian oceans	885	1.507 ± 0.030	-0.471 ± 0.034
Northern hemisphere	751	1.523 ± 0.031	-0.499 ± 0.041
Southern hemisphere	1196	1.505 ± 0.027	-0.470 ± 0.029

sity of $u_{19.5}$ is inversely related to the magnitude of the slope of the wind speed model function. This accounts for the discontinuities in the wind speed distribution in Figure 11. For each branch point σ_B , the slope of the model function is steeper to the right than to the left of σ_B . Hence there is greater probability of obtaining $u_{19.5}(\sigma_B^-)$ than $u_{19.5}(\sigma_B^+)$. The larger jump in the histogram at 8 m s⁻¹ (corresponding to the 10.9-dB branch point) is explained by the fact that the change in model function slope is larger than at the 10.12-dB branch point (see Figure 12).

We conclude that it is imperative that any model function used to compute wind speed from σ° must have continuous slope everywhere. Thus the Brown et al. three-branch algorithm must be modified. One possibility would be to modify the existing algorithm using a smooth polynomial fit to the Brown et al. curve. However, since the Brown et al. algorithm was derived for the GEOS 3 altimeter and simply implemented on Seasat data (see earlier discussion), there is merit in deriving a new wind speed model function independent of past models.

5. A PROPOSED NEW WIND SPEED MODEL FUNCTION

During the 1960's and early 1970's a number of radar measurements of the sea surface were made from aircraft by the Naval Resesach Laboratory. These measurements were made over a broad range of incidence angles, wind speeds, and wind directions. From off-nadir measurements (incidence angles greater than 15°), the data suggested a power law relationship between the normalized radar cross-section σ° (in real units) and the wind speed [Guinard et al., 1971]. More extensive aircraft measurements made by NASA Johnson Space Center and NASA Langley Research Center supported the empirical power law relationship [Jones and Schroeder, 1978]. A power law relation was therefore adopted to estimate wind speed in the off-nadir regime from the Seasat satellite scatterometer (SASS).

In the near-nadir regime (incidence angles less than 10°), σ° also appeared to obey a power law relation to the wind speed. This was apparently first noted by Daley et al. [1973] from data collected from the NRL flight program. Barrick [1974] found additional support for a power law relation from an analysis of aircraft nadir radar measurements made by Raytheon in 1969 and 1970. Consequently, a power law relation was also adopted for nadir-regime SASS backscatter measurements. If σ° is expressed in decibels the power law relation becomes

$$\sigma^\circ(\text{dB}) = 10[G + H \log_{10} u_{19.5}]$$

where $u_{19.5}$ is the wind speed at 19.5 m above the sea surface. For SASS σ° , the parameters G and H were estimated from least squares analysis of an extensive in situ data base [see Boggs, 1981; Schroeder et al., 1982].

From the discussion in section 4.2, we have shown that

whatever form is chosen for the ALT wind speed model function, it is important that it be continuously differentiable. We propose adopting a model function for ALT with the same form as that used on SASS data. Besides being continuously differentiable, an advantage of this model function is its simplicity compared with the Brown et al. [1981] three-branch algorithm with fifth-order polynomial correction.

As discussed previously, the quantity of high-quality buoy data is too small to estimate the parameters G and H by direct comparison with in situ wind speed measurements (only 14 independent NDBO buoy measurements within 100 km and 1 hour of ALT σ° measurements). We have therefore used the spatial and temporal averaging technique of section 3 to estimate G and H for ALT by comparison with vertically polarized off-nadir SASS wind speed estimates. Based on the results of section 3, we removed a 1 m s⁻¹ bias from the SASS data prior to comparison with ALT measurements of σ° . While we are very aware of the limitations of this method of ALT wind speed model function calibration, we cannot find any viable alternative, given the limited in situ data base available for intercomparison. Tuning to future altimeter missions will clearly require a well-planned in situ measurement program in conjunction with the satellite measurements. Such a measurement program is being coordinated for Geosat.

As in section 3, we chose 2° latitude by 6° longitude and 96-day averages for comparison of σ° from ALT and wind speed from SASS. If we use angle brackets to denote temporal and spatial average, the proposed form for the wind speed model function can be expressed in terms of averages by

$$\langle \sigma^\circ(\text{dB}) \rangle = 10[G + H \langle \log_{10} u_{19.5} \rangle]$$

Note that the wind speed enters the expression as $\langle \log_{10}$

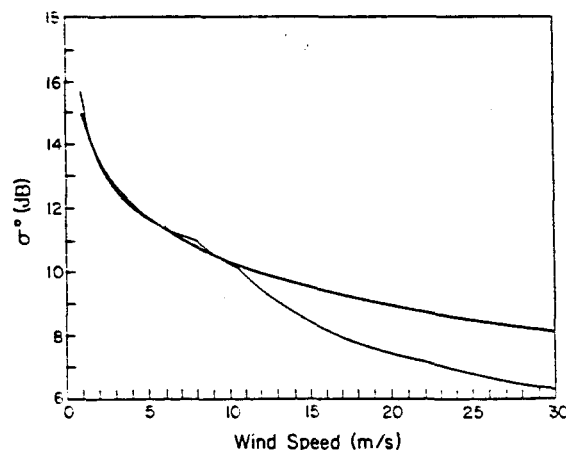


Fig. 14. Comparison of Brown et al.'s [1981] three-branch wind speed model function (thin curve) and the new model function proposed here (heavy curve). The heavy curve is the same as that shown in Figure 13.

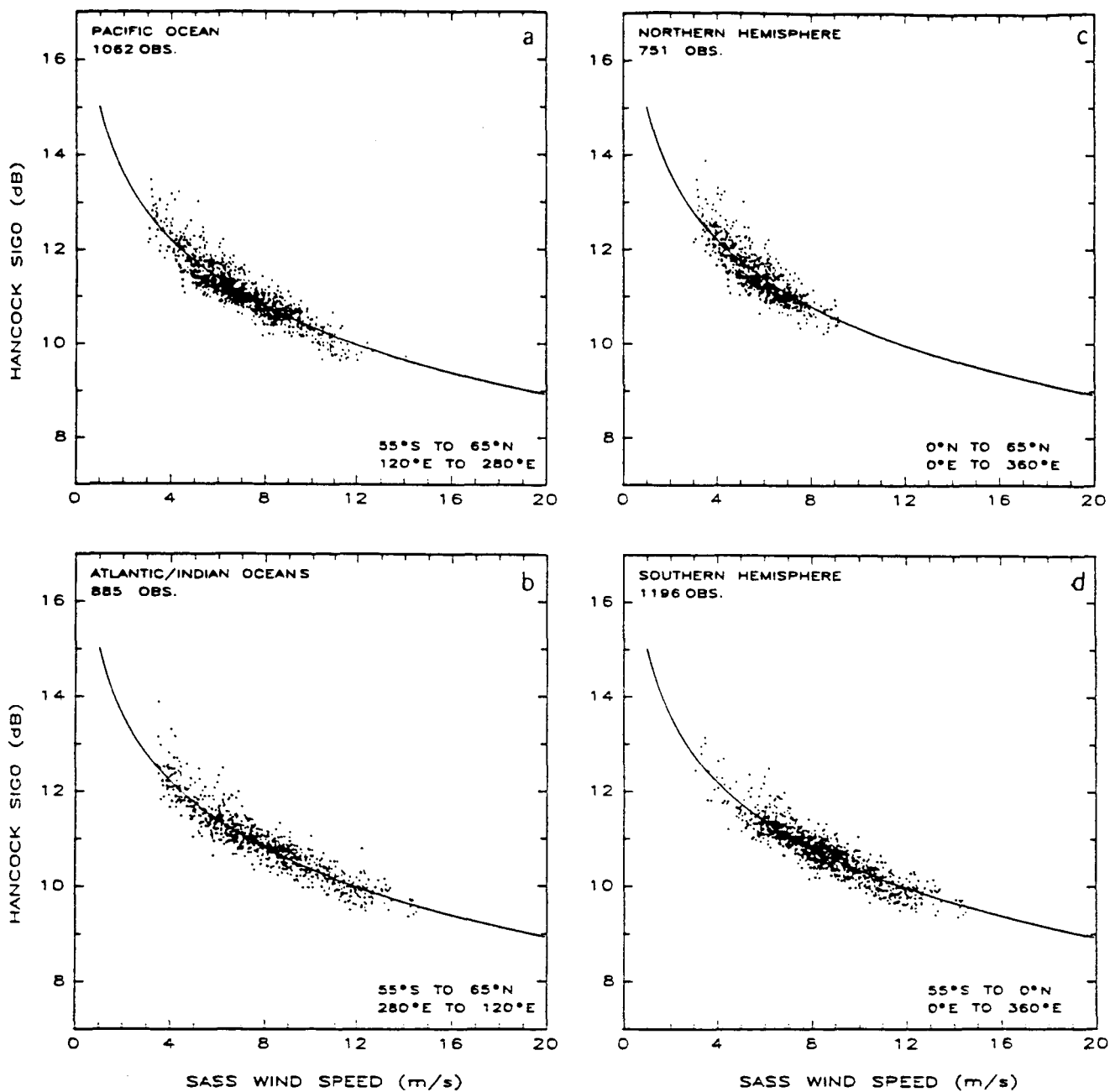


Fig. 15. Same as Fig. 13 except data have been separated into four geographical regions: (a) Pacific Ocean (both hemispheres); (b) Atlantic and Indian oceans (both hemispheres); (c) northern hemisphere (Pacific and Atlantic oceans); (d) southern hemisphere (Pacific, Atlantic, and Indian oceans). Continuous curves represent least squares fit to the global data (see Figure 13).

$u_{19.5}$) and not $\log_{10} \langle u_{19.5} \rangle$; the constants G and H can be carried through the averaging operation, but the logarithm cannot since it is a nonlinear operation.

In our intercomparison, all data within 200 km of land boundaries were excluded to eliminate the possibility of land contamination in the footprint or side lobes of the radar measurements. This 200-km land mask also eliminates much of the data over ice (primarily in the southern hemisphere) which can also result in spurious σ° measurements. As in section 3, only data between latitudes 65°N and 55°S were included.

A scatter plot of global 96-day nonoverlapping 2° by 6° average ALT σ° and SASS $u_{19.5}$ is shown in Figure 13. The solid line in Figure 13 corresponds to our proposed model

function. This curve is based on the least squares parameters estimated from the global data (see Table 7). The error bars in Table 7 correspond to the 95% confidence regions about the estimated parameters (computed using standard methods, see, for example, *Draper and Smith* [1981]). It is evident that the proposed model function fits the data quite well. The rms error about the least squares fit line is 0.26 dB, and the correlation between σ° and the wind speed is 0.92.

For comparison, the new proposed model function is shown in Figure 14 together with the *Brown et al.* [1981] three-branch model function. The two algorithms are very nearly the same for wind speeds less than 10 m s^{-1} . However, for higher wind speeds (corresponding to the third branch of the *Brown et al.* algorithm), the two model functions diverge rap-

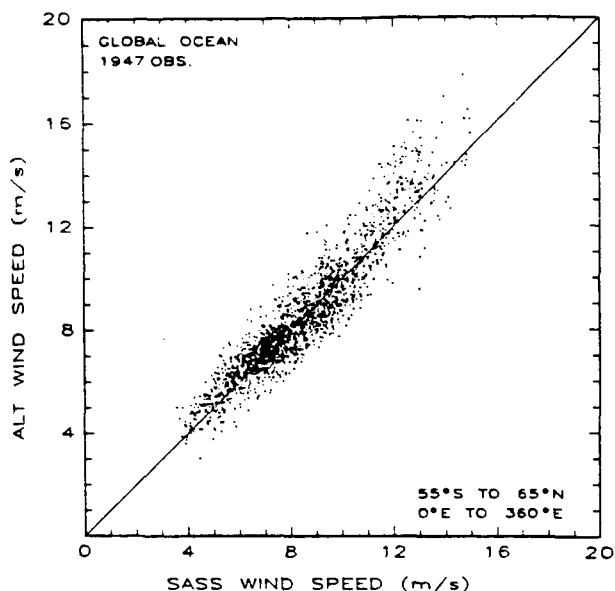


Fig. 16. Scatter plot comparison of 96-day, nonoverlapping 2° by 6° average wind speeds estimated using the proposed new algorithm and SASS wind speeds (corrected for a 1 m s^{-1} bias). Straight line represents perfect fit.

idly. That the two model functions agree at the lower wind speeds is comforting since the preponderance of data (over 90% in both cases) used to derive both model functions fell within the $3\text{--}12 \text{ m s}^{-1}$ range. The discrepancy at higher wind speeds is disturbing. However, because of the paucity of observations in this regime, both model functions must be considered suspect at wind speeds greater than 12 m s^{-1} . In defense of the model function proposed here, we are aware of no physical basis for a sudden increase in sensitivity of σ° to wind speed at around 10 m s^{-1} . We therefore feel that our model function is preferable to the Brown et al. three-branch model function. This hypothesis will be testable with the extensive high-quality in situ measurement program planned for Geosat.

It is useful to investigate the stability of the proposed new wind speed model function to gain some feeling for its reliability. One method of achieving this is to examine the performance of the model function in different geographical regions. In Figure 15, the global 96-day, 2° by 6° average data have been separated into four geographical regions: Figure 15a, Pacific Ocean (both northern and southern hemispheres); Figure 15b, Atlantic and Indian oceans (both northern and southern hemispheres); Figure 15c, northern hemisphere (Pacific and Atlantic oceans); and Figure 15d, southern hemisphere (Pacific, Atlantic, and Indian oceans). In all four plots, the solid line corresponds to the model function derived for the global data set (Figure 13). It is apparent that the single model function fits the data in all four regions very well.

For comparison, the least squares fit of parameters G and H estimated separately for each region are given in Table 7. In all cases, the G and H values computed from the global data fall easily within the error bars of the G and H values computed separately for each of the four geographical regions. The worst case is the northern hemisphere region. However, this is the least reliable of the four regions because of the very limited range of the observed wind speeds ($4\text{--}8 \text{ m s}^{-1}$). This is reflected in the larger error bars on the H coefficient (see Table 7). In the other three regions, the observations cover a broader

range of wind speeds due to strong austral winter winds in the southern hemisphere during the Seasat mission. The estimated coefficients G and H are consequently more reliable.

We conclude that the G and H values derived for the global data set are an adequate representation in all geographical regions. Inverting the proposed algorithm to obtain the 19.5-m wind speed from measurements of σ° gives

$$u_{19.5} = 10^{[(\sigma^\circ(\text{dB})/10 - G)/H]}$$

A scatter plot comparison of 96-day, 2° by 6° average SASS wind speed (corrected for a 1 m s^{-1} bias) and ALT wind speed (computed from σ° corrected using the Hancock algorithm) is shown in Figure 16. The correlation between the two estimates of wind speed is 0.94 over a range from 4 to 15 m s^{-1} . The slope of the least squares fit straight line is 1.005 ± 0.048 with an offset of $(0.084 \pm 0.409) \text{ m s}^{-1}$ and an rms error of 0.82 m s^{-1} .

From Figure 16, there is a suggestion that the proposed model function may be overestimating wind speeds in excess of 12 m s^{-1} . Alternatively, SASS could be underestimating these high wind speeds. Since the number of comparisons at these high wind speeds is small, the statistical significance of the discrepancy is questionable. The discrepancy at high wind speeds could be eliminated with a polynomial correction of the sort used in the Brown et al. [1981] wind speed model function. However, since it is not yet known whether the error lies in ALT or SASS wind speed estimates, we prefer not to apply a polynomial correction at this time. The Geosat in situ measurement program should resolve this apparent discrepancy at high wind speeds.

As a final point, the effect of the new model function on the distribution of wind speeds is shown in Figure 17. The peculiarities evident in Figures 5 and 11 are no longer present; the distribution varies smoothly over the full range of wind speeds. The peak in the distribution is at about 7.5 m s^{-1} , and the overall average value and standard deviation are 8.5 and 4.6 m s^{-1} , respectively.

6. DISCUSSION AND CONCLUSIONS

The launch of the U. S. Navy altimetric satellite Geosat scheduled for February 1985 has motivated an in-depth investigation of wind speed estimation from ALT measurements of radar backscatter. ALT wind speed retrieval is a two-step procedure. In the first step (see section 4.1), the normalized radar cross-section σ° is computed from receiver gain (AGC), satellite attitude angle and satellite height. In the second step (see section 4.2), the wind speed is computed from σ° . In our study

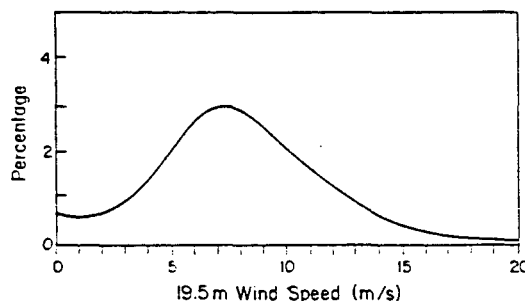


Fig. 17. Histogram of 19.5-m wind speeds computed from approximately 3 million observations during the full 96-day Seasat mission using the Hancock modified σ° algorithm and the new proposed wind speed model function. Bin size is 0.25 m s^{-1} .

of ALT wind speed estimation from Seasat, we identified problems with both steps of the procedure.

The most fundamental problem is an error in the σ° algorithm implemented in Seasat ALT geophysical data record (GDR) processing which resulted in a discontinuous dependence of σ° on AGC. When this algorithm is corrected to remove all discontinuities, the resulting values of σ° are much more reasonable than those produced in the Seasat GDR's. The corrected algorithm (suggested by D. Hancock (personal communication, 1983)) is much simpler than the Seasat GDR σ° algorithm (section 4.1).

The wind speeds computed from corrected σ° still exhibit rather peculiar behavior. The Seasat GDR wind speed model function was adopted from the GEOS 3 algorithm derived by Brown *et al.* [1981]. In this algorithm, the wind speed is first estimated from a three-branch model function and then corrected with a fifth-order polynomial adjustment. We traced the peculiar behavior of computed wind speeds to discontinuous derivatives at the two branch points of the three-branch model function.

In this paper, we have proposed a new model function for wind speed estimation from corrected values of σ° . The proposed model function has the same functional form as that used on Seasat SASS data. If σ° is expressed in decibels, the new model function estimates the wind speed at 19.5 m by

$$\hat{u}_{19.5} = 10^{((\sigma^\circ(\text{dB})/10 - G)/H)}$$

where

$$G = 1.502$$

$$H = -0.468$$

The parameters G and H were estimated by least squares from a comparison of global 96-day, 2° by 6° averages of ALT σ° with vertically polarized, off-nadir SASS wind speed. The SASS wind speeds were corrected for a 1 m s^{-1} bias which was evidently introduced into the Seasat SASS GDR processing due to calibration to an erroneous wind recorder in JASIN.

The proposed model function of course produces ALT wind speeds which are consistent with SASS wind speeds. For the global 96-day, 2° by 6° averages, the correlation between ALT and SASS wind speed is 0.94, and the rms difference is 0.82 m s^{-1} . A distinct advantage of this technique for ALT and SASS wind speed comparison is that the averaging removes any

random component of error in individual estimates of wind speed. It should be born in mind that the validity of the proposed algorithm has only been demonstrated on spatially and temporally averaged data.

A natural question that arises is whether the proposed algorithm adequately describes instantaneous ALT estimates of wind speed. A rigorous test of performance on individual measurements of σ° requires an extensive high-quality in situ data base for comparison. Using the NDBO buoy data base, we were able to identify only 14 independent buoy observations of wind speed within 100 km and 1 hour of Seasat ALT σ° measurements. This is clearly too few for a meaningful intercomparison. The extensive in situ measurement program planned for Geosat will correct this situation and allow an independent assessment of the proposed wind speed model function.

An alternative approach which yields some information on model function performance on instantaneous measurements is to determine the rms error of ALT σ° measurements. We examined the global Seasat ALT data base and determined that the point-to-point rms error was 0.3 dB. The effects of this measurement noise are shown in Figure 18. The dashed lines show the wind speed estimated with a 0.3-dB error in the measurement of σ° . Retrieval of low wind speeds is relatively insensitive to errors in measurement of σ° . However, at high wind speeds, errors in measurement of σ° result in very poor estimates of wind speed. For example, a +0.3-dB error in σ° at 20 m s^{-1} results in an estimated wind speed of 24 m s^{-1} . Even at moderate wind speeds of 8 m s^{-1} , a +0.3-dB error in σ° yields an estimated wind speed of 9.5 m s^{-1} .

We conclude that Seasat ALT σ° measurement error is too large to provide reliable instantaneous estimates of wind speed. It seems to us that ALT wind speed estimates will only be useful when the data are temporally and spatially averaged. We have used 96-day, 2° by 6° averages in this study. The lower limits of averaging are the subject of further investigation. This problem is unfortunately addressable to only a limited degree from Seasat data because of intermittent sampling by ALT during the 96-day mission.

One final caveat in the proposed model function is that it is based on very few comparisons at wind speeds higher than 12 m s^{-1} . Thus the validity of the model function is suspect at these high wind speeds. This can only be resolved from a carefully coordinated in situ measurement program such as that planned for Geosat.

Acknowledgments. We would like to acknowledge F. Wentz for helpful discussions throughout this project and D. Hancock for the use of his unpublished σ° algorithm. M. Freilich and an anonymous reviewer contributed valuable criticism and comments on an early version of this manuscript. We thank F. Kuykendall for writing and implementing a wonderfully efficient computer program for identifying matches between satellite and buoy wind speed measurements. Finally, we would also like to thank Pam Wegner for typing the manuscript. This work was carried out at Oregon State University and the Jet Propulsion Laboratory under NASA contract NAS7-100. The Jet Propulsion Laboratory's Pilot Ocean Data System provided the use of their computer for accessing the Seasat data archives and for the data analysis presented in this paper.

REFERENCES

- Barrick, D. E., Wind dependence of quasi-specular microwave sea scatter, *IEEE Trans. Antennas Propag.*, AP22, 135-136, 1974.
 Barrick, D. E., and C. T. Swift, The Seasat microwave instruments in historical perspective, *IEEE J. Oceanic Eng.*, OES, 74-79, 1980.
 Bendat, J. S. and A. G. Piersol, *Random Data: Analysis and Measurement Procedures*, 407 pp., Wiley-Interscience, New York, 1971.

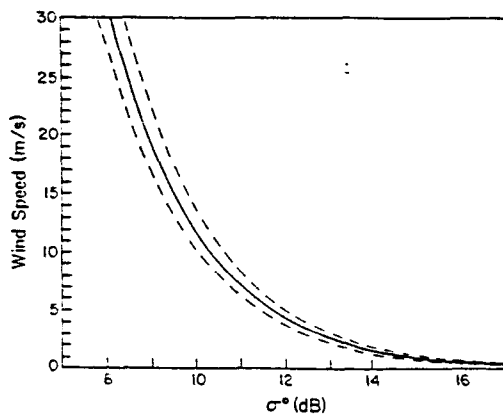


Fig. 18. The proposed new ALT wind speed model function (continuous curve). The dashed lines show the effects on estimated wind speed when σ° is in error by $\pm 0.3 \text{ dB}$.

- Boggs, D. H., The Seasat scatterometer model function: The genesis of SASS-1, *Rep. 622-230*, 30 pp., Jet Propul. Lab., Pasadena, Calif., 1981.
- Brown, G. S., Backscattering from a Gaussian distributed, perfectly conducting, rough surface, *IEEE Trans. Antennas Propag.*, AP26, 472-482, 1978.
- Brown, G. S., Estimation of surface winds speeds using satellite-borne radar measurements at normal incidence, *J. Geophys. Res.*, 84, 3974-3978, 1979.
- Brown, G. S., H. R. Stanley, and N. A. Roy, The wind speed measurement capability of spaceborne radar altimetry, *IEEE J. Oceanic Eng.*, OE6, 59-63, 1981.
- Chelton, D. B., Comments on "Seasonal variation in wind speed and sea state from global satellite measurements," *J. Geophys. Res.*, this issue.
- Chelton, D. B., K. J. Hussey, and M. E. Parke, Global satellite measurements of water vapor, wind speed and wave height, *Nature*, 294, 529-532, 1981.
- Cox, C. S., and W. H. Munk, Statistics of the sea surface derived from sun glitter, *J. Mar. Res.*, 13, 198-227, 1954.
- Daley, J. C., J. T. Ransone, and W. T. Davis, Radar sea return from JOSS-II, *Rep. 7534*, Nav. Res. Lab., Washington, D. C., Feb. 21, 1973.
- Draper, N. R., and H. Smith, *Applied Regression Analysis*, 709 pp., John Wiley, New York, 1981.
- Fedor, L. S., and G. S. Brown, Wave height and wind speed measurements from the Seasat altimeter, *J. Geophys. Res.*, 87, 3254-3260, 1982.
- Fu, L.-L., Recent progress in the application of satellite altimetry to observing the mesoscale variability and general circulation of the oceans, *Rev. Geophys. Space Phys.*, 21, 1657-1666, 1983.
- Guinard, N. W., J. T. Ransone, and J. C. Daley, Variation of the NRCS of the sea with increasing roughness, *J. Geophys. Res.*, 76, 1525-1538, 1971.
- Halpern, D., and R. A. Knox, Coherence between low-level cloud motion vectors and surface wind measurements near 0°, 152°W from April 1979 to February 1980, *Atmos. Ocean*, 21, 82-93, 1983.
- Jones, W. L., and L. C. Schroeder, Radar backscatter from the ocean: Dependence on surface friction velocity, *Boundary Layer Meteorol.*, 13, 133-149, 1978.
- Jones, W. L., L. C. Schroeder, and J. L. Mitchell, Aircraft measurements of the microwave scattering signature of the ocean, *IEEE J. Oceanic Eng.*, OE2, 52-61, 1977.
- Liu, W. T., and P. P. Niiler, 1984: Determination of monthly mean humidity in the atmospheric surface layer over oceans from satellite data, *J. Phys. Oceanog.*, 14, 1451-1457, 1984.
- Moore, R. K., and A. K. Fung, Radar determination of winds at sea, *Proc. IEEE*, 67, 1504-1521, 1979.
- Phillips, O. M., *The Dynamics of the Upper Ocean*, Cambridge University Press, New York, 1966.
- Schroeder, L. C., D. H. Boggs, G. Dome, I. M. Halberstam, W. L. Jones, W. J. Pierson, and F. J. Wentz, The relationship between wind vector and normalized radar cross section used to derive Seasat-A satellite scatterometer winds, *J. Geophys. Res.*, 87, 3318-3336, 1982.
- Swift, C. W., Passive microwave remote sensing of the ocean—A review, *Boundary Layer Meteorol.* 18, 25-54, 1980.
- Townsend, W. F., An initial assessment of the performance achieved by the Seasat-1 radar altimeter, *IEEE J. Oceanic Eng.*, OE5, 80-92, 1980.
- Weller, R. A., R. E. Payne, W. G. Large, and W. Zenk, Wind measurements from an array of oceanographic moorings and from F/S Meteor during JASIN 1978, *J. Geophys. Res.*, 88, 9689-9705, 1983.
- Wentz, F. J., V. J. Cardone, and L. S. Fedor, Intercomparison of wind speeds inferred by the SASS, altimeter, and SMMR, *J. Geophys. Res.*, 87, 3378-3384, 1982.
- Wentz, F. J., S. Peteherych, and L. A. Thomas, A model function for ocean radar cross sections at 14.6 GHz, *J. Geophys. Res.*, 89, 3689-3704, 1984.
- Wu, J., Sea surface slope and equilibrium wind-wave spectra, *Phys. Fluids*, 15, 741-747, 1972.
- Wurtele, M. G., P. M. Woiceshyn, S. Peteherych, M. Borowski, and W. S. Appleby, Wind direction alias removal studies of Seasat scatterometer-derived wind fields, *J. Geophys. Res.*, 87, 3365-3377, 1982.

D. B. Chelton, College of Oceanography, Oregon State University, Corvallis, OR 97331.

P. J. McCabe, Jet Propulsion Laboratory, Pasadena, CA 91109.

(Received August 24, 1984;
accepted October 10, 1984.)

Comment on "Seasonal Variation in Wind Speed and Sea State From Global Satellite Measurements" by D. Sandwell and R. Agreen

DUDLEY B. CHELTON

College of Oceanography, Oregon State University, Corvallis

In a recent paper, Sandwell and Agreen [1984; hereafter SA] presented figures of global seasonal wind speed and sea state as measured by the GEOS 3 satellite altimeter. Since that time, Chelton and McCabe [1985; hereafter CM] have found that problems exist in the algorithms used to retrieve wind speed from altimeter measurements of radar backscatter. These problems were discovered too late to be of use in the analysis of SA. However, because they have a significant impact on the accuracy of wind speed estimation from altimeters, it is important that they be pointed out now so that the results of SA are not misused. Although the results presented here do not alter many of the conclusions of SA in a qualitative sense, they do become important for any quantitative interpretation of the seasonal winds presented by SA. In addition, the data distribution maps presented here (Figures 3a-3f) are useful for pointing out limitations in other applications of GEOS 3 data (e.g., use of the altimeter sea level measurements to study surface geostrophic currents).

A detailed description of sea surface wind speed estimation from radar altimeters is given in CM. Briefly, wind speed retrieval is a two-step procedure. In the first step, the power of microwave radiation backscattered from the sea surface is determined from parameters measured by the altimeter receiver. To account for variations in transmitted power, the return power is normalized by the transmitted power. This normalized radar cross section is usually referred to as σ° . The σ° measurements must be corrected for variations in the attitude angle of the satellite and variations in the height of the satellite above the sea surface.

The second step in wind speed retrieval is to estimate wind speed from σ° . This estimation is based on the principle that the roughness of the sea surface increases with increasing wind speed. The backscattered power measured by the altimeter receiver consists of microwave radiation reflected specularly from the sea surface over an approximate 10-km footprint directly beneath the satellite. As the sea surface roughens, much of the transmitted radiation is specularly scattered away from the radar antenna. Thus wind speed is inversely related to σ° . The algorithms used to estimate wind speed from σ° are purely empirical, based on comparisons with coincident measurements from buoys.

In a detailed investigation of the performance of wind speed estimation from the Seasat altimeter, CM identified problems with both steps of the procedure for wind speed retrieval. For Seasat, the power received by the altimeter antenna was converted to a constant output level for other receiver stages using a digital step attenuator automatic gain control (AGC). Thus σ° can be computed directly from AGC (with the aforementioned satellite attitude angle and height corrections). CM found that the tables used to compute σ° resulted in a dis-

continuous dependence on AGC. This algorithm was incapable of producing σ° values in the range from 11.2 to 12.0 dB, which corresponds to wind speeds from about 5 to 7 ms^{-1} . This error is clearly serious for wind speed estimation, since this wind speed range is very near the peak in a distribution of global wind speeds.

After correcting for the error in the Seasat σ° algorithm, CM still found peculiarities in the estimated wind speeds. These peculiarities were traced to discontinuities in the slope of the model function used to estimate wind speed from σ° . For Seasat, wind speeds were computed from σ° using a three-branch logarithmic model function developed by Brown *et al.* [1981]. The change in the slope of the model function at the two branch points (10.12 and 10.9 dB values of σ°) resulted in abrupt changes in the distribution of wind speeds computed from σ° . CM proposed a new single-branch model function which is very nearly the same as the Brown *et al.* model function for wind speeds less than 11 ms^{-1} (corresponding to the two lower branches of the three-branch algorithm). For higher wind speeds, the two model functions diverge rapidly.

Wind speed retrieval from the GEOS 3 ALT differed from the Seasat ALT both in the hardware configuration and in the algorithm used to estimate wind speed from σ° . On GEOS 3, the backscatter was measured directly using an analog receiver. (This was changed on Seasat to a digital system because of calibration problems inherent in analog systems.) Since σ° was measured using an analog system, wind retrieval from GEOS 3 should be immune from errors of the type found in the Seasat σ° algorithm (aside from calibration problems with the analog system).

However, the nature of the algorithm used to compute wind speed from GEOS 3 measurements of σ° does introduce errors in the wind speed. Wind speed estimation was based on a two-branch algorithm proposed by Brown [1979] which had the form

$$\sigma^\circ(\text{dB}) = -2.1 - 10 \log_{10} (a \ln u_{10} + b)$$

where σ° is measured in dB and u_{10} is the wind speed at 10 m above the sea surface. The parameters a and b were evaluated by least squares analysis of a very limited ship and buoy data base. The result was a two-branch algorithm with a branch point at 9.2 ms^{-1} . For the lower wind speed branch, $a = 0.02098$ and $b = 0.01075$. For the upper wind speed branch, $a = 0.08289$ and $b = -0.12664$.

In order to compute wind speed, this algorithm must be inverted, which gives

$$u_{10} = \exp [(S - b)/a]$$

where

$$S = 10^{-[\sigma^\circ(\text{dB}) + 2.1]/10}$$

This model function for wind speed is shown graphically in Figure 1. Note the discontinuous slope of the model function

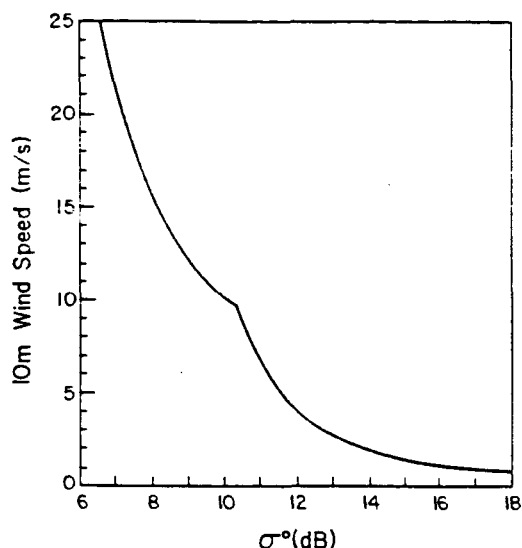


Fig. 1. The *Brown* [1979] two-branch wind speed model function implemented in geophysical processing of GEOS 3 ALT data.

at the branch point at 9.2 ms^{-1} (corresponding to a σ^0 value of 10.3 dB).

(Note: *Brown et al.* [1981] later developed a three-branch algorithm for computing wind speed from σ^0 for the GEOS 3 ALT. This algorithm had exactly the same form as that given above (with branch points at 7.87 and 10.03 ms^{-1}) and was based on an expanded data base consisting of high-quality measurements from National Data Buoy Office buoys. The three-branch algorithm was implemented in geophysical processing of the Seasat ALT data but was not used in the final geophysical processing of GEOS 3 ALT data.)

Problems with the *Brown* [1979] two-branch wind speed model function are easily identified with a simple histogram of wind speeds from the GEOS 3 ALT (Figure 2). There is an abrupt change at 9.2 ms^{-1} in the global distribution of wind speeds. Based on the results of CM, this abrupt change is due to the discontinuous slope at the 9.2 ms^{-1} branch point. The approximate factor of 2 change in slope at 9.2 ms^{-1} results in a factor of 2 increase in the number of wind speeds observed in the $9.2\text{--}9.4 \text{ ms}^{-1}$ bin over the $9.0\text{--}9.2 \text{ ms}^{-1}$ bin.

Thus as noted in CM, it is essential that any model function used to compute wind speed from σ^0 be continuously differentiable. Clearly, the GEOS 3 ALT data must be reprocessed using a new model function for wind speed in order to obtain reliable estimates of global winds. A form for the new model function is proposed in CM.

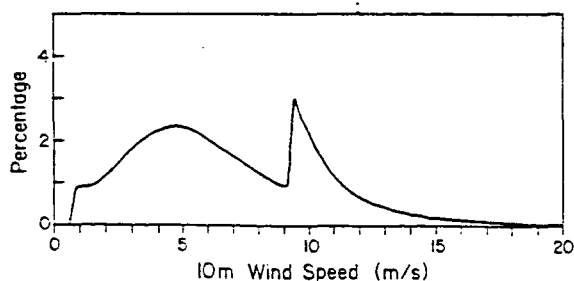


Fig. 2. Histogram of 10-m wind speeds computed from approximately 3.3 million observations during the full $3\frac{1}{2}$ year GEOS 3 mission using the *Brown* [1979] two-branch wind speed model function. Wind speed measurements less than 0.01 ms^{-1} have been excluded. Bin size is 0.2 ms^{-1} .

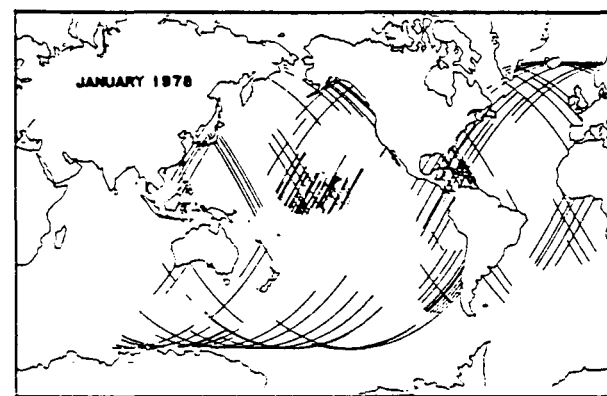
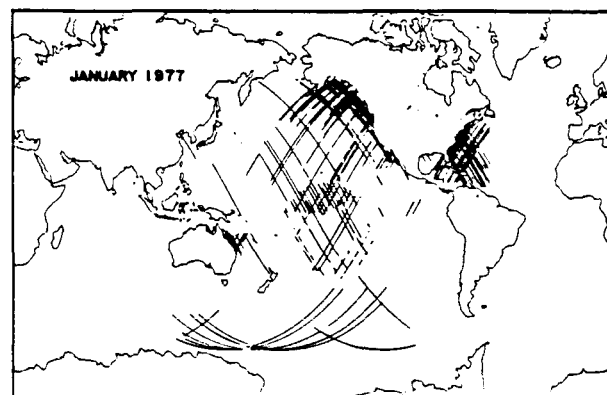
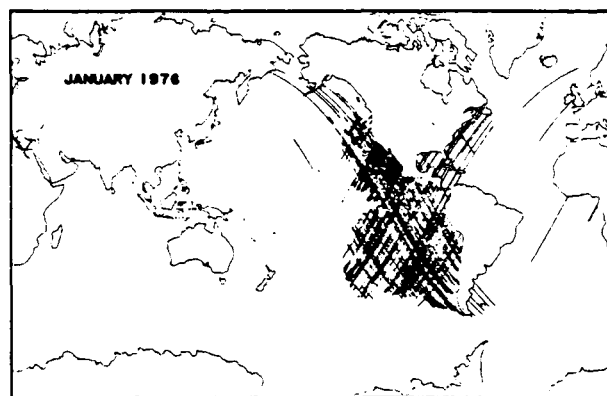


Fig. 3a. GEOS 3 ground tracks during all times when the ALT was turned on during January.

Since a large number of individual wind speed estimates are averaged in each 2° square in the maps presented by SA, a histogram of the average wind speeds will of course not exhibit the abrupt change at 9.2 ms^{-1} . Indeed, according to the Central Limit Theorem, a histogram of averaged winds must be very nearly Gaussian. However, the peak in this distribution will be biased toward a lower wind speed than for averages of individual winds computed using a more accurate model function. (This is not in general true but is true for the case considered here.) Therefore the seasonal wind speeds presented by SA are generally lower than would be obtained if a more accurate model function were used (see Figures 4 and 16 of CM).

Before any steps are taken to reprocess the data, it is useful to examine the spatial and temporal distribution of the GEOS

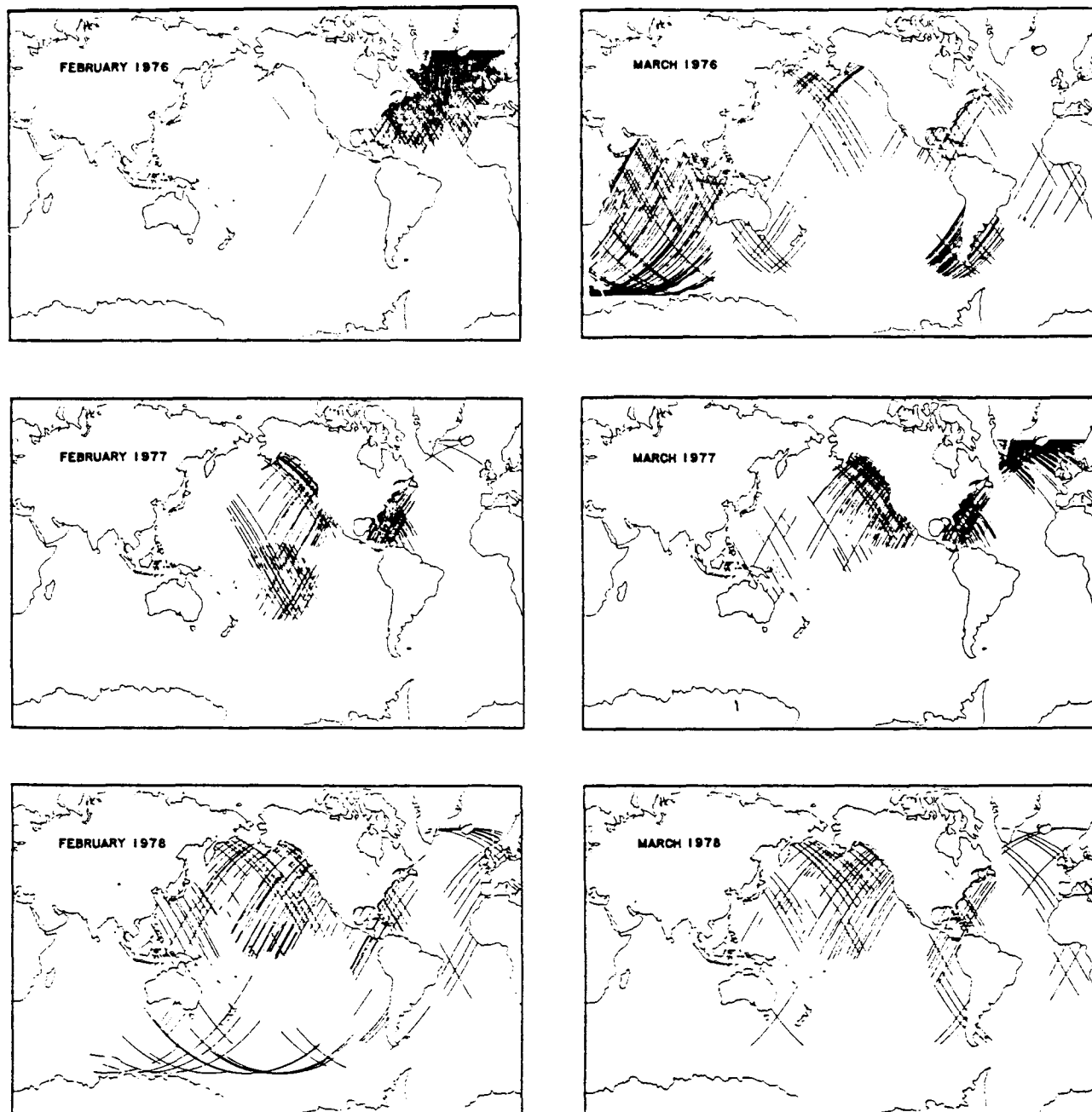


Fig. 3b. As in Figure 3a except for February.

Fig. 3c. As in Figure 3a except for March.

3 ALT σ° measurements in some detail. This information is given to a very limited degree by SA in their global summaries of the number of observations by 2° latitude and longitude regions. They show the total number of boreal winter (which they define to be December, January, February, and March) and summer (defined as June, July, August, and September) observations over the $3\frac{1}{2}$ year GEOS 3 mission (April 1975 to November 1978). A more detailed examination reveals serious limitations in the seasonal wind speeds presented by SA. The GEOS 3 ground tracks during all times when the ALT was turned on are shown in Figure 3 for each individual month during the $3\frac{1}{2}$ year mission.

Some of the salient features of the boreal winter (December, January, February, and March) sampling by the GEOS 3 ALT are:

1. Only the western North Atlantic and eastern North Pa-

cific oceans were sampled every month during the $3\frac{1}{2}$ year GEOS 3 mission.

2. There were very few measurements south of 30°S during any month.

3. The entire Indian Ocean was sampled only during the month of March 1976.

4. The western North Pacific Ocean was sampled by only a very small number of ground tracks in January, February, and March of 1978.

5. The eastern North Atlantic Ocean was sampled by only a very small number of ground tracks in February 1976, December 1977, and February and March 1978.

6. The entire South Atlantic Ocean was essentially unsampled. (SA block out much of this region in their figures, but the reliability of the seasonal mean in regions not blocked out remains questionable.)

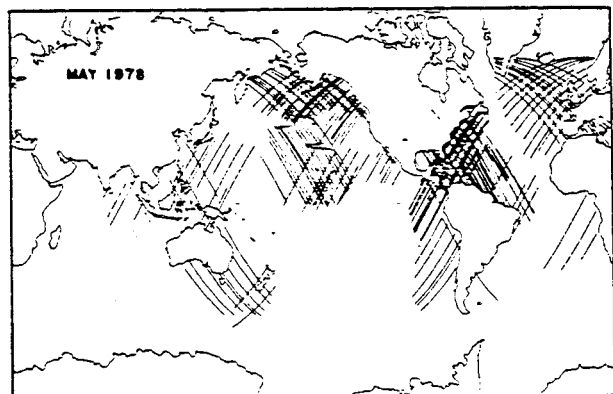
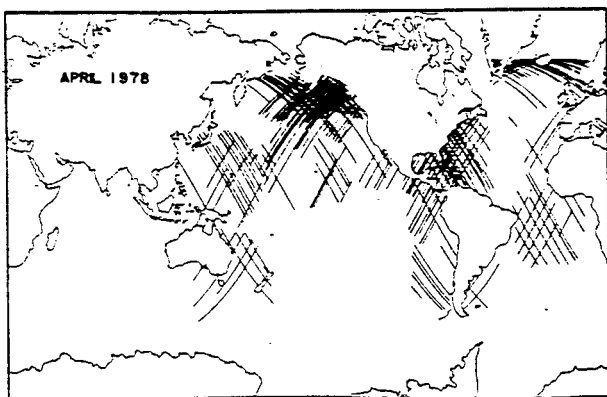
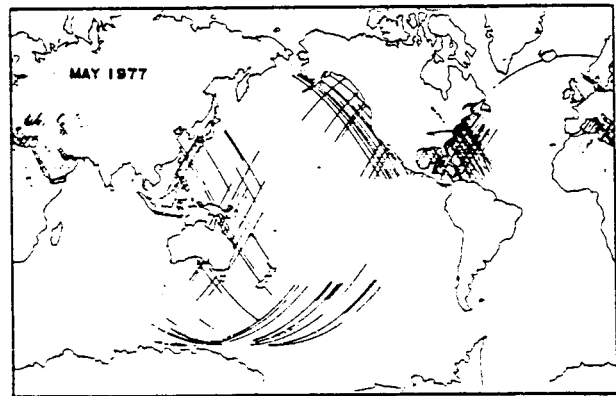
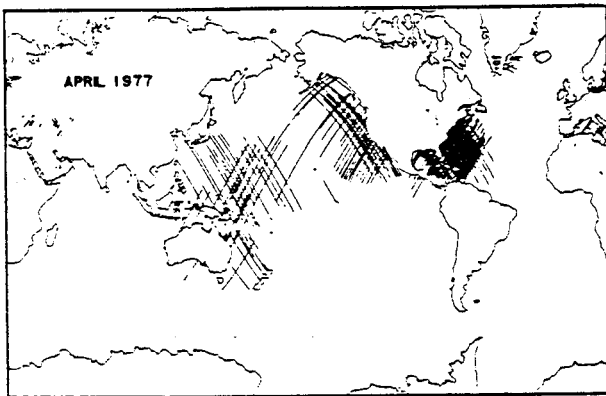
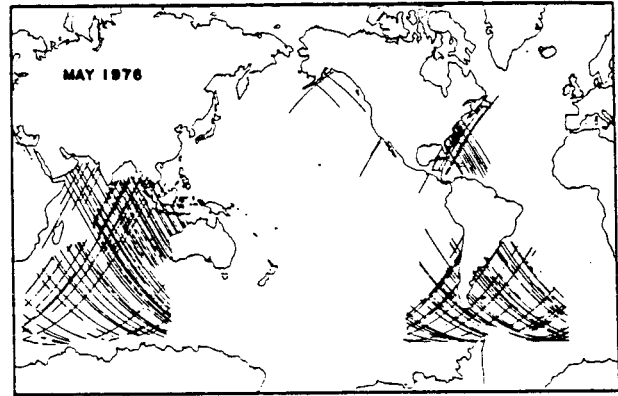
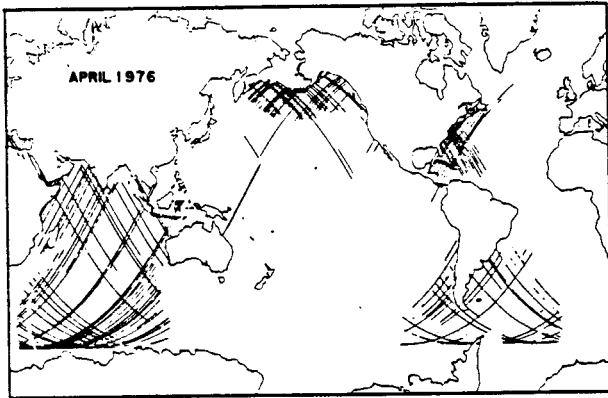
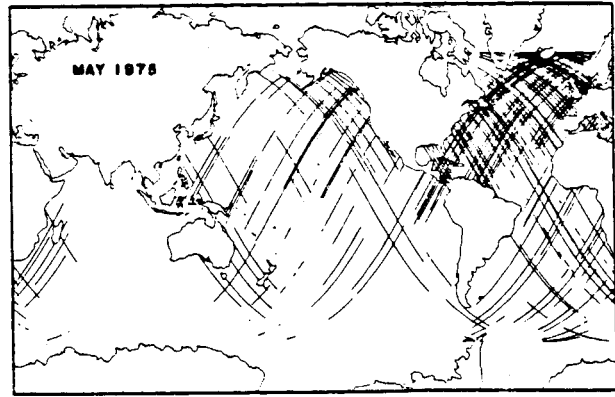
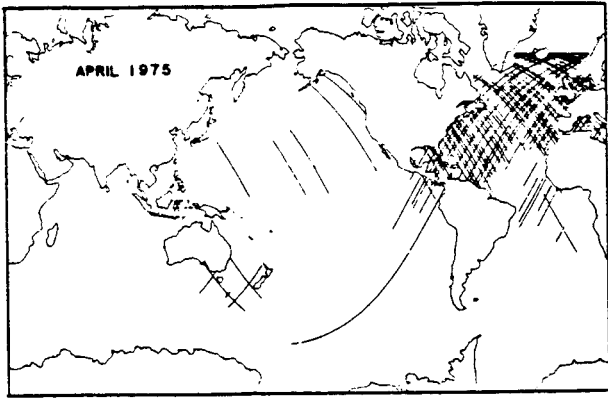


Fig. 3d. As in Figure 3a except for April.

Fig. 3e. As in Figure 3a except for May.

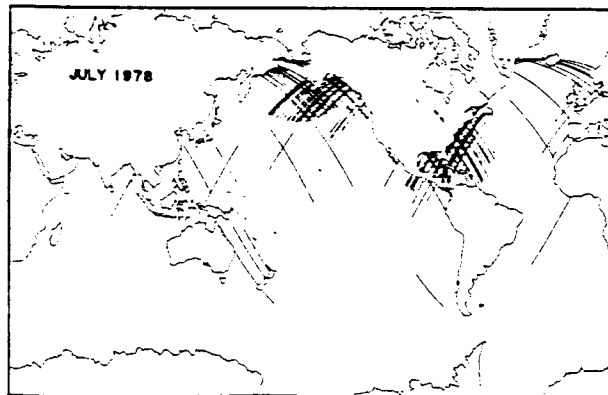
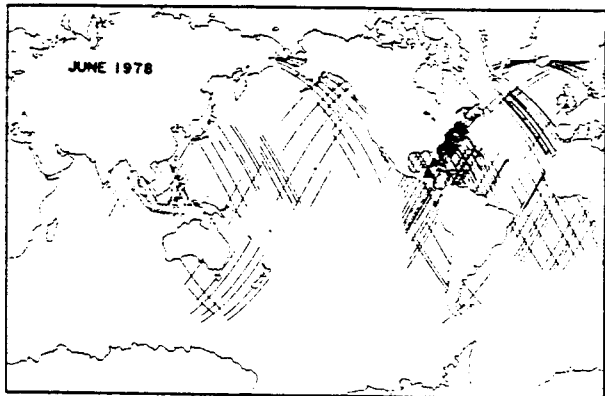
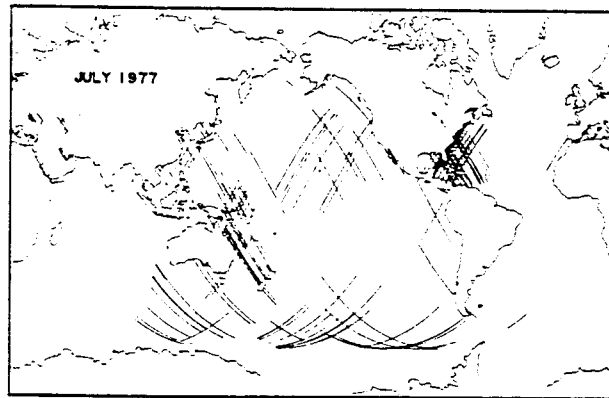
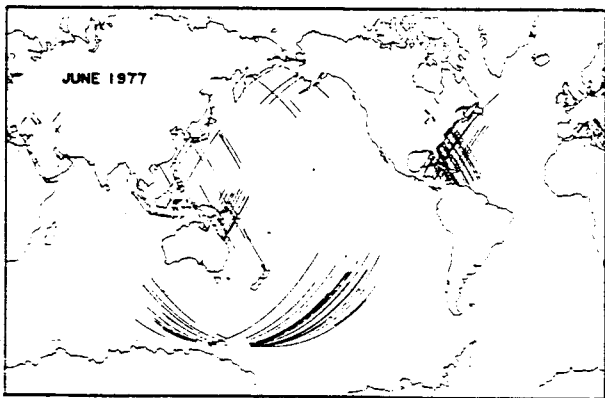
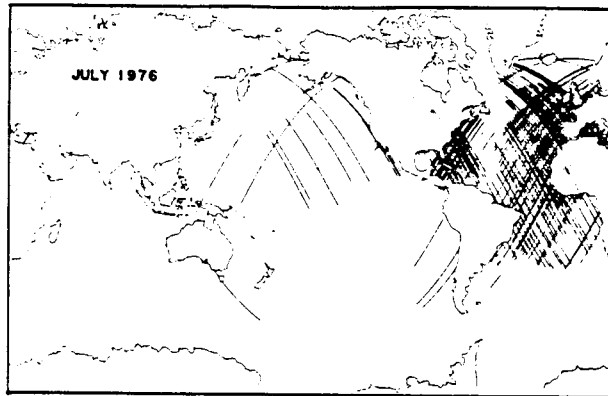
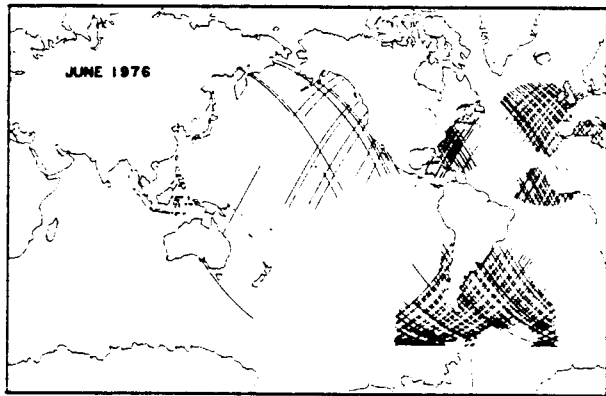
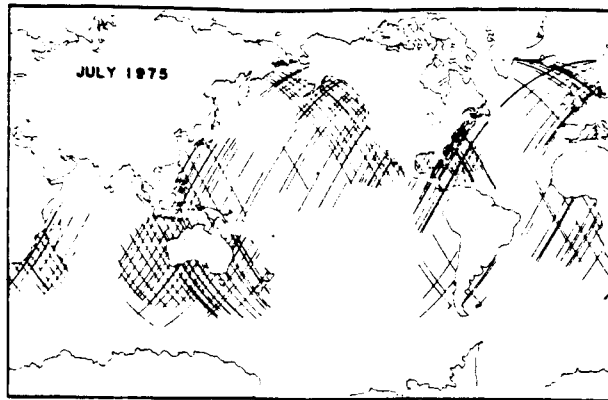
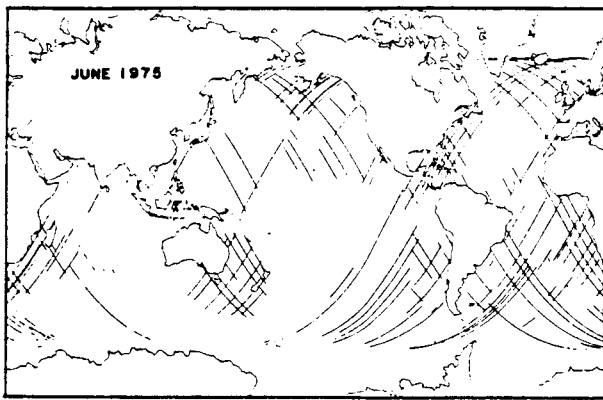


Fig. 3f. As in Figure 3a except for June.

Fig. 3g. As in Figure 3a except for July.

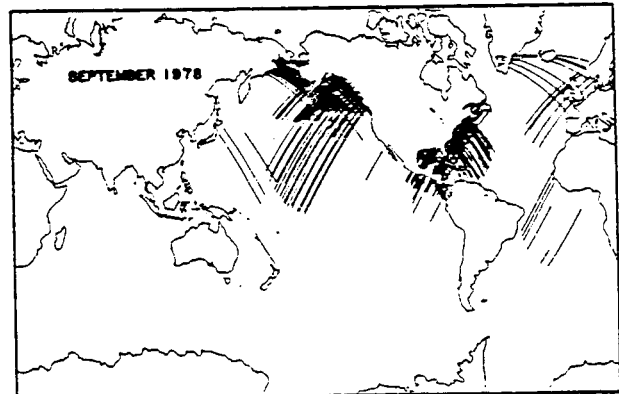
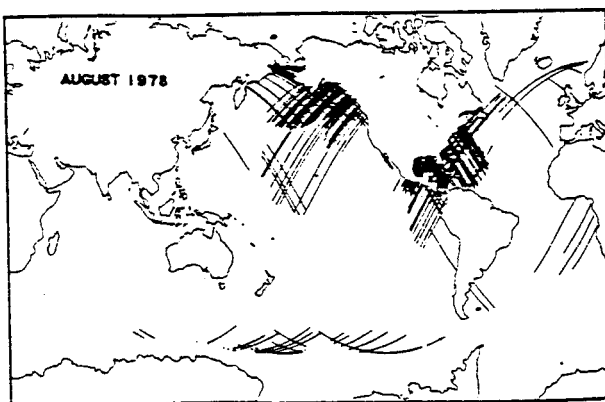
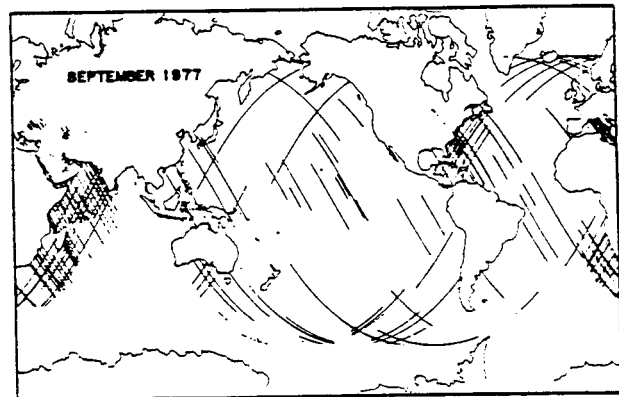
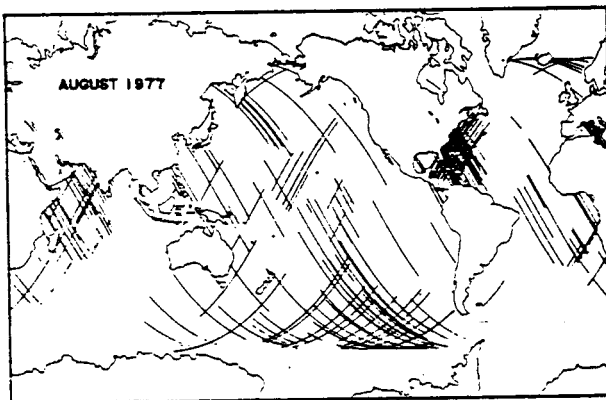
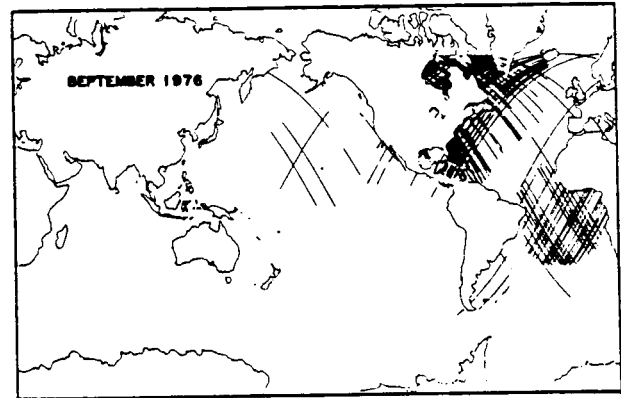
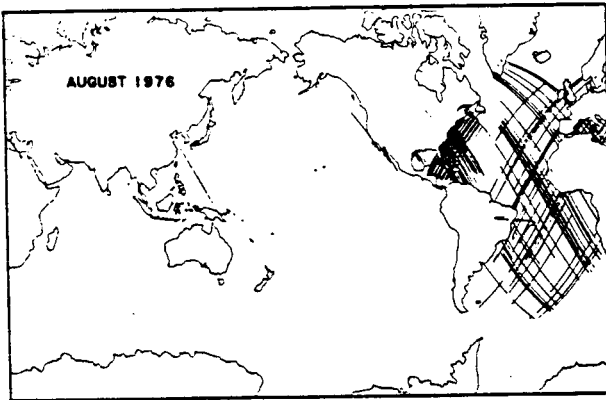
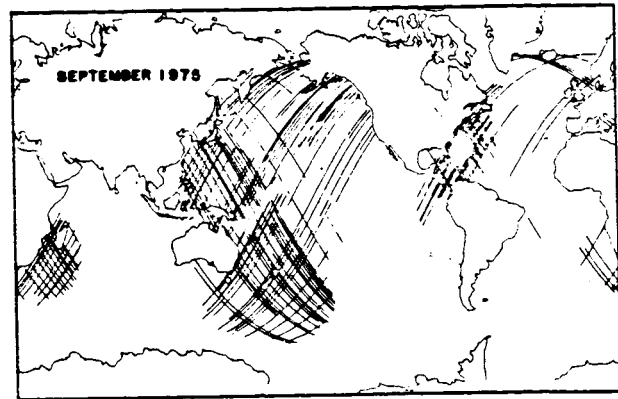
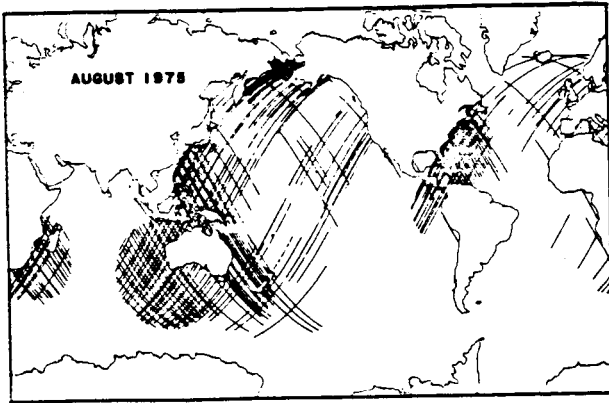


Fig. 3h. As in Figure 3a except for August.

Fig. 3i. As in Figure 3a except for September.

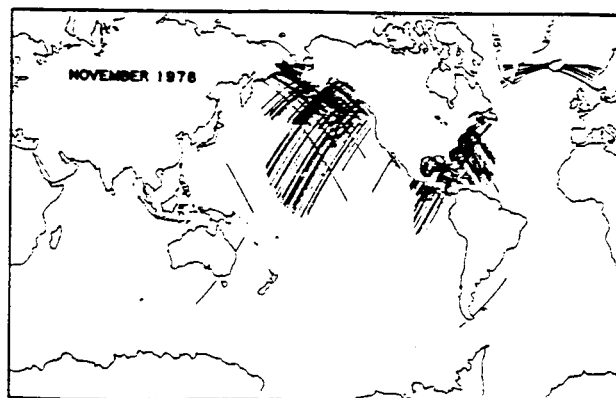
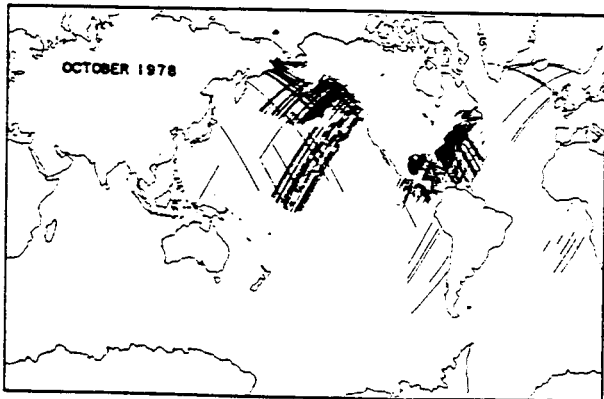
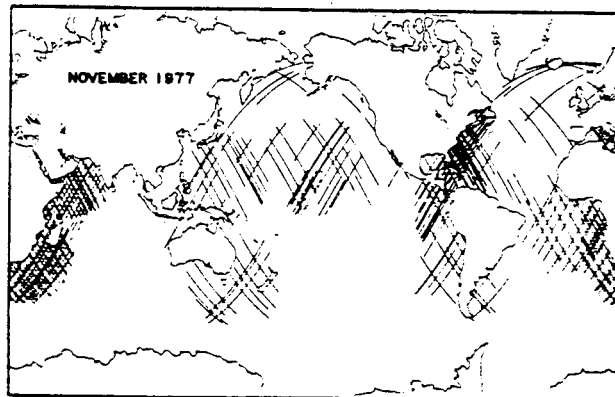
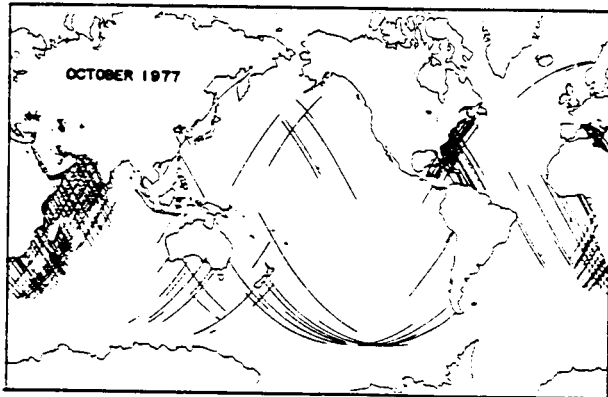
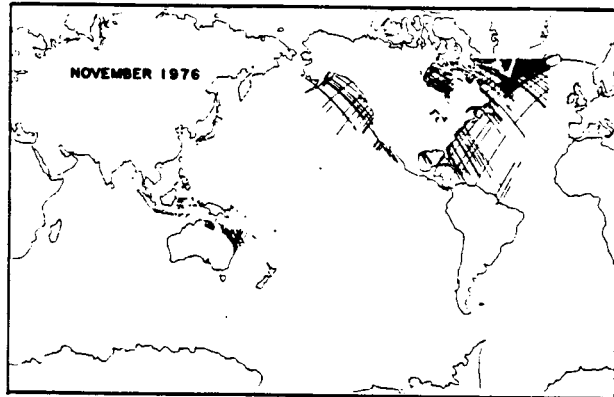
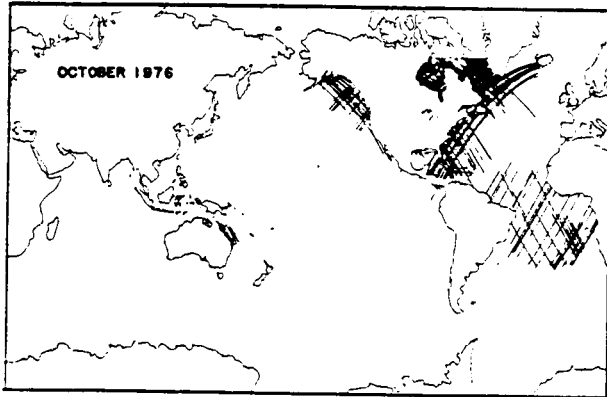
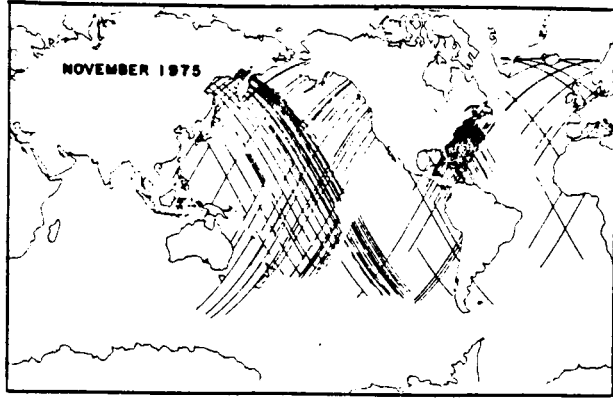
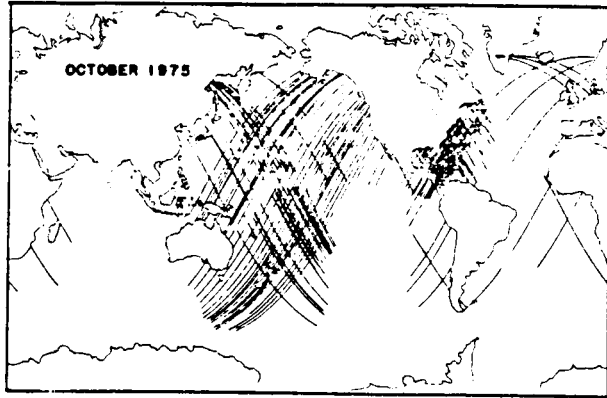


Fig. 3j. As in Figure 3a except for October.

Fig. 3k. As in Figure 3a except for November.

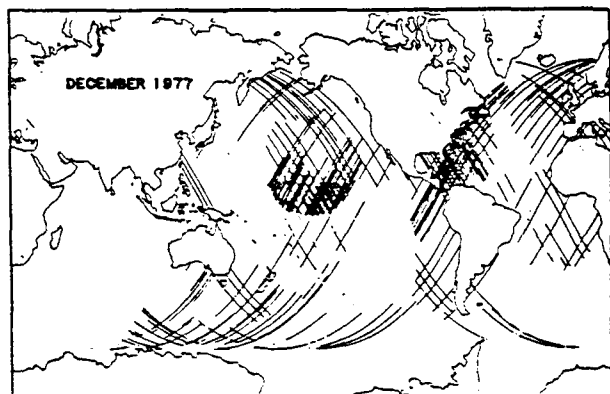
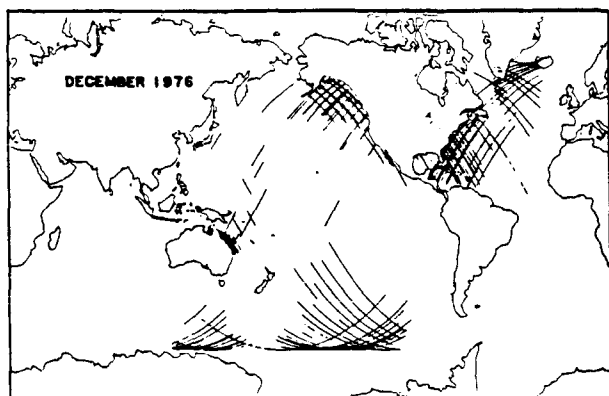
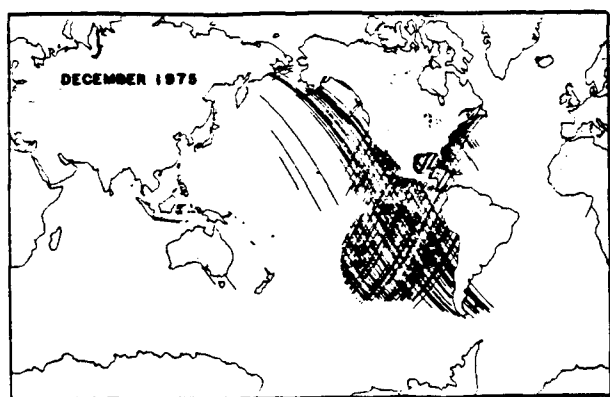


Fig. 3i. As in Figure 3a except for December.

Some of the salient features of boreal summer (June, July, August, and September) sampling by the GEOS 3 ALT are:

1. The western North Atlantic and eastern North Pacific Oceans were sampled nearly every month during the GEOS 3 mission.
2. Again, the number of observations south of 30°S was relatively small.
3. The central and South Indian Ocean was never sam-

pled. (SA block out the southern Indian Ocean but show contours in the central Indian Ocean.)

4. The eastern half of the equatorial Pacific Ocean was essentially unsampled (except for a few ground tracks in August and September 1977).

5. Sampling of the South Pacific Ocean was essentially limited to August 1977 (with a very few ground tracks in June, July, and September 1977).

6. The western South Atlantic Ocean was sampled only in June 1976 (with a few ground tracks in August 1976).

From these figures, it is clear that, except for the western North Atlantic and eastern North Pacific Oceans, the temporal and spatial sampling of the global Ocean by the GEOS 3 ALT was very irregular. In many areas, the seasonal mean values presented by SA are based on measurements taken in different years. Since it is known that there is strong interannual variability in global winds, the representativeness of the seasonal winds in SA is questionable. This is true even in a relative sense where winds in one geographical region are compared with those in another (since the winds in different regions may have been sampled by GEOS 3 in different years).

The conclusion is that patterns of winds presented by SA are, at best, only qualitatively correct because of weaknesses in the two-branch model function for wind speed and irregular temporal and spatial sampling by GEOS 3. It is questionable whether reprocessing GEOS 3 ALT data for wind speed would be useful scientifically for more quantitative examination of global wind speeds. The maps in Figure 3 help identify geographic regions where the mean wind speeds presented by SA are least trustworthy. Although reliable statistics on seasonal winds could probably be computed from GEOS 3 data in a few selected regions (using a corrected single-branch wind speed model function), statistics on global winds would probably not be very meaningful.

Acknowledgments. I would like to thank the Jet Propulsion Laboratory's Pilot Ocean Data System for use of their computer for accessing the GEOS 3 data archive and for the data analysis presented in this paper. This work was carried out at Oregon State University under NASA contract NAS7-100.

REFERENCES

- Brown, G. S., Estimation of surface wind speeds using satellite-borne radar measurements at normal incidence, *J. Geophys. Res.*, **84**, 3974-3978, 1979.
- Brown, G. S., H. R. Stanley, and N. A. Roy, The wind speed measurement capability of space-borne radar altimetry, *IEEE J. Oceanic Eng.*, **OE-6**, 59-63, 1981.
- Chelton, D. B., and J. P. McCabe, A review of satellite altimeter measurements of sea surface wind speed, with a proposed new algorithm, *J. Geophys. Res.*, in press, 1985.
- Sandwell, D. T., and R. W. Agreen, Seasonal variation in wind speed and sea state from global satellite measurements, *J. Geophys. Res.*, **89**, 2041-2051, 1984.

D. B. Chelton, College of Oceanography, Oregon State University, Corvallis, OR 97331.

(Received September 22, 1984;
revised December 1, 1984;
accepted December 14, 1984.)

Temporal Variability of the Antarctic Circumpolar Current Observed from Satellite Altimetry

Abstract. Sea level measurements by the Seasat altimeter were used to study the temporal variability of the Antarctic Circumpolar Current between July and October 1978. Large-scale zonal coherence in the cross-stream sea level difference was observed, indicating a general increase in the surface geostrophic velocity of the current around the Southern Ocean. The result demonstrates the power of satellite altimetry to monitor the variability of large-scale ocean currents.

Recent observations (1, 2) have revealed that there are substantial temporal variations in the mass transport of the Antarctic Circumpolar Current (ACC). The magnitude of the variation (peak-to-peak range) has been estimated to be 40 sverdrups ($1 \text{ Sv} = 10^9 \text{ kg/sec}$), about 30 percent of the mean transport. ACC transport variations of this magnitude

have profound effects on the circulation of the world's oceans, which are important determinants of the global climate (3).

Because synoptic global observations of the ACC are lacking, very little is known about the spatial structure of its temporal variability. For example, what is the zonal scale of the variability? Does

ORIGINAL PAGE
COLOR PHOTOGRAPH

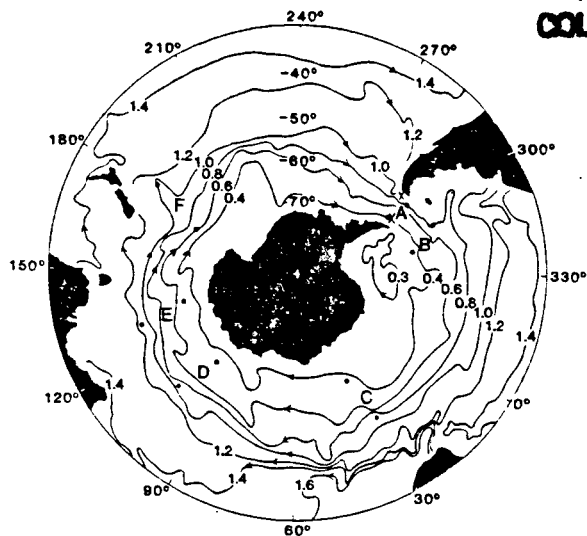


Fig. 1. Long-term averaged sea-surface dynamic topography of the Southern Ocean (11), expressed in dynamic meters relative to the 1000-dbar level. The dots indicate the locations of six pairs of altimeter crossover clusters (A through F), and the x's indicate the locations of two bottom pressure gauges.

areas of approximately 2500 km by 2500 km around the Southern Ocean between 40°S and 65°S. This procedure reduced the root-mean-square (r.m.s.) crossover difference from 146 to 32 cm. After deleting anomalous values greater than 60 cm, the residual r.m.s. crossover difference was reduced to 24 cm, which was still dominated by residual errors from various sources (orbit, sea-state bias, range delays in the media, and ocean tides). Since the time scales of the errors are generally less than a week whereas those of the large-scale oceanic variability are generally greater than a month, the residual crossover differences can be smoothed over a 20-day window to further reduce the errors. This smoothing procedure reduced the r.m.s. residual crossover difference from 24 to 9 cm with an error of 6 cm (8). The resultant smoothed residual crossover differences constitute the data base for the results presented here.

Because of the near-repeat orbit of Seasat, there is a regularly spaced grid of points with a high density of crossovers (referred to here as clusters). We have identified a total of 229 clusters around the ACC, each measuring approximately 200 km by 200 km and containing about 200 crossovers during the 3-month Seasat mission. For each cluster area the crossover adjustment was applied again to remove a constant bias from each track so as to minimize the residual crossover differences. Each resultant bias then effectively represents an along-track average of the time-varying sea level over a distance of ~200 km and hence reflects predominantly the large-scale variability of ocean currents. We thus generated a sea level time series at each cluster by ordering all the resultant biases by their corresponding altimeter overpass times.

To examine the zonal structure of the ACC variability, we have selected six pairs of crossover clusters along the main axis of the flow and computed the sea level difference across the current. The sea level difference between two clusters is proportional to the average surface geostrophic velocity perpendicular to the line segment connecting the two clusters. Displayed in Fig. 1 are the positions of the six pairs of clusters (labeled from A to F) superimposed on a map produced by Gordon *et al.* (11) of the long-term averaged sea-surface dynamic height relative to the 1000-dbar level. The dynamic height is proportional to the stream function of the surface geostrophic flow relative to the 1000-dbar level. The directions of this average relative flow are indicated by the arrows

the transport of the ACC vary in phase around the Southern Ocean? Answers to these questions can come only from global observing systems. The cost of using a network of ships to observe the ACC for an extended period of time would be prohibitive. One of the most promising means of monitoring ocean circulation over large spatial scales is with a satellite radar altimeter system (4).

A radar altimeter measures the altitude of a spacecraft above the sea surface by radio pulse ranging. With an independent knowledge of the height of the spacecraft (the orbit height) referenced to an earth-fixed coordinate system, the height of the sea surface referenced to the same coordinate can be readily obtained. Reviews of the applications of altimetric measurement of the sea surface to the study of ocean currents can be found in the literature (5). We present here some results of an attempt to use the data collected by the Seasat altimeter (6) to study the large-scale temporal variability of the ACC during the 3-month lifetime of Seasat.

The approach used is a variant of the so-called crossover-difference technique (7). A full description of the technique will appear elsewhere (8). A crossover difference refers to the difference between the altimeter measurements made at the intersection of an ascending (northbound) and a descending (southbound) ground track. It comprises three components: orbit error, altimeter measurement error, and true sea level variations. With both orbit and altimeter measurement errors properly corrected, the crossover differences have been used to map the mesoscale variability of ocean currents (7). However, as far as we know, the information contained in the crossover differences has not yet been

exploited to infer the large-scale temporal variability of ocean currents.

Of the various errors contained in the crossover differences, orbit error is by far the most significant. As a first step to reduce orbit error, we applied a crossover adjustment (9) to the Seasat geophysical data records (10) in overlapping

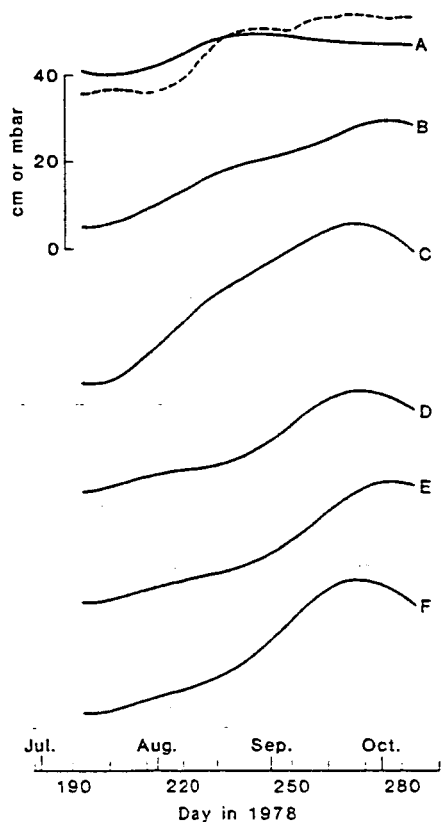


Fig. 2. Time series of the north-south sea level differences (in centimeters) across the six altimeter crossover cluster pairs shown in Fig. 1. The stippled region around each curve represents the r.m.s. error. The dashed line in (A) shows a 20-day running average of the north-south pressure difference (in millibars) across the two bottom pressure gauges (deployed at a depth of 500 m) shown in Fig. 1.

on the figure. The two clusters of pair A are in the vicinity of two bottom pressure gauges (denoted by X's on Fig. 1), which were deployed at a depth of 500 m on the continental slope as part of the International Southern Ocean Study (ISOS) program to monitor the variability of the ACC in the Drake Passage (1). The sea level difference across pair A will be compared with the pressure difference across the two gauges.

The sampling interval of the sea level time series generated from altimeter crossover differences is irregular as a result of the irregular overpass times of the altimeter. To compute the difference between two time series, we interpolated the time series to a common time grid at daily intervals, using the optimal interpolation scheme discussed by Bretherton *et al.* (12). The resultant sea level differences across the six cluster pairs (northern cluster minus southern cluster) for the period from day 193 (12 July) to day 284 (11 October) of 1978 are shown in Fig. 2. The r.m.s. error is indicated by the stippled region around each curve. A rise in the sea level difference implies an increase in the average surface geostrophic velocity between the two clusters. Because each sea level time series is a solution to a difference equation, there is an arbitrary constant associated with each series. This constant was determined here such that each series started from zero at day 193.

The dashed line superimposed on curve A represents a 20-day running mean of the north-south pressure difference (in millibars) between the two bottom pressure gauges (deployed at a depth of 500 m) in the Drake Passage. If the flow variability in the region were due entirely to barotropic motions, then the two curves would match each other to the extent of measurement errors (13). However, the flow variability in the Drake Passage has a substantial baroclinic component (14), which can account for part of the discrepancy between the two curves. In fact, the discrepancy found here is due primarily to the difference between sea level and bottom pressure at the northern side of the Passage, where the flow variability is known to be higher. Nevertheless, the general increase in the pressure difference (about 20 mbar) across the Drake Passage indeed has a counterpart in the sea level difference measured by the altimeter (about 10 cm).

Figure 2 shows that there is some zonal coherence in the increase in the sea level difference across the ACC during the Seasat mission. The net increase in the sea level difference across the

Fig. 3. Color-coded map of the low-frequency (period longer than 20 days) sea level changes measured by the Seasat altimeter over the Southern Ocean between 40°S and 65°S from 12 July to 11 October 1978 (October minus July). The directions of the corresponding change in surface geostrophic velocity are indicated by the arrows. The dots designate the locations of the altimeter measurements used to construct the map.



other five sections is 20 to 30 cm. This change in sea level slope is indicative of an eastward acceleration of the ACC. The variations of the sea level difference across the ACC do not appear to be exactly in phase around the Southern Ocean. Owing to the limited duration of the time series, however, it is not possible to draw any quantitative conclusions about the coherence and phase characteristics of the variability.

Figure 3 is a color-coded map showing the net sea level changes (day 284 minus day 193) at the 229 clusters (indicated by dots) around the Southern Ocean (15). Because the observed sea level variations are basically characterized by linear trends over the 3-month period (16), such a difference map is an effective representation of the variability. The large spatial scales of the variability are clearly evident. During this period, sea level was decreasing over the green areas around Antarctica and increasing over the yellow to brown areas to the north, indicating a general eastward acceleration of the ACC. The directions of the corresponding change in surface geostrophic velocity are indicated by the arrows, showing substantial meridional components in three regions over major topographic features (17): 240° to 270°, 330° to 30°, and 60° to 90°. At longitudes 0° and 90° there are exceptions to the generally eastward acceleration. The large, localized increase in sea level southeast of South America and south of Australia is probably due to local phenomena unrelated to the ACC.

To the best of our knowledge, the results presented here provide the first direct observational evidence for zonal coherence in the temporal variability of the ACC. Moreover, they demonstrate

that even an altimeter with only 1-m accuracy (for the measurement of the sea-surface height) is able to detect large-scale sea level variability with decimeter magnitudes. The shortness of the Seasat data set allows only a glimpse of a phenomenon whose temporal scales are apparently longer than the 3-month data record. Future altimetric missions such as TOPEX (Ocean Topography Experiment) (18), on satellites equipped with improved instruments, hold the promise of providing a more accurate, multiyear view of the large-scale temporal variability of ocean currents such as the ACC.

LEE-LUENG FU

Jet Propulsion Laboratory,
California Institute of Technology,
Pasadena 91109

DUDLEY B. CHELTON

College of Oceanography,
Oregon State University,
Corvallis 97331

References and Notes

1. R. B. Wearn, Jr., and D. J. Baker, *Deep-Sea Res.* 27A, 875 (1980).
2. T. Whitworth III, *J. Phys. Oceanogr.* 13, 2045 (1983).
3. National Research Council, *Ocean Research for Understanding Climatic Variations* (National Academy Press, Washington, D.C., 1983).
4. W. Munk and C. Wunsch, *Philos. Trans. R. Soc. London Ser. A* 307, 439 (1982).
5. C. Wunsch and E. M. Gaposchkin, *Rev. Geophys. Space Phys.* 18, 725 (1980); L.-L. Fu, *ibid.* 21, 1657 (1983).
6. B. D. Tapley, G. H. Born, M. E. Parke, *J. Geophys. Res.* 87, 3179 (1982).
7. R. E. Cheney and J. G. Marsh, *Eos (Trans. Am. Geophys. Union)* 62, 743 (1981); A. L. Gordon *et al.*, *J. Geophys. Res.* 88, 755 (1983).
8. L.-L. Fu and D. B. Chelton, in preparation.
9. In the crossover adjustment we subtracted a bias from each track such that the crossover differences were minimized in a least-squares sense over a given geographical area. Owing to its large spatial scales (~10,000 km), orbit error can be substantially reduced by this adjustment without compromising oceanic signals.
10. Most of the altimeter measurement errors have been partially corrected for in the data [see (6)].
11. A. L. Gordon, E. Molinelli, T. Baker, *J. Geophys. Res.* 83, 2023 (1978).

12. F. P. Bretherton, R. E. Davis, C. B. Fandry, *Deep-Sea Res.* 23, 559 (1976).
13. If the density field remains unchanged as for barotropic motions, a change in sea level of 1 cm causes a change in bottom pressure of ~ 1 mbar.
14. W. D. Nowlin, R. D. Pillsbury, J. Bottero, *Deep-Sea Res.* 28A, 1 (1981).
15. Before contouring, the data were interpolated to a grid 400 km by 400 km and smoothed over adjacent grid points. The resultant rms error for the map is estimated to be less than 4 cm.
16. The correlation coefficient (sea level versus time) averaged over the 229 clusters (weighted by variance) is 0.7 ± 0.3 .
17. See (11) for a bathymetry map.
18. The rms accuracy of the TOPEX altimeter is expected to be 14 cm [see TOPEX Science Working Group, *Satellite Altimetric Measurements of the Ocean* (Publication 400-111, Jet Propulsion Laboratory, Pasadena, 1981)].
19. We thank M. Parke for useful discussions. The ISOS pressure record used in the study was provided by R. B. Wearn. This research was performed at the Jet Propulsion Laboratory, California Institute of Technology, and at Oregon State University under contract with the National Aeronautics and Space Administration.

20 April 1984; accepted 11 June 1984

Observing Large-Scale Temporal Variability of Ocean Currents by Satellite Altimetry: With Application to the Antarctic Circumpolar Current

LEE-LUENG FU

Jet Propulsion Laboratory, California Institute of Technology, Pasadena

DUDLEY B. CHELTON

College of Oceanography, Oregon State University, Corvallis

A new method is developed for studying large-scale temporal variability of ocean currents from satellite altimetric sea level measurements at intersections (crossovers) of ascending and descending orbit ground tracks. Using this method, sea level time series can be constructed from crossover sea level differences in small sample areas where altimetric crossovers are clustered. The method is applied to Seasat altimeter data to study the temporal evolution of the Antarctic Circumpolar Current (ACC) over the 3-month Seasat mission (July–October 1978). The results reveal a generally eastward acceleration of the ACC around the Southern Ocean with meridional disturbances which appear to be associated with bottom topographic features. This is the first direct observational evidence for large-scale coherence in the temporal variability of the ACC. It demonstrates the great potential of satellite altimetry for synoptic observation of temporal variability of the world ocean circulation.

1. INTRODUCTION

It has been increasingly recognized that global measurement of the sea surface topography by satellite altimetry is a viable technique for obtaining quantitatively useful information on the general circulation and variability of surface geostrophic currents of the world ocean [e.g., Munk and Wunsch, 1982]. General descriptions of satellite altimetry can be found in Wunsch and Gaposchkin [1980] and in Stewart [1983]. Progress in application to observations of the general circulation and mesoscale variability of the ocean has recently been reviewed by Fu [1983a]. To obtain absolute geostrophic velocity from altimetrically measured sea surface topography, adequate knowledge of the geoid (the earth's equipotential surface) is required. Because the geoid is not accurately known over most of the world ocean, altimetric observations have not yet improved our knowledge of the oceanic general circulation [see Tai and Wunsch, 1984]. However, the use of repeated altimetric observations whereby the unknown time-invariant geoid can be removed has provided a global view of the statistics of mesoscale variability of the oceans [e.g., Cheney *et al.*, 1983; Fu, 1983b]. Due to the presence of substantial, long-wavelength orbit errors in altimetric measurements, the scales of variability studied have been confined primarily to mesoscales (with a dominant length scale of about 100 km). Thus far, there have been no attempts to use satellite altimeter data to study large-scale (scales greater than mesoscales) temporal variability of the ocean.

In this paper we demonstrate a new method by which altimetric measurements can be used to construct sea level time series for the study of large-scale temporal variability of ocean currents. A number of techniques are employed to reduce long-wavelength orbit errors plus other errors without compromising low-frequency, large-scale oceanic signals. The essence of the technique is the separation of signal and error by utilizing fundamental differences in their spatial and temporal characteristics. The method is applied here to Seasat altimeter

data [see Tapley *et al.*, 1982a] to study temporal variability of the Antarctic Circumpolar Current (hereafter referred to as ACC) around the Southern Ocean. Some preliminary results of this study have been briefly reported in Fu and Chelton [1984]. A more complete and detailed description is given here.

Recent in situ observations in Drake Passage [e.g., Whitworth, 1983; Wearn and Baker, 1980] have revealed rather substantial temporal variations in the mass transport of the ACC. Due to a lack of synoptic observations around the Southern Ocean, very little is known about the spatial structure of this temporal variability. With its global coverage, altimeter data can be used to examine the spatial coherence of changes in the flow over spatial scales this large. Because of the short duration of the Seasat mission and errors in the altimeter data, the accuracy and statistical significance of the results presented here are not very high. Emphasis in this paper is placed more on demonstration of the methodology and its potential with more accurate and longer duration altimetric missions expected in the near future.

We begin with a discussion in section 2 of a new method for generating sea level time series from altimetric measurements. Data characteristics and error reduction techniques are described in sections 3 and 4, respectively. Testing of the method using Seasat altimeter measurements in the Drake Passage area and comparisons of the results with in situ measurements are discussed in section 5. Application to the entire ACC area is presented in section 6, and the results are discussed in terms of variations in geostrophic velocity. Finally, a summary and conclusion are given in section 7.

2. THE METHOD

The essence of the approach is to construct sea level time series from altimeter crossover differences, i.e., the difference between altimetric measurements made at the intersection (a crossover) of an ascending (northbound) and a descending (southbound) ground track. A crossover difference comprises three basic components: orbit error, altimeter measurement error, and true sea level variation. After reducing the two error components, altimeter crossover differences have previously

been used to map the statistics of mesoscale sea level variability [e.g., Cheney and Marsh, 1981; Gordon et al., 1983]. However, information contained in the crossover differences has not yet been exploited to examine the temporal history of sea level variations.

The method is most easily explained if we assume for the moment that the crossover differences are error-free. Effects of orbit error and measurement error will be discussed in later sections. Consider a small control area traversed by M ascending and N descending orbit tracks and assign to each track an unknown constant to represent an along-track average of sea level across the control area. We wish to make an estimate of the $M + N$ unknown average sea levels (one for each track) from the $M \times N$ crossover differences. The problem is thus an overdetermined one and can be solved by a least squares procedure. To pose the problem mathematically, denote the $M + N$ unknown along-track average sea levels by a_m ($m = 1, \dots, M$) and d_n ($n = 1, \dots, N$), where a_m and d_n are the sea levels for ascending and descending tracks, respectively. Define r_{mn} to be the altimeter-measured sea level difference at the crossover point corresponding to the m th ascending and n th descending track (ascending minus descending). The sum of square differences between sea level changes measured by the altimeter at the crossover points and changes in true sea level averaged across the control area is then

$$Z = \sum_{m=1}^M \sum_{n=1}^N (a_m - d_n - r_{mn})^2 \quad (1)$$

The average sea levels a_m and d_n can be determined by minimizing Z . The resulting equations for a_m and d_n can be obtained by differentiating with respect to a_m and d_n to get

$$Na_m - \sum_{j=1}^N d_j = \sum_{j=1}^N r_{mj} \quad (m = 1, \dots, M) \quad (2)$$

$$\sum_{i=1}^M a_i - Md_n = \sum_{i=1}^M r_{in} \quad (n = 1, \dots, N) \quad (3)$$

Since the sum of the M equations of (2) is equal to the sum of the N equations of (3), (2) and (3) represent only $(N + M - 1)$ independent equations. This simply means that an arbitrary constant exists in the solution. This constant can be fixed by setting

$$a_1 = 0 \quad (4)$$

Then the solution to (2), (3), and (4) is unique and represents the differences of a_m and d_n from a_1 , the unknown initial value of the sea level. By arranging a_m and d_n in order of increasing time, a time series of sea level in the control area is then obtained. Note that if sea level is truly constant across the control area but temporally varying between ground tracks, then $a_m - d_n = r_{mn}$ with error-free measurements.

It should be apparent that a good control area must meet two requirements. First, the number of crossovers in the area must be high to ensure adequate temporal resolution for the resulting time series. The number of crossovers increases with the size of the control area. However, the second requirement is that the dimension of the control area be small compared with the typical scale of oceanic variability so that average sea level over the area is a meaningful quantity. In application to real data, some compromise must be made between these two conflicting requirements.

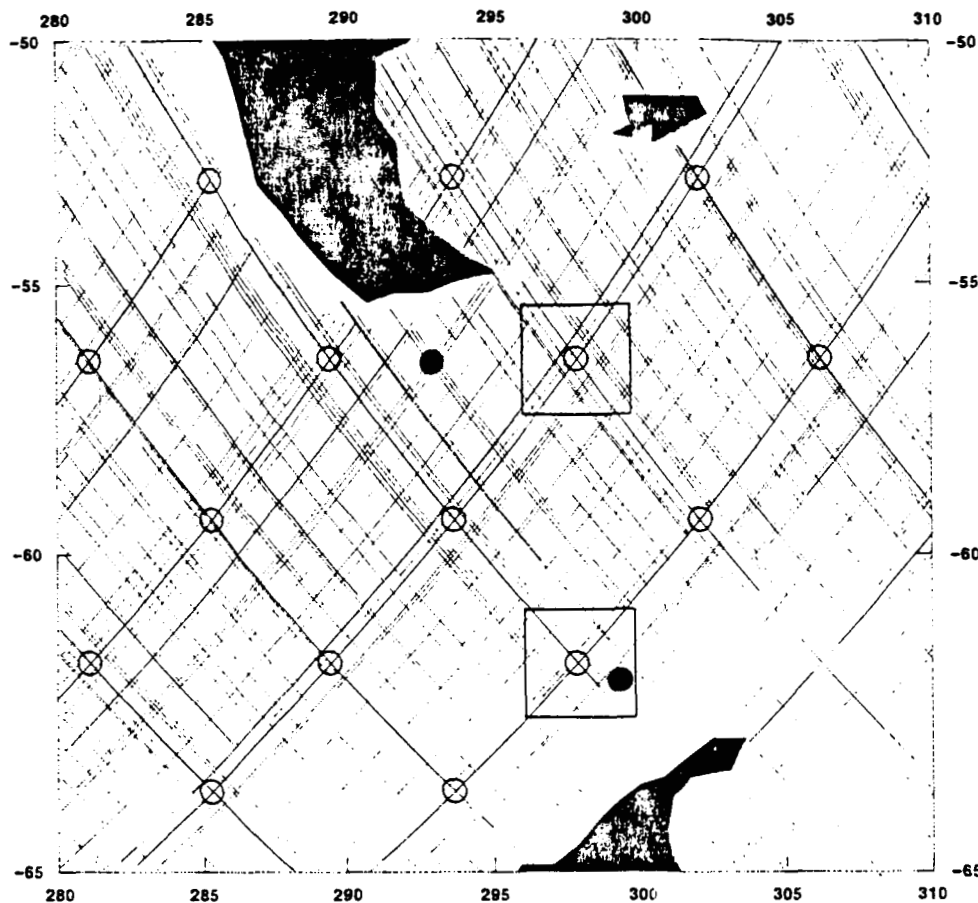
3. SEASAT ALTIMETER DATA AND CROSSOVERS

To examine the ACC around the entire Southern Ocean, all Seasat 1-s average altimeter data from the Geophysical Data

Records (GDR, see Lorell et al. [1980]) between 40°S and 65°S were used in this study. Most of the major errors had already been corrected in the GDR. These errors include tropospheric water vapor and ionospheric free electron range delays, tides, and the inverse barometer effect of atmospheric pressure loading (see Tapley et al. [1982a] for a detailed discussion). Before computing crossover differences, we applied three additional levels of processing to the data. First, a "glitch editing" procedure was performed to replace anomalous data values with their local medians across seven successive measurements. (The criterion for anomaly was a deviation of more than 2 m from the local median.) Second, a correction for sea-state bias was made by adding 7% of the altimeter-measured $H_{1/3}$ (significant wave height) to the sea surface height measurement [Born et al., 1982]. Third, all data flagged for anomalous scatter in the 1-s averages of returned radar power were eliminated. Such scatter occurs, for example, when there is ice or land in the footprint or side lobes of the altimeter antenna pattern.

To facilitate computation of crossover differences, the data set was divided into 12 overlapping subsets, each covering 25° of latitude and 40° of longitude. Within each subset, crossover points were located using the method described by M. E. Parke and L. R. Stavert (unpublished manuscript, 1985), and the corresponding crossover differences were then computed. To minimize the effects of short tracks and anomalous data on the orbit error reduction procedure to be discussed in section 4.1, two screening tests were applied to the computation: first, individual tracks with less than 10 crossovers were deleted before computing crossover differences; second, crossover differences exceeding 6 m were eliminated. A total of 125,222 crossover points were thus located, resulting in a rms crossover difference of 146 cm over the Southern Ocean. This value is significantly lower than the global value of 180 cm (M. Parke, personal communication, 1984), primarily due to the relatively low orbit error over the Southern Ocean (M. E. Parke and L. R. Stavert, unpublished manuscript, 1985).

Because Seasat was locked in a repeat orbit during the last month of the mission, the density of crossover points is highest at the intersections of the repeat tracks. These intersections are thus ideal locations for constructing sea level time series in a control area as discussed in section 2. Displayed in Figure 1 are the Seasat tracks in the vicinity of Drake Passage. The repeat-track intersections are indicated by open circles. After some experimentation with different sizes for the control area, we settled on a 200×200 km square around each repeat-track intersection. The exact location of the center of the control area was determined so as to maximize the number of crossovers in the square. We thus restrict attention to sea level variations with wavelengths longer than 400 km. Each control area thus determined contains a group of crossovers and is hereafter referred to as a cluster area. A total of 229 cluster areas which yielded good quality data were identified around the Southern Ocean. Two sample cluster areas are shown by the open squares in Figure 1. The two solid circles indicate the locations of bottom pressure gauges that were deployed in early 1976 as part of the International Southern Ocean Studies (ISOS) program to monitor the variability of the ACC through Drake Passage [see Wearn and Baker, 1980]. The two pressure gauges measured the bottom pressure at a depth of 500 m on the continental slope through 1980, thus bracketing the Seasat mission from July 7, 1978, to October 10, 1978. The altimeter-derived sea level time series in the two cluster areas will later be compared with the pressure gauge data. Before proceeding to the construction of time series in the cluster areas, we first discuss treatment of errors in the data.



ORIGINAL PAGE IS
OF POOR QUALITY

Fig. 1. Seasat altimeter data coverage in the Drake Passage area. Open circles represent intersections of 3-day repeat ground tracks. Solid circles denote the locations of ISOS bottom pressure gauges. Two sample cluster areas are shown by the open squares.

4. ERROR REDUCTION AND ANALYSIS

Successful application of the method described in section 2 to real data depends on the size of orbit error and measurement error in the crossover differences r_{mn} . Among the various errors, orbit error is by far the most significant. The global rms orbit error in the Seasat GDR has been estimated to be 150 cm [Tapley *et al.*, 1982a]. Since orbit errors are approximately uncorrelated from track to track, this corresponds to a rms crossover difference of 210 cm. These orbit errors would clearly obscure any oceanographic signals likely to be observed. Some method is thus required to reduce the size of orbit error. A method that has been successfully used in a number of past studies is discussed in detail below. This is then followed by a discussion of residual measurement errors and their reduction by a smoothing scheme.

4.1. Reduction of Orbit Error

Since its spatial scale is large (the dominant wavelength is the circumference of the earth; see Tapley *et al.* [1982a]), orbit error can be greatly reduced by a simple modeling effort: Over a distance of a few thousand kilometers (the meridional dimension of the Southern Ocean), the orbit error along track i can be expressed as [see Rapp, 1979]

$$e_i(t) = \alpha_i + \beta_i t + \gamma_i t^2 + \text{higher order terms} \quad (5)$$

where t is time, α_i , β_i , and γ_i are parameters whose values are determined for each track so as to minimize the resulting crossover differences in a least squares sense over a given geographic area. The least squares solution procedure used here is exactly the same as the one discussed in section 2

except that the control area is now very large (larger than the scales of true sea level variability). The estimated orbit error is then subtracted from each track of data. This is now a standard technique for reducing orbit errors in altimetric measurement.

For studies of mesoscale variability, the first two or three terms in (5) have been used to model the orbit error [Cheney and Marsh, 1981; Gordon *et al.*, 1983]. Since the focus of the present study is large-scale variability, only the first term, a constant, is used in (5). Inclusion of the linear and quadratic terms would remove any true sea level slope and curvature along track and hence eliminate large-scale geostrophic currents, which are the signals of interest in this study. It should be kept in mind, however, that the residual orbit error after removing only a constant bias (hereafter referred to as an orbit bias adjustment) from each track is higher than that resulting from also removing the higher-order terms in (5). It will be shown later that residual orbit error can be further reduced by temporally smoothing the crossover differences within a cluster area.

Applications of the orbit bias adjustment to the 12 subsets of data (see section 3) reduced the rms crossover difference from 146 to 32 cm averaged around the entire ACC. Shown in Figure 2 are histograms of the crossover differences before and after the orbit bias adjustment in one of the subset regions (40°S–65°S, 180°–220°). The rms crossover difference in this particular region is 146 cm before the adjustment and 34 cm after the adjustment. It is unlikely that the large residual crossover differences at the tails of the histogram (Figure 2, lower panel) were caused by large-scale sea level changes. Since these outliers would carry a large weight in determining

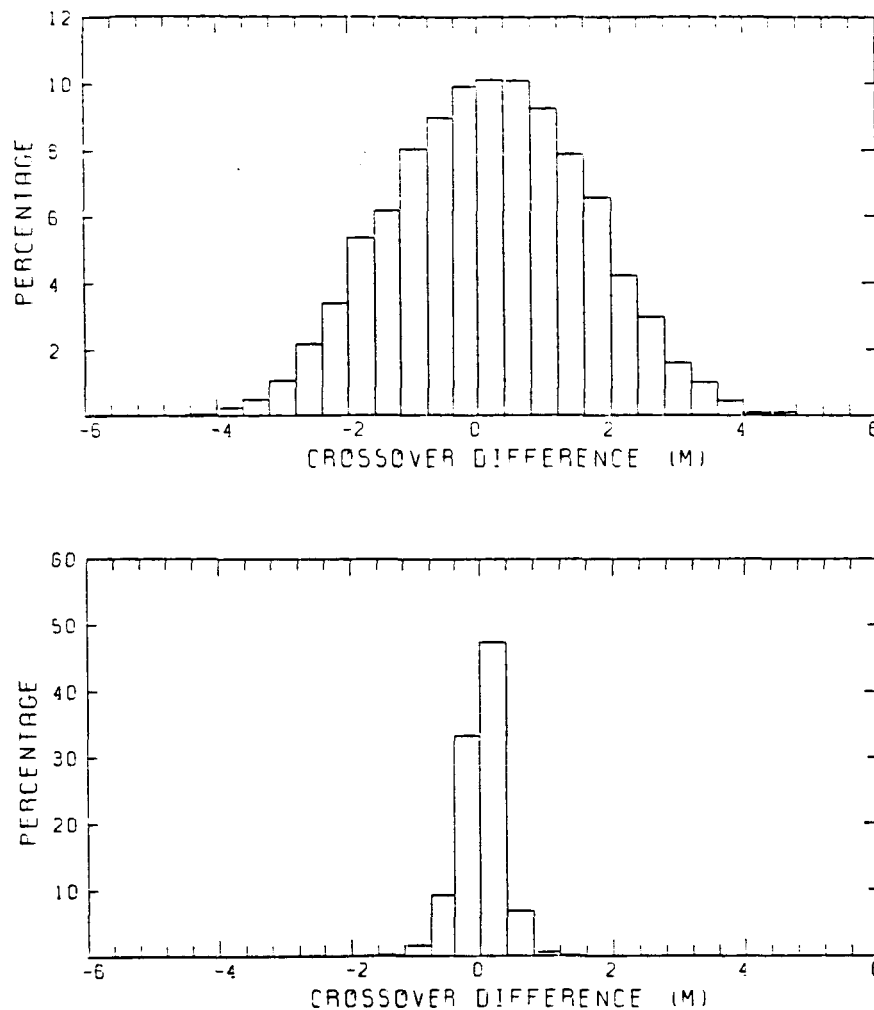


Fig. 2. Histograms of the crossover differences in the region 40°S–65°S, 180°–220° before (upper panel) and after (lower panel) an orbit bias adjustment.

sea level from least squares solutions, we deleted all the residual crossover differences exceeding 60 cm (about two standard deviations). This resulted in deletion of about 6% of the data, reducing the rms crossover difference to 24 cm around the entire ACC.

4.2. A Budget for the Residual Errors

To determine signal content of the residual crossover differences, we investigated the residual errors contained in the 24 cm rms variability. From the error budget for the Seasat altimeter data archived in the GDR [Tapley *et al.*, 1982a], the following major error sources for residual crossover differences were identified: residual orbit error, instrument noise, sea-state related bias, range delay by ionospheric free electrons and tropospheric water vapor, sea level variations caused by ocean tides and atmospheric loading (inverse barometer effects). The magnitude of each of these errors after applying the orbit bias adjustment of section 4.1 is discussed below.

1. By applying the orbit bias adjustment to a simulated orbit error data set, we estimate the residual rms orbit error to be 10 cm. A detailed discussion of the method used to obtain this estimate is given in Appendix A.

2. For 1-s average data in the GDR, the rms instrument noise is about 5 cm [Tapley *et al.*, 1982a]. Because this is

essentially a white noise (i.e., uncorrelated from point to point), it is not reduced by the orbit bias adjustment, which only affects errors with spatial scales on the order of 2500 km (the size of the orbit bias adjustment control area).

3. After the 7% $H_{1/3}$ correction for the sea-state bias, Born *et al.* [1982] estimated the rms residual sea-state bias error to be 2% of $H_{1/3}$. The average $H_{1/3}$ measured by the Seasat altimeter over the Southern Ocean is about 4 m [see Chelton *et al.*, 1981]. Therefore the rms sea-state bias error is estimated to be 8 cm. However, it should be kept in mind that the result of Born *et al.* [1982] was based on the average of a wide range of sea-state conditions at a number of geographical locations and might not be representative of the winter high sea-state conditions in the Southern Ocean during the Seasat period. Therefore 8 cm may be an underestimate, and the eliminated outliers of Figure 2 (lower panel) could in fact be due to sea-state bias errors. However, we will assume that the 8-cm estimate is approximately correct. The scale of the sea-state bias is 500–1000 km, which is too short to be significantly reduced by the orbit bias adjustment.

4. The ionospheric free electron range delay has been corrected in the GDR with an estimated rms residual error of 3 cm [Lorell *et al.*, 1982]. Because this error is distributed over a wide range of spatial scales, it is not clear how much it can be reduced by the orbit bias adjustment. We therefore conserva-

TABLE 1. Altimetry Error Budgets

Error Source	rms Magnitude, cm	
	Before Adjustment	After Adjustment
Instrument noise	5	5
Orbit	103	10
Sea-state bias	8	8
Ionosphere free electrons	3	3
Troposphere water vapor	4	4
Atmospheric pressure loading	3	3
Ocean tides	10	4
Root-sum-squares	104	16

tively estimate the residual error due to ionospheric effects to be 3 cm.

5. The tropospheric water vapor range delay has been corrected in the GDR using (when available) water vapor measurements from a scanning multichannel microwave radiometer (SMMR) on board Seasat. The rms error of this correction is estimated to be about 3 cm [Tapley et al., 1982b]. However, SMMR data are available for only about 80% of the altimeter measurements. The water vapor analyses from the Fleet Numerical Oceanography Center (FNOC) were used when SMMR data were missing. The correction using FNOC data has an estimated rms error of 6 cm [Tapley et al., 1982b]. Therefore the combined rms error for the water vapor effect is approximately 4 cm. Because the scale of this error is only 50–500 km, it is not significantly reduced by the orbit bias adjustment.

6. Sea level variations due to atmospheric pressure loading have been corrected in the GDR by using FNOC sea level pressure analyses. The rms error of this correction is estimated to be 3 cm [Tapley et al., 1982a]. Part of this error might have been removed by the orbit bias adjustment, since the scales of atmospheric pressure variations are of the order of several thousand kilometers. However, we have not attempted to estimate the reduction of error since the atmospheric mass field over the Southern Ocean is so poorly known. We therefore conservatively leave the residual error due to pressure effects at 3 cm after the orbit bias adjustment.

7. The global tide model of Schwiderski [1980] has been used to remove the tide-induced sea level changes from the GDR. The global rms error of this model is reputed to be of the order of 10 cm. Because the scales of the barotropic ocean tides are of the order of several thousand kilometers, part of the tidal error is removed by the orbit bias adjustment. As a rough estimate of the amount by which tidal error can be reduced, we used the difference between the model of Schwiderski and the model of Parke and Hendershott [1980] along Seasat tracks as a simulated tidal error data set. We then applied to this signal the bias adjustment discussed in section 4.1. This resulted in a reduction of the rms tidal error from 11 to 4 cm.

The error budgets before and after the orbit bias adjustment are tabulated in Table 1. The root-sum-squared total error after adjustment is about 16 cm. Since these errors are approximately uncorrelated from track to track, this corresponds to an rms error of 22 cm for crossover differences and accounts for 80% of the total variance of residual crossover differences. Assuming signal and noise are uncorrelated, the signal-to-noise ratio for the residual crossover difference is thus only 0.2. Clearly, further processing is required to reduce

errors to a level where temporally varying oceanic signals can be detected.

4.3. A Smoothing Scheme

The errors listed in Table 1 have time scales ranging from a few hours to a few days. This is generally much shorter than the time scales of large-scale oceanic variability (1 month or greater). It is therefore possible to temporally smooth those crossover differences that lie in a given cluster area to further reduce errors. In this section we present a smoothing technique which is analogous to a running average filter.

A particular crossover difference is a function of two times and can thus be expressed as $D_i(t_i, t_i')$, where t_i and t_i' are the times of ascending and descending tracks, respectively. When the two times of one crossover difference are close to those of another, the two crossover differences can be averaged to reduce random errors. In a given cluster area, we replaced the crossover difference D_i by a smoothed value \bar{D}_i defined by

$$\bar{D}_i = \frac{1}{N_i} \sum_{j=1}^{N_i} s_j D_j \quad (6)$$

The summation is over the N_i individual crossover differences D_j satisfying either of the following two conditions:

Condition A

$$|t_j - t_i| < T \quad |t_j' - t_i'| < T$$

Condition B

$$|t_j - t_i'| < T \quad |t_j' - t_i| < T$$

The coefficients s_j in (6) are either +1 or -1. The sign is determined as follows. The individual crossover differences were defined to be ascending minus descending altimeter measurements (see section 2). A temporal evolution of sea level is thus implicit in each crossover difference. The signs of the s_j in (6) are chosen to preserve the temporal sense of the crossover difference D_i . For example, if the ascending time of crossover i occurs after the descending time (i.e., $t_i > t_i'$), then all of the terms in the summation (6) must correspond to increasing time. For crossovers D_j for which $t_j > t_j'$, the sign of s_j is thus positive. However, for crossovers D_j for which $t_j < t_j'$, the sign of s_j is negative.

After experimenting with different values for T , we settled on a value of 10 days as a compromise between temporal resolution and error reduction. The smoothing scheme is then equivalent to averaging over a two-dimensional (20×20 day) running window as shown schematically in Figure 3, which displays the position in the t, t' plane of the crossovers in a sample cluster area ($59^\circ\text{S}, 100^\circ\text{W}$). For a given crossover denoted by the asterisk, the unbroken square represents the window corresponding to condition A, and the dashed square represents the window corresponding to condition B.

Shown in Figure 4 is a histogram of N_i for all of the crossovers that fall in the 229 cluster areas around the Southern Ocean (a total of 65,989 crossovers). The average number of individual crossovers used to obtain a smoothed value is 24. These crossover differences are not all independent. When the number of crossovers is large, N_i crossover points are (to a close approximation) the result of the intersections of $N_i^{1/2}$ ascending tracks and $N_i^{1/2}$ descending tracks. Thus the number of independent samples is approximately $2N_i^{1/2}$, or 9.8 on the average. One then expects that the smoothing scheme would reduce the rms error by a factor of $(9.8)^{1/2} = 3.1$, resulting in an rms error of 7 cm for the smoothed crossover

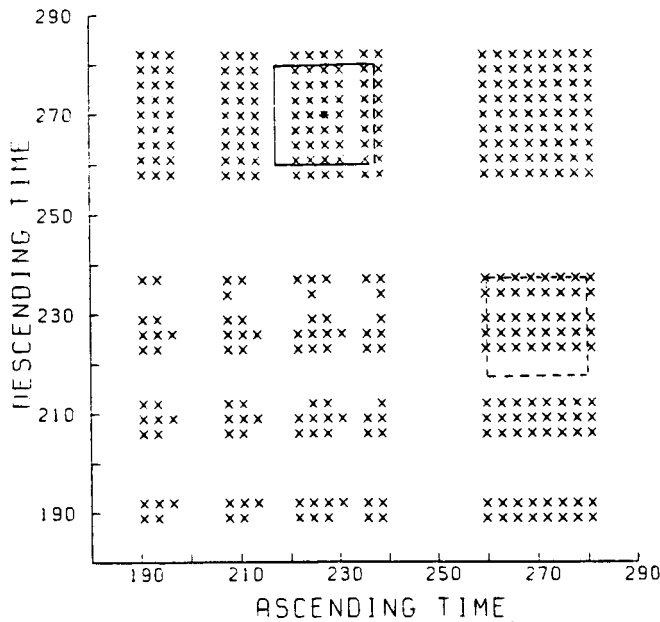


Fig. 3. Locations of crossovers in the plane spanned by their ascending and descending times (in day numbers of 1978) in a sample cluster area (59°S, 100°W). The two squares represent the two smoothing windows for the crossover denoted by the asterisk.

differences. This corresponds to an rms error of 5 cm for altimetric measurement of sea level. A more rigorous error estimate gives a value of 4.6 cm (see Appendix B).

Note from Figure 1 that within a cluster area a given ascending track does not always intersect all the descending tracks (and vice versa). In other words, the intersections of some of the ascending and descending tracks traversing the same cluster area fall outside its 200 × 200 km boundary. Therefore the number of crossovers along an individual track differs from track to track in a cluster area, making the sea level estimate for each track differently constrained in the least squares solutions given by (2) and (3). The estimated sea level would be more reliable for those tracks with the greatest number of crossovers. Computation of a smoothed crossover difference \bar{D}_i by (6), however, can be performed for any desired pair of ascending and descending times t and t' , regardless of whether such a crossover actually exists. From the set of ascending and descending ground track times in a cluster area,

we computed a smoothed crossover difference between all possible pairs of ascending and descending ground track times, even when the corresponding intersection fell outside the cluster boundary. Consequently, the number of smoothed crossover differences used as inputs to (2) and (3) is the same for all tracks, resulting in equal reliability for all sea level estimates in a cluster area. The total number of smoothed crossover differences in a cluster area is thus always somewhat greater than that of the actual raw crossover differences.

By applying this smoothing scheme to all 229 cluster areas, the rms residual crossover difference was reduced from 24 to 10 cm. Since the residual error has been estimated to be 7 cm, the signal-to-noise ratio is increased to about 1 (assuming signal and noise are uncorrelated). The effect of smoothing on the crossover differences is illustrated in Figure 5, which shows sample scatter plots of crossover difference versus time difference between ascending and descending tracks both before and after smoothing. The sample cluster area chosen is the one shown in Figure 1 by the square near the southern side of Drake Passage. Before smoothing, the crossover differences are dominated by errors and appear to be random with no systematic dependence on time difference. After smoothing, a general increase of crossover difference with time difference can be clearly seen, suggesting that a low-frequency signal has emerged from the noise. The smoothed residual crossover differences at the 229 cluster areas formed the data base for constructing sea level time series using the method described in section 2. Results at the two cluster areas shown in Figure 1, and their comparisons with the bottom pressure gauge data are discussed in the next section.

5. SEA LEVEL TIME SERIES

The ability to extract true sea level signal from noisy measurements using the methods described in sections 2 and 4.3 is investigated in this section using both altimeter and in situ data in the vicinity of Drake Passage. We first examine the performance of the methods by applying them to error-free known signals. As known signals, we have chosen the Wearn and Baker pressure gauge data on the north and south sides of Drake Passage as shown in Figure 1. After demonstrating the success of the methods on known signals, we apply the methods to actual Seasat altimeter data at cluster areas near the bottom pressure gauges and compare the results with the bottom pressure time series.

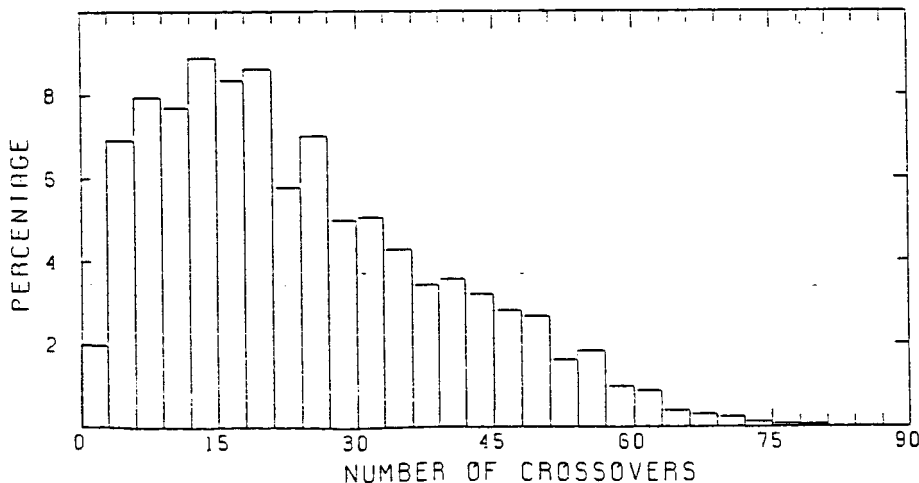


Fig. 4. Histogram of the number of crossovers averaged in each smoothed crossover difference computed over all the cluster areas.

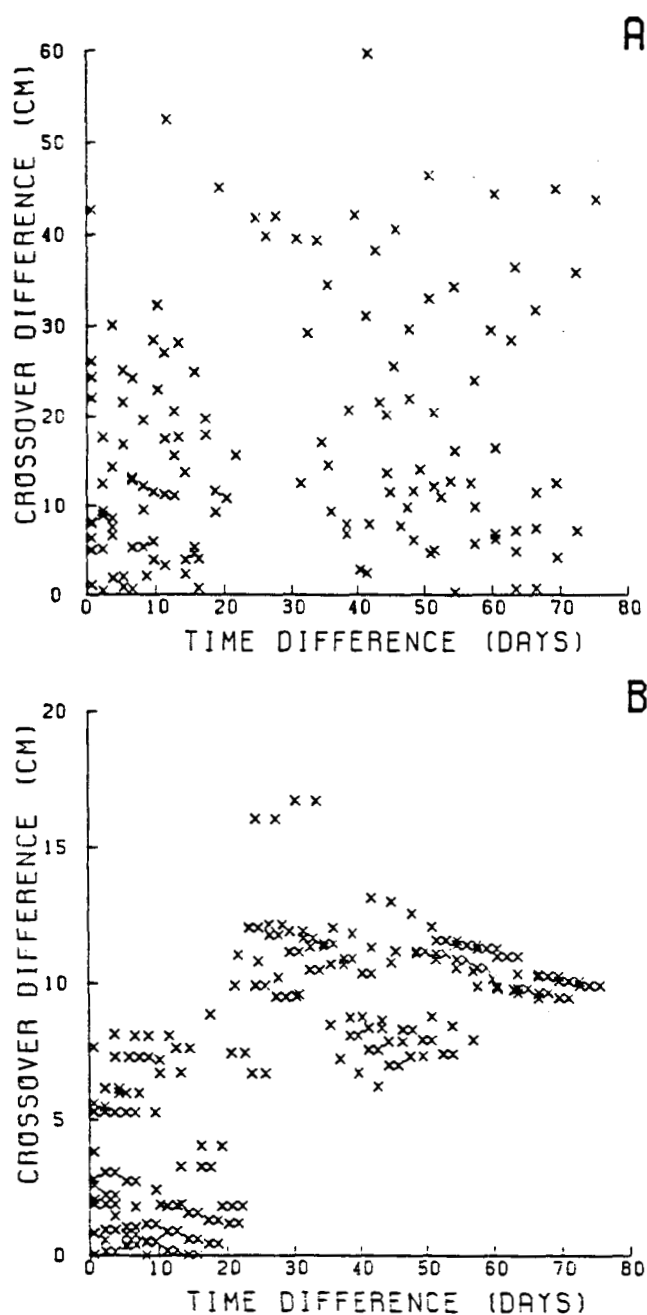


Fig. 5. Scatter plots of crossover difference versus the corresponding temporal separation before (upper panel) and after (lower panel) smoothing. Note the difference in vertical scale between the two panels.

5.1. Test Solutions

It is useful to demonstrate the reconstruction of a known time series from knowledge of its time-lagged differences (analogous to noise-free altimeter crossover differences). As two examples of known signals, we used the Wearn and Baker pressure data which are shown in Figure 6 by the thin lines (with the mean values removed). If the bottom pressure variations are indicative of barotropic ocean signals, 1 mbar change in bottom pressure is equivalent to approximately 1 cm change in sea level. It is not important here whether or not the bottom pressure data represent true sea level changes or whether the bottom pressure measurements are noisy. We simply wish to determine how well a specified signal (with

time scales similar to those likely to exist in the altimeter data) can be recovered using the crossover difference technique described in section 2 and the smoothing technique described in section 4.3.

A set of "crossover differences" was first generated by sampling the raw pressure data at the times when Seasat flew over the center of each track in the two cluster areas indicated in Figure 1. These crossover differences were then smoothed using the 20-day smoothing technique described in section 4.3 and used as inputs to (2) and (3). The resulting estimated bottom pressure time series are shown in Figure 6 by the open circles. The sampling intervals of the time series are irregular due to the irregular overpass times of the altimeter. The 20-day smoothed "altimeter sampled" data can be compared with the true 20-day running mean of the raw data (denoted by the heavy lines in Figure 6). For each test case, the single arbitrary constant in the solution was determined by minimizing the squares of the differences between the altimeter sampled data and the low-passed raw data. The results are quite satisfying. As expected, the reconstructed time series closely resemble the true 20-day running mean of the original time series.

5.2. Altimetrically Derived Sea Level Time Series

The same technique was applied to the actual altimeter measurements in the two cluster areas shown by the open squares in Figure 1. The estimated sea level time series obtained by applying (2) and (3) to the smoothed crossover differences are shown by the crosses in Figure 7. Comparisons with the low-passed bottom pressure data (solid lines) will be discussed in section 5.3.

The error bars in Figure 7 denote an rms error of ± 4.6 cm, which was obtained from a study in which the effects of the errors listed in Table 1 were simulated in the reconstruction of a given known time series (see Appendix B for details). Note that the expected error estimated from the more rigorous analysis in Appendix B differs little from the crude 5-cm estimate given in section 4.3.

The presence of a small-amplitude bimodal oscillation with approximately a 3-day period (e.g., the early part of the record at the northern cluster and the latter part of the record at the southern cluster) is caused by the effects of the smoothing scheme on altimeter measurement errors and can be explained as follows. Over a given cluster area, the altimeter data are characterized by an irregularly spaced series of ascending and descending orbit pairs separated in time by about 1/2 day. Successive pairs of passes are about 3 days apart except for the existence of data gaps. Thus the closely spaced points constituting the bimodal oscillation in Figure 7 alternate between ascending and descending orbits. For crossovers separated by less than a day, the true sea level difference should be small. However, the crossover differences are sometimes large because of altimeter measurement errors. The crossover differences associated with successive pairs of samples satisfy condition A in section 4.3 and are therefore averaged together to produce smoothed crossover differences from which the sea level estimates are computed. Thus the effect of an anomalous crossover difference spreads over the 20-day smoothing window. This can result in a finite and slowly varying offset between sea level estimates from ascending and descending orbits, which accounts for the bimodal oscillatory behavior found for some of the clusters. In section 6.2, gappy time series like those shown in Figure 7 are interpolated to a uniform time grid using an objective technique which eliminates the erroneous oscillatory behavior (see also Appendix C).

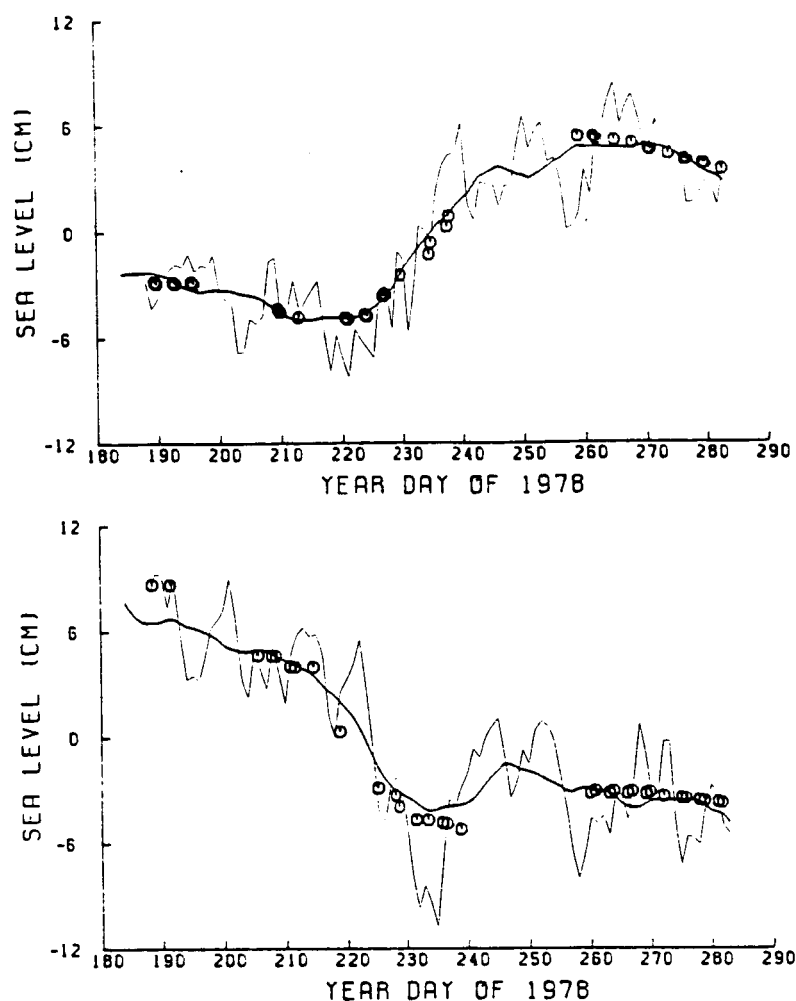


Fig. 6. Thin lines represent daily bottom pressure (in centimeters of its equivalent barotropic sea level change) at the southern (lower panel) and northern (upper panel) side of Drake Passage. Heavy lines represent a 20-day running average of the daily pressure record. Open circles show the reconstructed pressure record at altimeter overpass times using the method described in the text.

5.3. Comparison With Bottom Pressure Measurements

Ideally, we would like to compare the sea level time series derived from altimetry with in situ sea level measurements. Unfortunately, such measurements do not exist. To our knowledge, the only time series measurements which can be readily compared with the Seasat altimeter results in the Southern Ocean were made by the two aforementioned bottom pressure gauges deployed at a depth of 500 m on either side of Drake Passage (see Figure 1). As noted earlier, variation in bottom pressure is proportional to variation in sea level when the water movement is barotropic. However, in the presence of baroclinic motions, these two measurements can differ considerably. Sea level and bottom pressure can also differ by the simple fact that the bottom pressure gauges and altimeter cluster areas are not exactly collocated (see Figure 1). Nevertheless, we feel that a comparison between the two measurements can still shed some light on the validity of the altimetric results.

As shown in Figure 7, there is fair agreement between the sea level and low-passed bottom pressure time series in the southern region of Drake Passage (lower panel), whereas the two time series differ substantially in the northern region (upper panel). This geographic difference can be rationalized in terms of baroclinic variability. The currents in Drake Pas-

sage are concentrated along several baroclinic fronts [e.g., Nowlin and Clifford, 1982]. The cross-stream migration of these fronts can cause large baroclinic signals in sea level measured at a fixed location. In addition, the energetic eddy field in this region also has a significant baroclinic component. In general, the total flow variability (frontal migration plus eddies) in Drake Passage has been shown from in situ measurements to increase northward [Nowlin *et al.*, 1981], resulting in a larger discrepancy between sea level and bottom pressure in the northern region. In addition, the greater distance between the cluster area and the pressure gauge in the northern region could also account for part of the observed discrepancy.

The better agreement between observed sea level and bottom pressure in the southern region suggests that the flow variability there is predominantly barotropic and that the altimetric sea level time series is a valid measure of true sea level variations to the extent of estimated measurement errors.

6. TEMPORAL VARIABILITY OF THE ANTARCTIC CIRCUMPOLAR CURRENT

The crossover difference technique described in section 2 was applied to the smoothed crossover differences at each of the 229 cluster areas around the Southern Ocean to obtain

229 estimated sea level time series. The geographical distribution of the 229 cluster areas is shown in Figure 8 along with the average sea surface dynamic topography relative to 1000 dbar assembled from 50 years of snp data [Gordon *et al.*, 1982]. The large-scale variability of the ACC is well sampled by the altimetric cluster areas. The sea level variability at these 229 cluster areas over the 3-month Seasat mission is described in this section in terms of empirical orthogonal functions (EOF's). EOF's provide an efficient summary of the covariability over a large array of time series. Their use in data analysis is now a standard practice in oceanography (see Davis [1976] for a thorough discussion). A very brief summary of the formalism is given in section 6.1. The technique is applied to the 229 sea level time series in section 6.2, and the results are then discussed in section 6.3 in terms of geostrophic velocity.

6.1. Empirical Orthogonal Functions

Let $\eta_m(t)$ represent the altimetrically measured sea level at time t in cluster area m . We wish to express $\eta_m(t)$ at the cluster locations x_m , $m = 1, \dots, M$, in terms of M orthonormal functions $F_k(x_m)$ by

$$\eta_m(t) = \sum_{k=1}^M a_k(t)F_k(x_m) \quad m = 1, \dots, M \quad (7)$$

For this study, $M = 229$. EOF's are uniquely defined among the large number of possible orthonormal functions by the constraint that the corresponding amplitudes a_k satisfy

$$\{a_i(t)|a_j(t)\} = A_{ij}\delta_{ij} \quad (8)$$

where the braces are used to denote sample mean value averaged over t , A_{ij} is a constant, and δ_{ij} is the Kronecker delta. It can be shown that EOF's are the eigenvectors of the $M \times M$ mean cross product matrix C with elements

$$C_{ij} = \{\eta_i(t)\eta_j(t)\} \quad (9)$$

As a consequence of the orthonormality of the EOF's, the amplitude time series associated with the k th EOF is computed from the sample observations by

$$a_k(t) = \sum_{m=1}^M \eta_m(t)F_k(x_m) \quad (10)$$

The total mean square variability, summed over the M cluster points, is apportioned among the M modes such that the fraction of total mean square variability accounted for by mode k is

$$\{a_k^2(t)\} / \sum_{m=1}^M \{\eta_m^2(t)\}$$

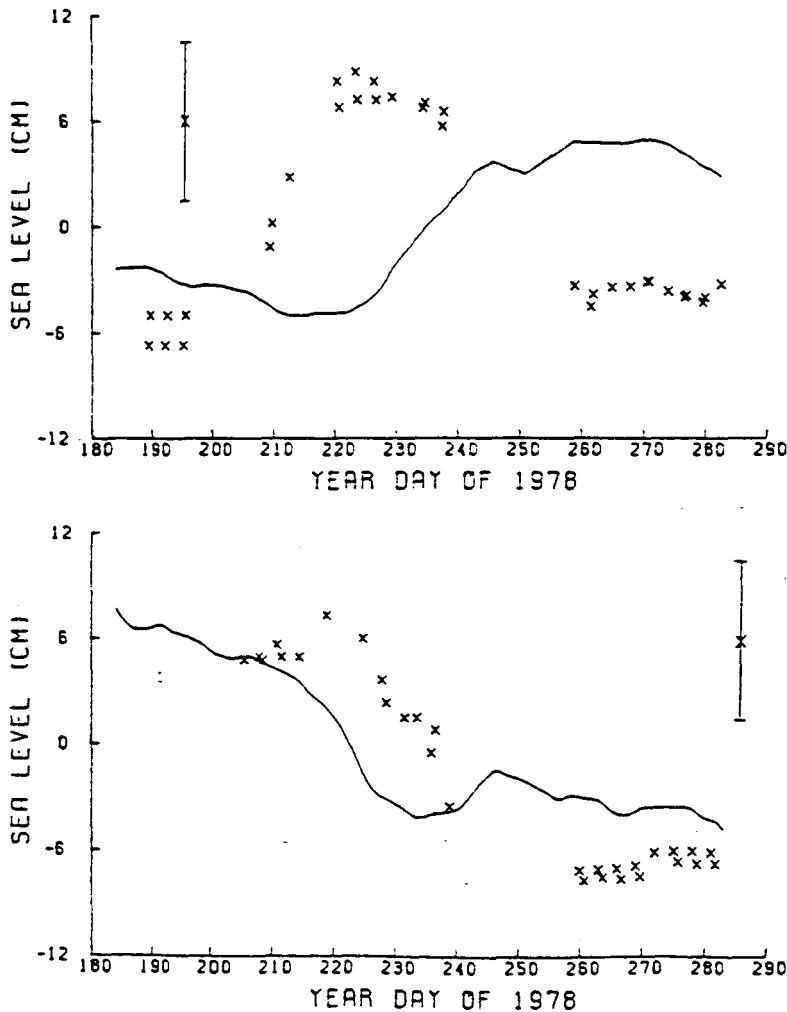


Fig. 7. Estimates (denoted by crosses) of sea level variation from Seasat altimetric crossover differences at the southern cluster area (lower panel) and northern cluster area (upper panel) in Drake Passage (see Figure 1 for locations). Solid lines represent the 20-day running average of the corresponding bottom pressure record.

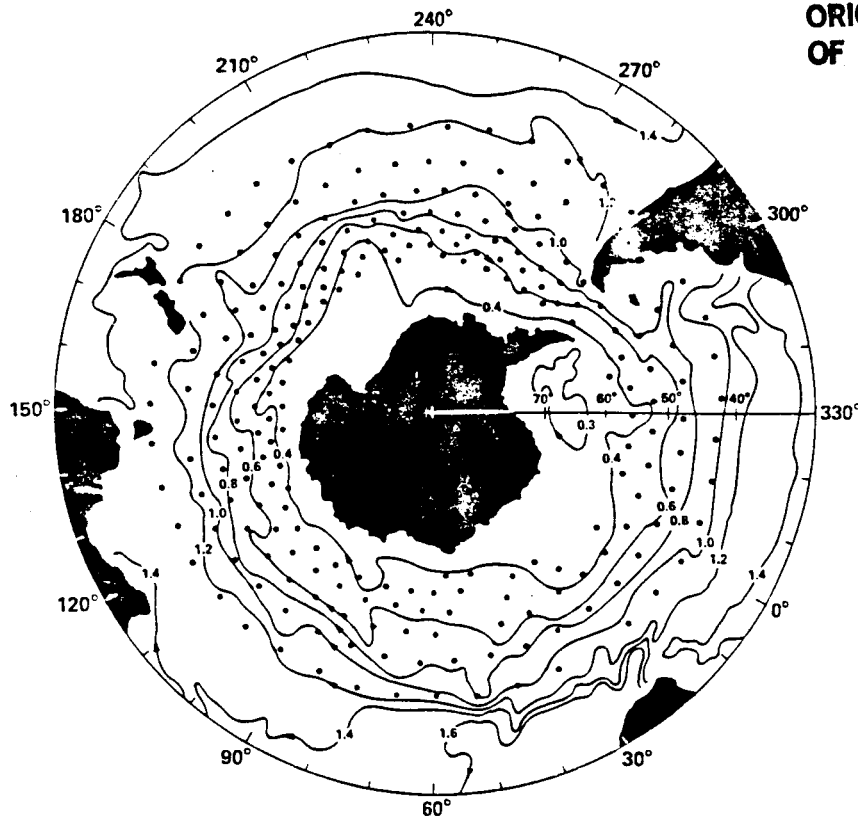


Fig. 8. Locations of the 229 Seasat altimeter crossover cluster areas in the Southern Ocean. Contours represent the long-term average dynamic height (in dynamic meters) relative to 1000 dbar [from Gordon *et al.*, 1982].

The virtue of EOF's over other possible orthonormal expansions is their efficiency of representation. Suppose the EOF's are ordered by decreasing $\{a_k^2(t)\}$. Then no other expansion of the ofrm

$$\eta_m^k(t) = \sum_{k=1}^K b_k(t) G_k(x_m)$$

in terms of $K < M$ functions $G_k(x_m)$ gives lower total mean square error

$$E = \sum_{m=1}^M \{[\eta_m(t) - \eta_m^k(t)]^2\}$$

than is obtained when the $G_k(x_m)$ are the EOF's [Davis, 1976]. Moreover, when the variability is dominated by large-scale coherent signals, only a small number of modes are required to represent most of the variability.

6.2. Sea Level Variability

To carry out an EOF analysis of the sea level time series, the objective analysis technique described by Bretherton *et al.* [1976] was used to interpolate the irregularly spaced $\eta_m(t)$ to a uniformly spaced time grid. With uniform sampling, the mean cross-product matrix C (see (9)) can easily be computed. Details of the objective interpolation are discussed in Appendix C. The interpolated time series were constructed at daily intervals beginning July 7, 1978 (day 188), the first day of Seasat altimeter data reception, and ending October 10, 1978 (day 283), the last day of Seasat operation. The sea level time series at each cluster point was constructed to yield changes in sea level relative to day 188. The EOF computation reveals that approximately 99% of the total mean square variability of the 229 time series can be represented by the first three EOF's

which account for 73.5%, 16.3%, and 8.7%, respectively, of the total mean square variability. Only the first EOF is discussed here; the spatial scales of the second and third EOF's are smaller and are considered to be dominated by errors.

The first EOF of sea level variability is contoured in Figure 9. Sea level rises and falls together in regions where the sign of the EOF is the same. The magnitude of the EOF value indicates the intensity of variability. Large spatial scales of the variability are clearly evident. The amplitude time series of the first EOF (Figure 10) is characterized by a secular increase over the 3-month observation period. It is apparent from Figure 9 that multiplication of the first EOF by its amplitude time series indicates a general decrease in sea level around the southern side of the Southern Ocean (negative areas near Antarctica) and a general increase in sea level to the north. The total sea level change in centimeters from the beginning to the end of the Seasat mission can be obtained by multiplying the EOF value by 7, the total change in the amplitude time series.

Since gradients of sea level reflect geostrophic surface velocities (see section 6.3), this pattern of sea level variation implies a general eastward acceleration of the ACC around Antarctica. This is represented in Figure 9 by the generally eastward arrows south of 50°S in the core of the ACC. EOF analysis thus suggests that the increase in ACC mass transport observed at Drake Passage [Wearn and Baker, 1980] is a local manifestation of a large-scale, eastward acceleration of the ACC. The eastward acceleration is notably disrupted in the three regions defined by longitude sectors 240°–270°, 330°–0°–20°, and 60°–80°. Flow variations over these regions are discussed in section 6.3 in terms of possible topographic influences.

North of the core of the ACC, the scales of variability are smaller, reflecting the possible influence of the subtropical

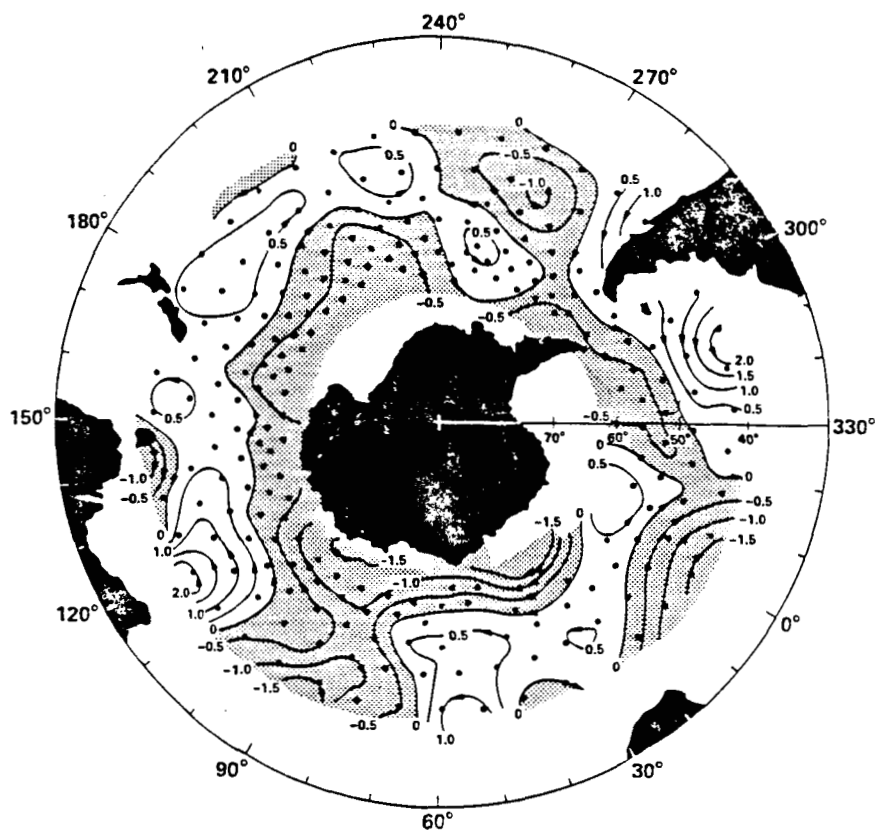


Fig. 9. The first EOF of sea level variability. Areas of negative values are stippled. Directions of the corresponding change in surface geostrophic velocity are indicated by the arrows.

convergence zones and the southern boundaries of subtropical gyres. As an example, the large localized sea level increase southeast of South America (300° – 330°) is probably caused by an intensification of the southeastward extension of the Brazil Current [see Reid *et al.*, 1977]. Similarly, the large localized sea level increase south of Australia (110° – 130°) probably reflects an intensification of the Leeuwin Current as it turns eastward around the southwest corner of Australia [Cresswell and Golding, 1980; Legeckis and Cresswell, 1981].

Since the nature of sea level variability is so simple (essentially a secular trend over the 96-day Seasat mission), the character of variability indicated by EOF analysis can be de-

termined by an alternative simple method. Differencing sea level from day 188 to day 283 at the 229 cluster points yields a pattern of total sea level change that is virtually identical to the spatial EOF shown in Figure 9 [see Fu and Chelton, 1984]. The advantage of the EOF analysis is that it provides an amplitude time series (Figure 10) from which the temporal evolution of large-scale sea level variability can be examined in greater detail.

Although the first EOF accounts for a large fraction (73.5%) of the total mean square variability, it is useful to examine the local representativeness of the EOF. The percentage of variability accounted for in each cluster area by the first

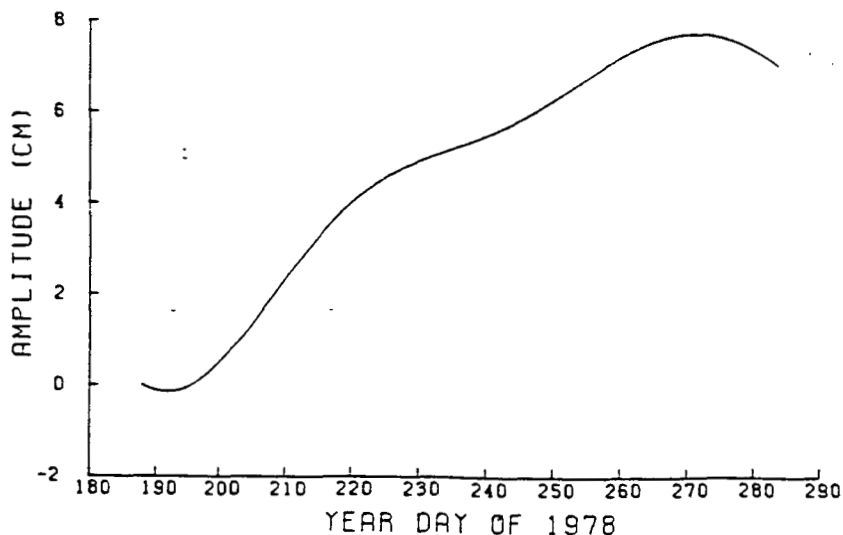


Fig. 10. Amplitude time series of the first EOF of sea level variability.

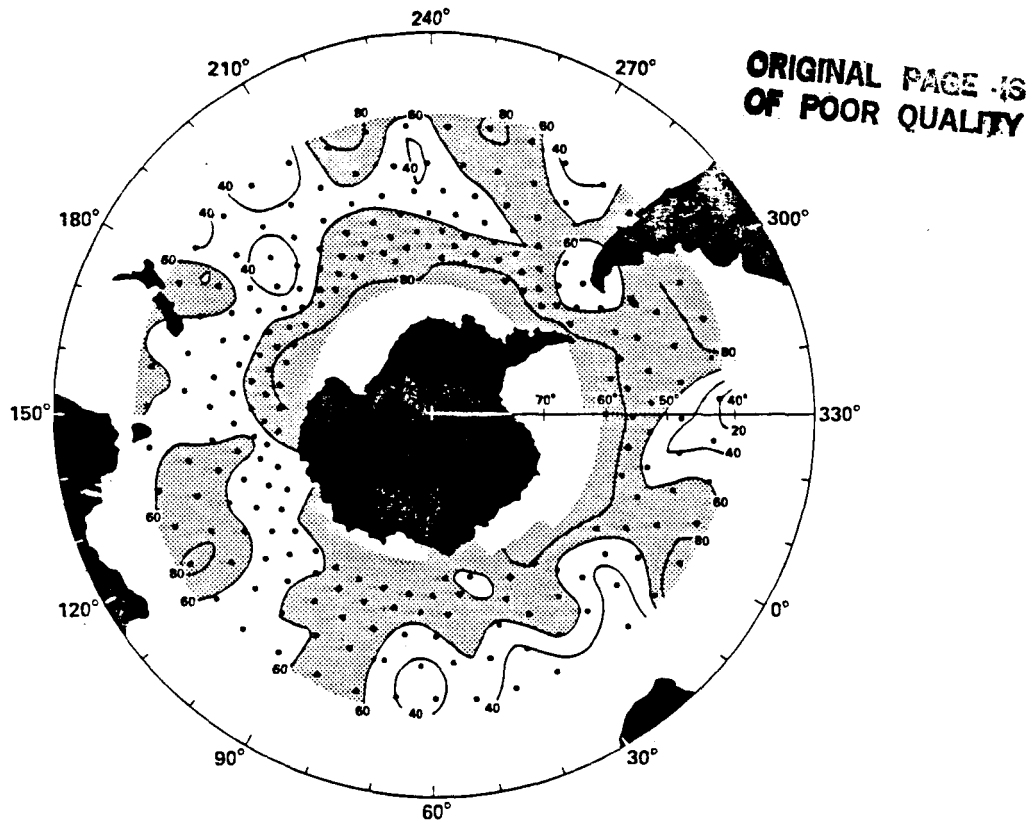


Fig. 11. Contour plot of the percentage of sea level variability accounted for at each cluster region by the first EOF.

EOF is contoured in Figure 11. Using the notation of section 6.1, the function plotted is

$$P(x_m) = \{a_1^2(t)\} F_1^2(x_m) / \{\eta_m^2(t)\}$$

which can be considered a measure of representativeness of the EOF; the EOF is most representative of the sea level variability in regions where the value of $P(x_m)$ is high. As the map clearly illustrates, the first EOF is a good representation of sea level variability in the core region of the ACC (south of 50°S), accounting for 60–80% of the signal in each cluster area.

6.3. Geostrophic Velocity Variability

Over periods longer than 20 days, sea level variations (after inverse barometric correction) essentially reflect variations in surface geostrophic currents [Wunsch, 1972]. Sea level measurements can thus be used to compute directly the variability of surface geostrophic velocity. Denote the net 96-day change in surface geostrophic velocity associated with the first EOF by δu (eastward) and δv (northward). Then

$$\delta u = -\frac{g}{f} \frac{\partial}{\partial y} (\delta H)$$

$$\delta v = \frac{g}{f} \frac{\partial}{\partial x} (\delta H)$$

where δH is the net 96-day change in sea level associated with the first EOF, g is the gravitational constant, f is the Coriolis parameter (negative in the Southern Hemisphere), and x and y are the east-west and north-south coordinates, respectively. To compute δu and δv , δH was first interpolated to a uniform $4^\circ \times 4^\circ$ grid using a two-dimensional cubic spline fit to the sea level changes associated with the first EOF at the 229 cluster points. Then δu and δv were evaluated at the grid point from

the resulting spline coefficients. Figure 12 shows the resulting net 96-day vector change in surface geostrophic velocity associated with the first EOF. The $4^\circ \times 4^\circ$ grid points are located at the tails of each vector. Superimposed on the figure are the 0°C and 5°C isotherms at 100-m depth (shown by dashed and solid lines, respectively) taken from Gordon *et al.* [1982, plate 11]. These subsurface isotherms represent approximate boundaries of the polar frontal zone which contains the high-speed core of the ACC (T. Whitworth, personal communication, 1984). Areas with depth less than 3000 m are stippled in Figure 12. The 3000-m contours were subjectively smoothed from Gordon *et al.* [1982, plate 2].

The generally eastward acceleration of the ACC discussed in section 6.2 is clearly evident in Figure 12. As noted earlier, there are three regions where the eastward acceleration is disrupted. These disruptions are apparently associated with topographic features. In the sector of longitudes 330° – 0° – 20° , the acceleration becomes southward at 340° , downstream from a region of rough topography comprising the meridionally oriented South Sandwich Island Chain and Trench to the east of Drake Passage. This southward acceleration is probably a manifestation of a lee wave generated by the topographic features. Between longitudes 350° and 20° , the net velocity change is westward, indicating a deceleration of the ACC over the 96-day Seasat mission. This deceleration may be related to the upstream southwind acceleration at 340° . The southward acceleration occurs near the region where the Weddell Sea gyre derives its inflow [e.g., Gordon and Huber, 1984], indicating a possible intensification of the gyre during the Seasat observation period.

Between longitudes 240° and 270° , a change from southward acceleration to northward acceleration is found along the 0°C isotherm, and a generally westward acceleration (deceleration of the ACC) occurs along the 5°C isotherm. These

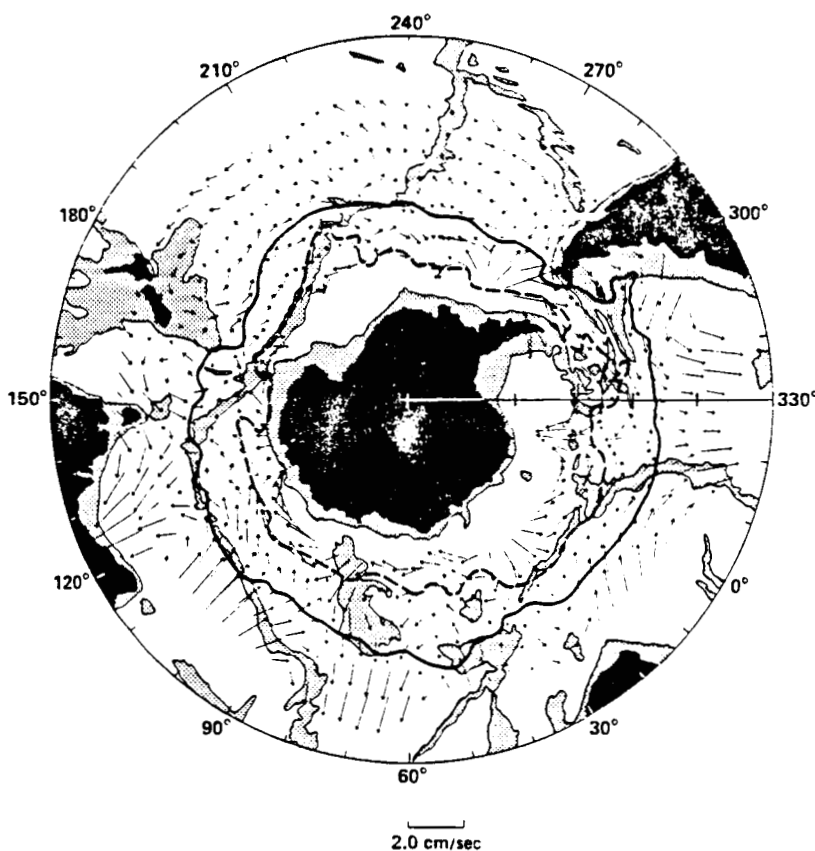


Fig. 12. Net vector change in surface geostrophic velocity associated with the first EOF of sea level variability. Also shown are the 0°C (dashed line) and 5°C (solid line) isotherms at 100-m depth [from Gordon *et al.*, 1982]. Areas shallower than 3000 m are stippled.

features also may be manifestations of a lee wave generated by the upstream Pacific-Antarctic Ridge.

The third disruption of the eastward acceleration of the core of the ACC is in the region between 60° and 80°. In this region there is a large area of northward acceleration apparently caused by the obstruction of the ACC by the Kerguelen Plateau.

Since the flow variability (Figure 9 and 12) has substantial meridional component in some regions, it is useful to determine whether the extent of the meridional migration of the ACC axis as suggested from the altimeter data is reasonable. From Figure 12, the magnitude of the altimetrically measured velocity change is generally less than 2 cm/s, much smaller than the 20–40 cm/s background surface velocity typically observed in this region [Whitworth *et al.*, 1982]. From the ratio of the velocity change to the mean background velocity and the zonal spatial scale of the variability, we can roughly estimate the meridional scale of cross-stream deflection due to the flow variability. A schematic diagram of initial (straight line) and final (curved line) paths of a streamline is shown in Figure 13. The cross-stream deflection scale (denoted by d) is thus related to the along-stream scale of the variability (denoted by L) by the following relation:

$$\frac{d}{L} \approx \frac{\delta v}{v}$$

where δv and v are the magnitudes of the velocity change and the mean background velocity, respectively. For example, consider a streamline roughly along the 5°C isotherm in the sector of longitudes 320°–0°–20°. The cross-stream component of the velocity difference changes from northward to southward over a distance of about 4700 km (60° in longitude at 45°S), so the corresponding L is about 2300 km. If we assume $v = 20$ cm/s and $\delta v = 2$ cm/s, then $d \approx 230$ km, which is comparable to the findings of Bowen and Stommel [1971] based on 1 year's repeated *Discovery II* sections along 0° and 20°E longitudes. We conclude that the meandering of the core of the ACC deduced from the altimeter data is not unreasonable.

7. SUMMARY AND CONCLUSION

A method has been developed to construct sea level time series from crossover differences of satellite altimetric measurements at geographical locations with high density of ascending and descending orbit ground track intersections (cluster areas). An orbit bias adjustment is first employed to reduce the dominant, long-wavelength orbit error by removing from altimetric measurements a constant bias over a distance of a few thousand kilometers. Residual crossover differences are then computed for each cluster location. To further reduce high-frequency residual errors, the sequence of crossover differences at each particular cluster location are smoothed using a two-dimensional running window in the two-time domain spanned by the ascending and descending

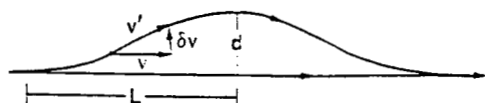


Fig. 13. Schematic diagram showing the relationship between the spatial scale of cross-stream deflection (d) and the magnitudes (v , v' , and δv) and along-stream spatial scale (L) of velocity variability.

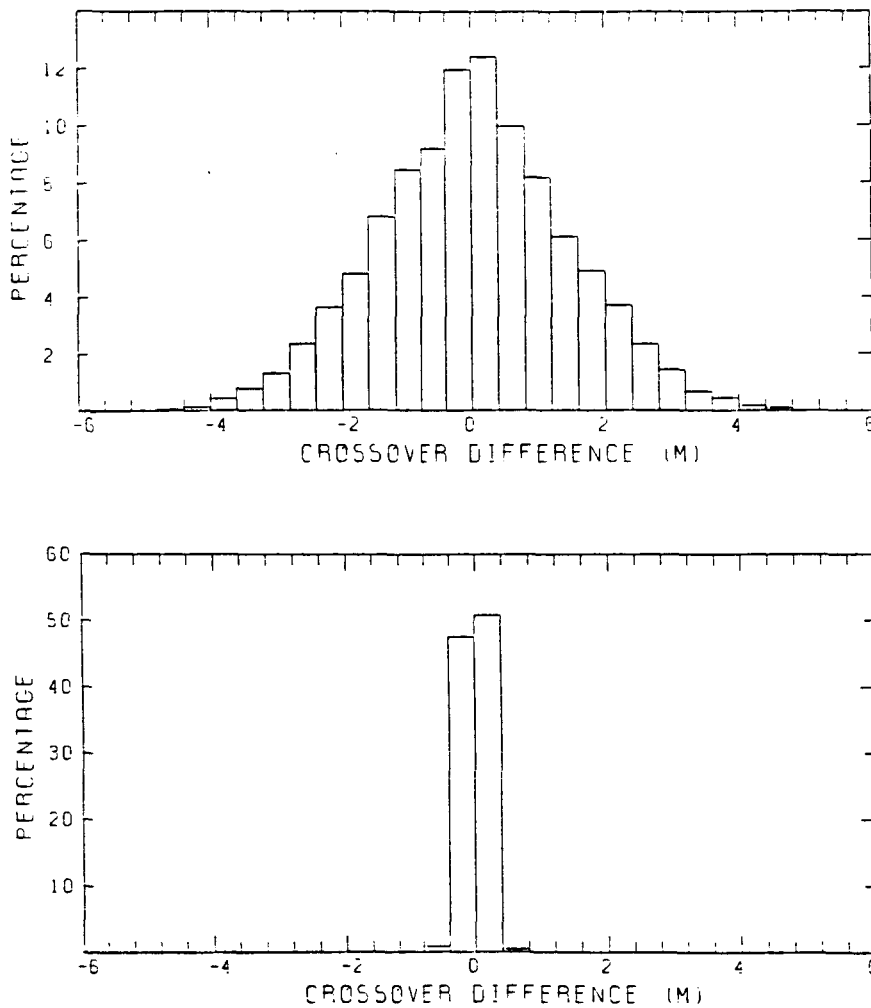


Fig. 14. Histograms of the crossover differences resulting from simulated orbit error before (upper panel) and after (lower panel) an orbit bias adjustment.

orbit times of the crossovers. The resulting crossover differences are then treated as measurements of time-lagged sea level differences, from which an irregularly spaced time series of sea level variation is estimated by a least squares technique. Finally, an evenly spaced sea level time series is constructed at each cluster location from the irregularly spaced samples using optimal interpolation.

The method is applied to Seasat data over the Southern Ocean to study large-scale temporal variability of the ACC during the Seasat mission (July 7, 1978, to October 10, 1978). Due to the fact that the Seasat orbits were nonrepeating (except for the last 30 days of the mission), clusters of crossover differences are sampled in a finite area of 200×200 km to assure adequate temporal coverage. In a given cluster area, the crossover differences are smoothed over a 20×20 day running window to reduce the magnitude of measurement errors to a marginally useful value of 5 cm (rms). Hence the resulting altimetrically measured sea level time series for each cluster location represents a spatial and temporal average of the true sea level variations.

The altimetric results were compared with in situ bottom pressure measurements made by pressure gauges deployed at a depth of 500 m on the continental slope on either side of Drake Passage. The comparison shows fair agreement between the two measurements at the southern side of Drake Passage, but substantial disagreement is found at the northern

side. We believe that this is due to a greater presence on the northern side of the ACC of baroclinic variability which causes the differences between sea level and bottom pressure measurements.

A total of 229 time series were computed from the Seasat altimeter data, covering the entire ACC region from 40°S to 65°S . An EOF analysis of the time series indicates that 73.5% of the total variability during the 96-day Seasat mission can be accounted for by the first EOF, which is characterized by a general decrease in sea level around the southern side of the ACC and a general increase in sea level to the north. The corresponding change in surface geostrophic velocity indicates a generally eastward acceleration of the ACC. Substantial meridional components of the acceleration are observed over major topographic features. The small magnitude of the large-scale meridional velocity change (about 2 cm/s over the 3-month mission) indicates that the extent of meridional migrations of the ACC axis during the Seasat mission are, at most, a few hundred kilometers.

The results presented here constitute the first direct observational evidence for large-scale coherence in the temporal variability of the ACC. Although the accuracy and statistical significance of the results are questionable due to the short duration and substantial measurement errors of the Seasat altimeter, the results have demonstrated the great potential of the methodology in application to more accurate and longer

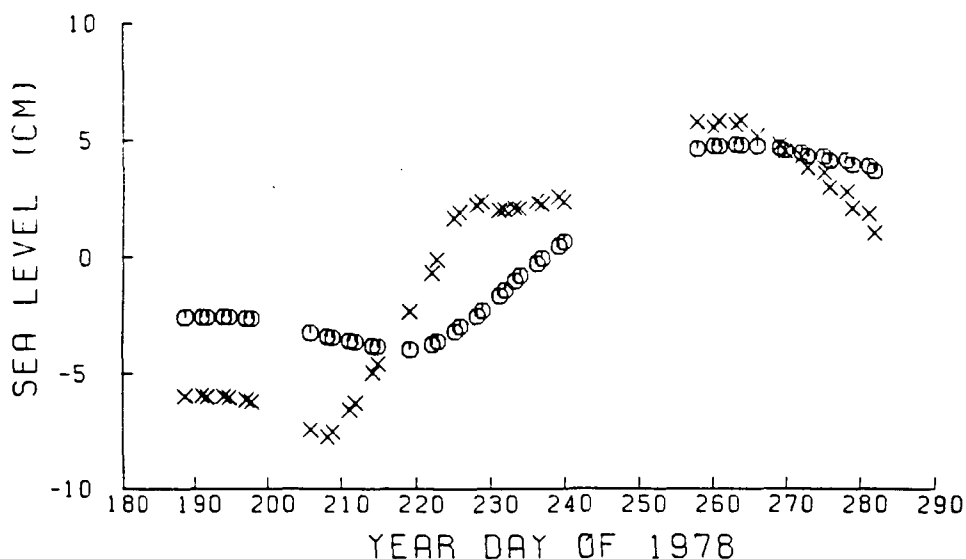


Fig. 15. An example showing reconstruction of the Wearn and Baker pressure record on the north side of Drake Passage using error-free (circles) and contaminated (crosses) crossover differences sampled at altimeter overpass times.

duration altimetric missions expected in the near future. For example, the projected rms accuracy for the altimeter proposed for the TOPEX mission [see *TOPEX Science Working Group*, 1981] is 14 cm, an order of magnitude improvement over Seasat. The TOPEX mission design calls for global altimeter measurements over a 3-year period. Using the method introduced here, we will be able to obtain from TOPEX altimetry a global network of sea level time series with much improved accuracy for studying temporal variability of the world ocean circulation.

8. APPENDIX A: REDUCTION OF ORBIT ERROR BY A BIAS ADJUSTMENT

As discussed in section 4.1, the rms crossover difference of the Seasat altimeter data between 40°S to 65°S is 146 cm before the application of an orbit bias adjustment. To a close approximation (within a few centimeters), the crossover difference is attributable to orbit error. In this appendix we investigate the extent to which an orbit error of the given magnitude

can be reduced by the bias adjustment discussed in section 4.1. The approach is to apply the bias adjustment to a simulated orbit error field.

Since the dominant frequency of orbit error is once per revolution [Tapley *et al.*, 1982a], the orbit error along a given track can be modeled as $A \sin(F_0 t + P)$, where A is an amplitude, F_0 is the once-per-revolution frequency ($1/101 \text{ min}^{-1}$ for Seasat), t is time, and P is a phase angle. Since orbit error is essentially random from track to track, A and P can be approximately modeled as random numbers with specified probability distribution functions (pdf). The pdf of P was simply assumed to be uniform between 0 and 2π . After experimenting with different pdf's for A , we found that a uniform pdf between 0 and a maximum value A_m resulted in a crossover difference histogram with shape resembling that shown in Figure 2. To make the simulated rms crossover difference close to the observed value of 146 cm, A_m was chosen to be 253 cm. We applied this orbit error model to the same sample region used in section 4.1. The histogram of the resulting crossover differ-

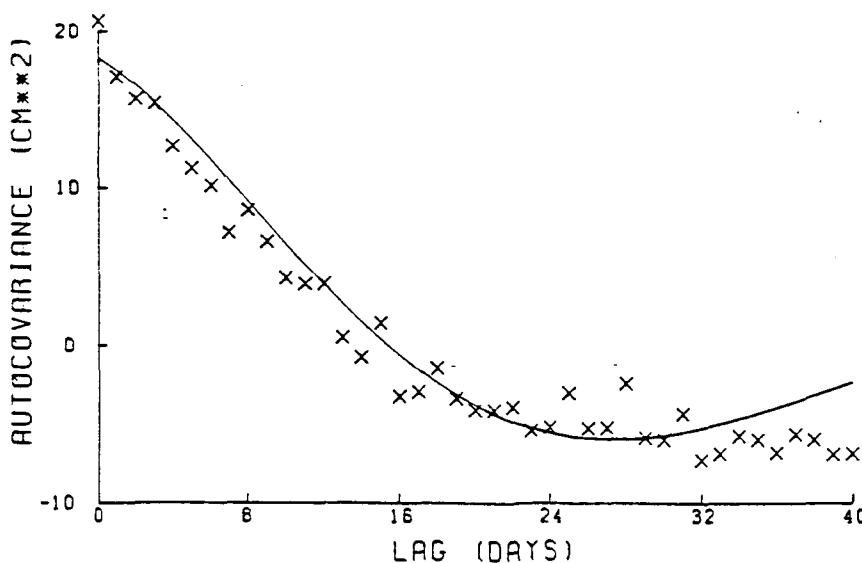


Fig. 16. Sample error autocovariance function estimated from simulations. The solid line represents a least squares fit by an analytical function (see text).

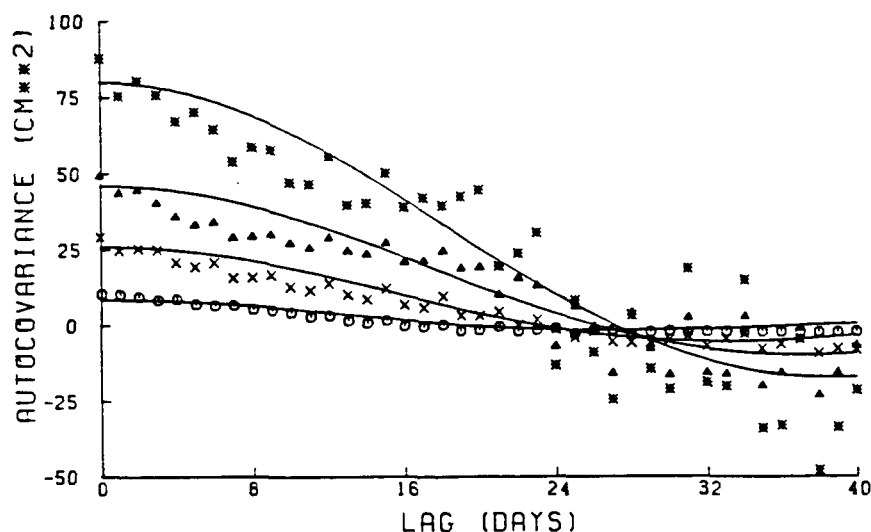


Fig. 17. Sample sea-level autocovariance functions estimated from altimetrically derived sea level time series with variance in the range 0–20 cm² (circles), 20–40 cm² (crosses), 40–60 cm² (triangles), and greater than 60 cm² (asterisks). Solid lines represent least squares fits by analytical functions (see text).

ences is shown in Figure 14 (upper panel). The standard deviation is 145 cm, the skewness is 0.02, and the kurtosis is 0.99. For comparison, the corresponding parameters for the real data in Figure 2 (upper panel) are 146 cm, -0.02 , and 0.89, respectively.

After application of the orbit bias adjustment (as discussed in section 4.1) to the simulated orbit error, the rms crossover difference was reduced from 145 to 14.2 cm. A histogram of the residual crossover differences is shown in the lower panel of Figure 14. Since the orbit biases of the two tracks in the crossover difference are essentially uncorrelated, an estimate of the residual orbit error is thus 14.2 cm divided by $2^{1/2}$, or 10 cm.

9. APPENDIX B: ERROR ESTIMATE FOR THE ALTIMETRICALLY DERIVED SEA LEVEL TIME SERIES

In section 4.3, the rms error of the smoothed crossover differences was crudely estimated to be 7 cm. This estimate, when divided by $2^{1/2}$ (i.e., 5 cm), can be considered a rough estimate for the rms error of the altimetrically derived sea level time series obtained through (2) and (3). In this appendix a more rigorous error estimate is made from a simulation study in which the various errors listed in Table 1 are included in the generation of simulated time series. In addition to an rms error estimate, an estimate of the error autocovariance function is also obtained. This error autocovariance is required for obtaining interpolated sea level time series by optimal estimation scheme (see Appendix C).

The residual errors after the orbit bias adjustment of section 4.1 (see Table 1) can be grouped into three categories: (1) point-to-point random; this category includes only instrument noise and has an rms value of 5 cm. (2) Track-to-track random; this category includes residual orbit error, sea-state bias, ionosphere and tropospheric range delay, and atmospheric pressure loading. Although not all of these errors are strictly random from track to track, their decorrelation time scales are believed to be shorter than a week. The root-sum-squares error from these sources is 14.1 cm. (3) Track-to-track systematic; this category includes only the tidal error, which is estimated to be 4 cm after orbit bias adjustment (see section 4.2).

The method used to estimate the statistical characteristics of

the errors can be summarized as follows. First, an error-free time series was obtained for a given cluster area by solving (2) and (3) using smoothed crossover differences sampled at altimeter overpass times from the Wearn and Baker bottom pressure record on the north side of Drake Passage. The procedure is exactly the same as that used to generate the simulated time series in Figure 6. Then a "contaminated" time series was generated by adding simulated errors. The northern Wearn and Baker pressure record was first resampled with added errors from all the three categories defined above. To simulate type 1 errors, a random number with a Gaussian pdf with a standard deviation of 5 cm was added to each sampled value. To simulate type 2 errors, a random number with a Gaussian pdf with a standard deviation of 14.1 cm was added to each sampled value (sampled at the center of each track). Finally, to simulate type 3 errors (tidal error), a sinusoidal signal with an amplitude of 5.7 cm (corresponding to an rms signal of 4 cm), a frequency of $1/12.42 \text{ h}^{-1}$ (the M_2 tidal frequency), and an arbitrary (but fixed for all sample times) phase was added to each sampled value. With these errors added, crossover differences were computed as before. After smoothing using the method described in section 4.3, these contaminated crossover differences were then used to generate a contaminated time series for the cluster area using (2) and (3). The difference between the two time series is thus a simulated error time series. An example showing error free and contaminated time series are displayed in Figure 15.

Such simulations were performed at 110 clusters to obtain an ensemble of simulated error time series from which a sample error autocovariance function was obtained (Figure 16). The autocovariance function was computed at lags with daily intervals. Because the error time series were irregularly spaced, the autocovariance was computed through a binning process. The value at each daily lag was an average within a 1-day bin centered at the lag. As shown in Figure 16 the zero-lag autocovariance (i.e., the error variance) was 20.7 cm² and the first zero-crossing of the autocovariance function was at about 16 days. Thus the rms error for the altimetric time series is 4.6 cm, in close agreement with the rough estimate of 5 cm in section 4.3. This corresponds to an rms error of 6.5 cm in crossover differences. The finite lag zero crossing is primarily a result of the smoothing of a random noise.

TABLE C1. Parameters for $R(\tau)$

Category	Variance Range. cm^2	Number of Clusters	Q . cm^2	P . d^{-1}
I	0-20	99	9	0.166
II	20-40	63	26	0.137
III	40-60	39	46	0.121
IV	60-	28	80	0.116

To be useful for the optimal interpolation discussed in Appendix C, the error autocovariance function was modeled by the four-parameter, positive definite (see Appendix C for definition) analytical function

$$E(\tau) = D\delta(\tau) + A \exp(-B\tau) \cos(C\tau) \quad (\text{B1})$$

where τ is the lag and $\delta(\tau)$ represents a special function for the contribution from random errors and is defined to be unity at $\tau = 0$ and zero elsewhere. The parameters A , B , and C were obtained by fitting the exponential-damped cosine function, represented by the second term of (B1), to the sample error autocovariance function through a nonlinear least squares procedure. Then D was obtained as the difference between the variance and A . The resulting estimates of the parameters were $D = 2.4 \text{ cm}^2$, $A = 18.3 \text{ cm}^2$, $B = 0.0389 \text{ d}^{-1}$, $C = 0.102 \text{ d}^{-1}$. $E(\tau)$ is shown by the solid line in Figure 16.

10. APPENDIX C: OPTIMAL INTERPOLATION OF AN IRREGULARLY SPACED TIME SERIES

There are many methods which can be used to interpolate an irregularly spaced time series to a regular time grid. All methods should produce similar results; if the interpolation method makes a great deal of difference in the final time series, then the process under investigation is probably undersampled temporally. The method we adopt is an objective scheme based on optimal estimation theory. It is preferable over other techniques because it provides a measure of the accuracy of each interpolated estimate based on statistical information about the signal and measurement error.

Optimal estimation was first used by meteorologists to generate synoptic maps of atmospheric variability [see Gandin, 1965; Alaka and Elvander, 1972]. The method has been applied to oceanographic data by Bretherton *et al.* [1976], who have also thoroughly reviewed the subject. Only a brief account of the method is given here with specific emphasis on application to the altimetric sea level time series.

Consider a set of N imperfect measurements of sea level at cluster area m . Use $h_m(t_i)$ to denote the true sea level and $\eta_m(t_i)$ the corresponding imperfect measurement at time t_i , $i = 1, N$. Then

$$\eta_m(t_i) = h_m(t_i) + \varepsilon_m(t_i) \quad (\text{C1})$$

where $\varepsilon_m(t_i)$ is the measurement error. For simplicity in the notation that follows, we will drop the subscript m with the understanding that an interpolated time series must be generated for each of the 229 cluster points. An estimate of sea level at time t can be constructed from all N imperfect measurements by

$$\bar{h}(t) = \sum_{i=1}^N \alpha_i \eta(t_i) \quad (\text{C2})$$

Note that the estimate $\bar{h}(t)$ is biased unless both the true value $h(t)$ and the measurements $\eta(t_i)$ have zero mean value. This is easily seen by noting that the bias of the estimate is

$$\langle \bar{h}(t) - h(t) \rangle = \sum_{i=1}^N \alpha_i \langle \eta(t_i) \rangle - \langle h(t) \rangle$$

Here angle brackets are used to denote the true expected value over a hypothetical infinite ensemble of realizations. The true ensemble averages $\langle h(t) \rangle$ and $\langle \eta(t_i) \rangle$ are not, in general, known. To minimize this bias, the sample mean of the measurements $\eta(t_i)$ was removed prior to constructing the optimal estimate by (C2). This sample mean was then added back to the estimate $\bar{h}(t)$ to obtain the final interpolated time series.

In general, the estimate (C2) should be constructed from only those measurements within a specified time window about the estimation time t in order to limit the size of the matrix to be inverted in forming the optimal estimate (see below). For the application here, the number of irregularly spaced measurements was small enough that all of the measurements at a particular cluster point were used to construct the estimates.

The expected square error of the estimate (C2) is

$$\langle [h(t) - \bar{h}(t)]^2 \rangle = \langle h^2(t) \rangle - 2 \sum_{i=1}^N \alpha_i A_i + \sum_{i=1}^N \sum_{j=1}^N \alpha_i D_{ij} \alpha_j \quad (\text{C3})$$

where A_i and D_{ij} , defined by

$$A_i = \langle h(t) \eta(t_i) \rangle \quad (\text{C4})$$

$$D_{ij} = \langle \eta(t_i) \eta(t_j) \rangle$$

are the elements of an $N \times 1$ vector (denoted by A), and an $N \times N$ matrix (denoted by D), respectively. The optimal estimate $\bar{h}(t)$ is obtained when the expected square error is minimized with respect to the parameters α_i . This minimum is obtained by setting the derivative of (C3) with respect to α_i equal to zero which gives the N equations (one for each i)

$$A_i = \sum_{j=1}^N \alpha_j D_{ij} \quad (\text{C5})$$

Solving these equations for the N parameters α_i gives

$$\alpha_i = \sum_{j=1}^N D_{ij}^{-1} A_j \quad (\text{C6})$$

where D_{ij}^{-1} is the i, j th element of the inverse of matrix D . Note that (C5) simplifies the expression (C3) for the expected square error of the estimate $\bar{h}(t)$ to

$$\langle [h(t) - \bar{h}(t)]^2 \rangle = \langle h^2(t) \rangle - \sum_{i=1}^N \alpha_i A_i \quad (\text{C7})$$

It is apparent from (C2), (C6), and (C7) that the sea level estimate $\bar{h}(t)$ and its expected square error require knowledge of the vector A and matrix D . If we assume that the measurement errors $\varepsilon(t_i)$ are uncorrelated with the signal $h(t)$ and that the statistics are stationary, then

$$A_i = R(t - t_i) \quad (\text{C8})$$

$$D_{ij} = R(t_i - t_j) + E(t_i - t_j)$$

where $R(\tau)$ and $E(\tau)$ are the signal and error autocovariance functions defined by

$$R(\tau) = \langle h(t)h(t + \tau) \rangle \quad (\text{C9})$$

$$E(\tau) = \langle \varepsilon(t)\varepsilon(t + \tau) \rangle$$

The true expected values within angle brackets in (C9) must be estimated from sample statistics. Since the sample measurements are irregularly spaced, it is necessary to approximate $R(\tau)$ and $E(\tau)$ by continuous analytical functions in order to compute A_i for general sample time t and interpolation time t_i . These analytical representations must satisfy the very im-

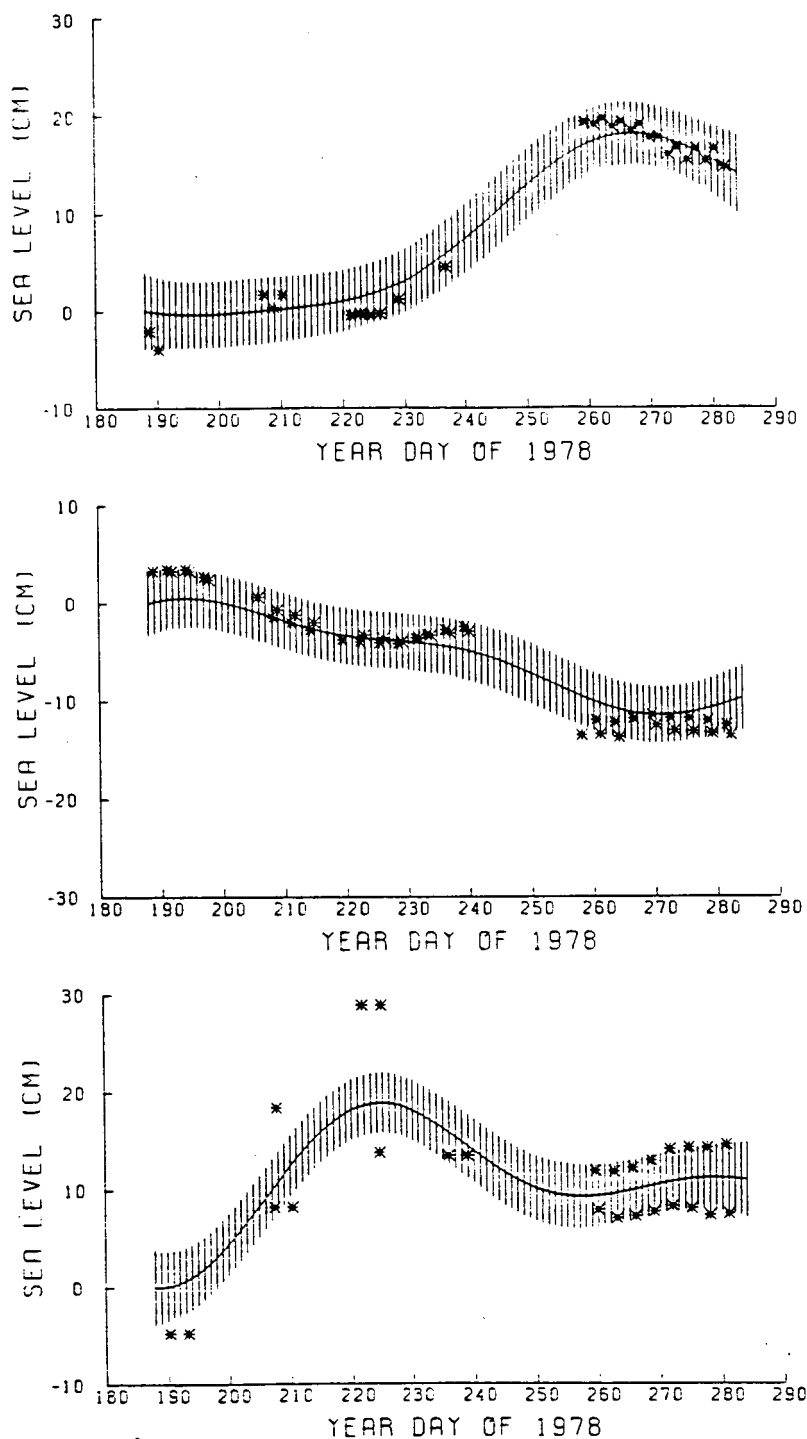


Fig. 18. Interpolated sea level time series at three sample cluster areas. The vertical bars represent error estimates obtained from the optimal interpolation technique (the square root of (C7)).

portant constraint that they be positive definite functions (i.e., the corresponding autocovariance matrix be positive definite for any arbitrary set of sampling lags) in order to assure that the mean square estimate

$$\begin{aligned} \langle \bar{h}^2(t) \rangle &= \sum_{i=1}^N \sum_{j=1}^N \alpha_i D_{ij} \alpha_j \\ &= \sum_{i=1}^N \sum_{j=1}^N \alpha_i R(t_i - t_j) \alpha_j + \sum_{i=1}^N \sum_{j=1}^N \alpha_i E(t_i - t_j) \alpha_j \end{aligned}$$

is nonnegative. Failure to satisfy this constraint can lead to very bad estimates by (C2). A function of lag τ is assured of

being positive definite if its Fourier transform is everywhere positive. This corresponds to positive spectral density at all frequencies. We used this criterion for positive definiteness in selecting proper functional representations for $R(\tau)$ and $E(\tau)$.

The functional form for $E(\tau)$ has already been given in Appendix B. The analytical form for $R(\tau)$ was determined as follows. We used the 229 altimetric sea level time series to estimate $R(\tau)$. First, a sample autocovariance function was computed at daily lags for each irregularly spaced time series using the same binning procedure as that used for estimating $E(\tau)$. Because the statistics of the sea level time series were not spatially homogeneous, we divided the 229 time series into

four categories according to their mean square variability (i.e., the variance) and computed an average autocovariance function for each category. The results are shown by different symbols in Figure 17. The definition of the four categories and the number of their corresponding samples are given in Table C1. Note from Figure 17, that the sample autocovariances for categories I and II are much less noisy than those of categories III and IV due to the fact that the statistics were compiled over a larger number of clusters. Each sample autocovariance function was fitted (through a nonlinear least squares procedure) by a positive-definite analytical function of the form

$$R(\tau) = Q \sin(P\tau)/(P\tau) \quad (C10)$$

The coefficients P and Q for each category are also given in Table C1. The resulting $R(\tau)$ are shown by continuous lines in Figure 17.

Using $R(\tau)$ and $E(\tau)$ represented by (C10) and (B1), respectively, optimal estimates of sea level along with corresponding error estimates were constructed for the 229 time series using (C2), (C6), and (C7) at daily intervals from July 7, 1978 (day 188), to October 10, 1978 (day 283). Each interpolated series was computed relative to a sea level value of zero at day 188. Three examples are shown in Figure 18. The upper two panels represent typical cases, while the bottom panel shows an extreme case in which the measurement errors are exceptionally large. The interpolation performs fairly well even for the extreme case. At sample observation times, the estimated value is exactly equal to the measured value when the measurement error ϵ is zero. However, for nonzero measurement error, this is not true in general. The deviation of interpolated values from sample observations is thus due to the effect of finite measurement errors. For the typical cases (upper two panels in Figure 18), the deviation is consistent with the estimated error bars.

Acknowledgments. We benefited from many useful discussions with M. E. Parke of the Jet Propulsion Laboratory. Comments by C. N. K. Mooers of the Naval Postgraduate School on the manuscript are also appreciated. The ISOS pressure record used in the study was provided by R. B. Wearn of the University of Washington. The research described in this paper was carried out by the Jet Propulsion Laboratory, California Institute of Technology, and by Oregon State University under contract with the National Aeronautics and Space Administration.

REFERENCES

- Alaka, M. A., and R. C. Elvander, Optimum interpolation from observations of mixed quality, *Mon. Weather Rev.*, **100**, 612-624, 1972.
- Born, G. H., M. A. Richards, and G. W. Rosborough, An empirical determination of the effects of sea state bias on Seasat altimetry, *J. Geophys. Res.*, **87**, 3221-3226, 1982.
- Bowen, J. L., and H. Stommel, How variable is the Antarctic Circumpolar Current?, in *Research in the Antarctic*, Publ. 93, edited by L. O. Quam, pp. 645-650, American Association for the Advancement of Science, Washington, D. C., 1971.
- Bretherton, F. P., R. E. Davis, and C. B. Fandry, A technique for objective analysis and design of oceanographic experiments applied to MODE-73, *Deep Sea Res.*, **23**, 559-582, 1976.
- Chelton, D. B., K. J. Hussey, and M. E. Parke, Global satellite measurements of water vapor, wind speed, and wave height, *Nature*, **294**, 529-532, 1981.
- Cheney, R. E., and J. G. Marsh, Oceanic eddy variability measured by Geos 3 altimeter crossover differences, *Eos Trans. AGU*, **62**(45), 743-752, 1981.
- Cheney, R. E., J. G. Marsh, and B. D. Beckley, Global mesoscale variability from collinear tracks of Seasat altimeter data, *J. Geophys. Res.*, **88**, 4343-4354, 1983.
- Cresswell, G. R., and T. J. Golding, Observations of a south-flowing current in the southeastern Indian Ocean, *Deep Sea Res.*, **27**, 449-466, 1980.
- Davis, R. E., Predictability of sea surface temperature and sea level pressure anomalies over the North Pacific Ocean, *J. Phys. Oceanogr.*, **6**, 249-266, 1976.
- Fu, L.-L., Recent progress in the application of satellite altimetry to observing the mesoscale variability and general circulation of the oceans, *Rev. Geophys. Space Phys.*, **21**, 1657-1666, 1983a.
- Fu, L.-L., On the wavenumber spectrum of oceanic mesoscale variability observed by the Seasat altimeter, *J. Geophys. Res.*, **88**, 4331-4342, 1983b.
- Fu, L.-L., and D. B. Chelton, Temporal variability of the Antarctic Circumpolar Current observed from satellite altimetry, *Science*, **226**(4672), 343-346, 1984.
- Gandin, L. S., *Objective Analysis of Meteorological Fields*, 242 pp., Israel Program for Scientific Translations, Jerusalem, 1965.
- Gordon, A. L., and B. A. Huber, Thermohaline stratification below the Southern Ocean sea ice, *J. Geophys. Res.*, **89**, 641-648, 1984.
- Gordon, A. L., E. Molinelli, and T. Baker, *Southern Ocean Atlas*, Columbia University Press, New York, 1982.
- Gordon, A. L., K. Horai, and M. Donn, Southern hemisphere western boundary current variability revealed by Geos 3 altimeter, *J. Geophys. Res.*, **88**, 755-762, 1983.
- Legeckis, R., and G. R. Cresswell, Satellite observations of sea surface temperature fronts off the coast of western and southern Australia, *Deep Sea Res.*, **28**, 297-306, 1981.
- Lorell, J., M. E. Parke, and J. F. Scott, Seasat Geophysical Data Record (GDR) Users Handbook (Altimeter), *JPL Internal Doc. 622-97, Revision A*, Jet Propulsion Lab., Pasadena, Calif., 1980.
- Lorell, J., E. Colquitt, and R. J. Anderle, Ionospheric correction for Seasat altimeter height measurement, *J. Geophys. Res.*, **87**, 3207-3212, 1982.
- Munk, W., and C. Wunsch, Observing the ocean in the 1990's, *Philos. Trans. R. Soc. London, Ser. A*, **307**, 439-464, 1982.
- Nowlin, W. D., Jr., and M. Clifford, The kinematic and thermohaline zonation of the Antarctic Circumpolar Current at Drake Passage, *J. Mar. Res.*, **40**(suppl.), 481-507, 1982.
- Nowlin, W. D., Jr., R. D. Pillsbury, and J. Bottero, Observations of kinetic energy levels in the Antarctic Circumpolar Current at Drake Passage *Deep Sea Res.*, **28**, 1-17, 1981.
- Parke, M. E., and M. C. Hendershott, M2, S2, K1 models of the global ocean tide on an elastic earth, *Mar. Geod.*, **3**, 379-408, 1980.
- Rapp, R. H., Geos 3 data processing for the recovery of geoid undulations and gravity anomalies, *J. Geophys. Res.*, **84**, 3784-3792, 1979.
- Reid, J. L., W. D. Nowlin, Jr., and W. C. Patzert, On the characteristics and circulation of the Southwestern Atlantic Ocean, *J. Phys. Oceanogr.*, **7**, 62-91, 1977.
- Schwiderski, E. W., Global ocean tides. 1. A detailed hydrodynamical interpolation model, *Mar. Geod.*, **3**, 161-217, 1980.
- Stewart, R. H., Satellite altimetry, in *Large-Scale Oceanographic Experiments in the WCRP*, WCRP Publ. Ser., vol. 2, pp. 261-287, 1, World Meteorological Organization, Geneva, Switzerland, 1983.
- Tai, C.-K., and C. Wunsch, An estimate of global absolute dynamic topography, *J. Phys. Oceanogr.*, **14**, 457-463, 1984.
- Tapley, B. D., G. H. Born, and M. E. Parke, The Seasat altimeter data and its accuracy assessment, *J. Geophys. Res.*, **87**, 3179-3188, 1982a.
- Tapley, B. D., J. B. Lundberg, and G. H. Born, The Seasat altimeter wet tropospheric range correction, *J. Geophys. Res.*, **87**, 3213-3220, 1982b.
- TOPEX Science Working Group, Satellite altimetric measurements of the ocean, *Doc. 400-111*, Jet Propulsion Lab., Pasadena, Calif., 1981.
- Wearn, R. B., and D. J. Baker, Jr., Bottom pressure measurements across the Antarctic Circumpolar Current and their relation to the wind, *Deep Sea Res.*, **27**, 875-888, 1980.
- Whitworth, T., III, Monitoring the transport of the Antarctic Circumpolar Current at Drake Passage, *J. Phys. Oceanogr.*, **13**, 2045-2057, 1983.
- Whitworth, T., III, W. D. Nowlin, Jr., and S. J. Worley, The net transport of the Antarctic Circumpolar Current through Drake Passage, *J. Phys. Oceanogr.*, **12**, 960-971, 1982.
- Wunsch, C., Bermuda sea level in relation to tides, weather, and baroclinic fluctuations, *Rev. Geophys. Space Phys.*, **10**, 1-49, 1972.
- Wunsch, C., and E. M. Gaposchkin, On using satellite altimetry to determine the general circulation of the oceans with application to geoid improvement, *Rev. Geophys. Space Phys.*, **18**, 725-745, 1980.

D. B. Chelton, College of Oceanography, Oregon State University, Corvallis, OR 97331.

L.-L. Fu, Jet Propulsion Laboratory, California Institute of Technology, 4800 Oak Grove Drive, Pasadena, CA 91109.

(Received September 18, 1984;
accepted October 27, 1984.)